The Influence of Turbulence and Magnetic Fields on the Non-Equilibrium

Chemistry Evolution in the Halos Surrounding Milky Way-like Galaxies

by

Edward Nathaniel Buie II

A Dissertation Presented in Partial Fulfillment
of the Requirements for the Degree
Doctor of Philosophy

Approved March 2022 by the
Graduate Supervisory Committee:

Evan Scannapieco, Chair
Sanchayeeta Borthakur
Chris Groppi
Danny Jacobs
Patrick Young

ARIZONA STATE UNIVERSITY

May 2022

ABSTRACT

The interactions that take place in the ionized halo of gas surrounding galaxies, known as the circumgalactic medium (CGM), dictates the host galaxy's evolution throughout cosmic time. These interactions are powered by inflows and outflows that enable the transfer of matter and energy, and are driven by feedback processes such as accretion, galactic winds, star formation and active galactic nuclei. Such feedback and the interactions that ensue leads to the formation of non-equilibrium chemistry in the CGM. This non-equilibrium chemistry is implied by observations that reveal the highly non-uniform distribution of lower ionization state speciies, such as Mg II and Si II, along with widespread higher ionization state material, such as O VI, that is difficult to match with equilibrium models. Given these observations, the CGM must be viewed as a dynamic, multiphase medium, such as occurs in the presence of turbulence. To better understand this ionized halo, I used the non-equilibrium chemistry package, MAIHEM, to perform hydrodynamic (HD) simulations. I carried out a suite of HD simulations with varying levels of artificially driven, homogeneous turbulence to learn how this influences the non-equilibrium chemistry that developes under certain conditions present in the CGM. I found that a level of turbulence consistent with velocities implied by observations replicated many observed features within the CGM, such as low and high ionization state material exisitng simultaneously. At higher levels of turbulence, however, simulations lead to a thermal runaway effect. To address this issue, and conduct more realistic simulations of this environment, I modeled a stratified medium in a Milky Way mass Navarro-Frenk-White (NFW) gravitational potential with turbulence that decreased radially. In this setup and with similar levels of turbulence, I alleviated the amount of thermal runaway that occurs, while also matching observed ionization states. I then performed magneto-hydrodynamic (MHD) simulations with the same model setup that additionally included rotation in

the inner halo. Magnetic fields facilite the developement of an overall hotter CGM that forms dense structures within where magnetic pressure dominates. Ion ratios in these regions resemble detections and limits gathered from recent observations. Furthermore, magnetic fields allow for the diffusion of angular momentum throughout the extended disk and gas cooling onto the disk, allowing for the maintaince of the disk at late times.

DEDICATION

To my mother, Jackie,

and to my brother, Marcus.

ACKNOWLEDGMENTS

This dissertation would not have been possible without the belief, support, and guidance from a multitude of people throughout the past six years. First, I have to thank my senior thesis advisor, Dr. Mark Voit, who encouraged me to think beyond my self-imposed limits and putting me on the path to applying to Arizona State University. I would not be here if not for you. Major thanks to my advisor Dr. Evan Scannapieco, who reinforced that mindset, encouraging me to apply for awards and helping me grow into the scientist I am today by allowing me the room to grow. Thank you for treating me as an equal, being available and open, and your patience as I worked through various challenges along the way. I have always said you were the best advisor, in my biased opinion, and my success throughout graduate school is in no small part to you giving me the space to explore opportunities and learn. I have always felt that my success and further goals were priorities for you, and I highly appreciate that. Additional thanks to my committee, Dr. Sanchayeeta Borthakur, Dr. Chris Groppi, Dr. Patrick Young, and Dr. Danny Jacobs, your support and insight, have enabled me to expand my knowledge and perspective. I would also like to thank Dr. Hilairy Hartnett, Dr. Christy Till, and Dr. Kimberly Scott for your invaluable insight, honesty, and openness in the later half of my graduate career as well as Becca Dial and all of the SESE staff for their assistance throughout it. I also have to thank Dr. William Gray, Dr. Mohammadtaher Safarzadeh, and Dr. Michele Fumagalli for your thoughtful feedback and insight throughout the simulation process.

I am beyond gratefu for all of the amazing friendships I have made while at ASU. I cannot thank everyone, it might become longer than the actual dissertation, however your impact on me has changed my life. Thank you Jon Hoh for being one of my first friends here and for always being uniquely you. Thank you to Nivedita Mahesh and J'Neil Blough-Swingen, my amazing office mates. Nive, your ambitous spirit is

contageous and sparked the ambition within me, something that I didn't know existed and am forever grateful to you for. Our conversations and the inspiration from both of you helped shape me and my belief in myself. Many thanks to Lucia Perez, your positivity has been a great addition to my life. Huge thanks to Genady Pilyavsky, Aishwarya Iyer, Jasmine Garani, and Grace Carlson for your thoughtful and honest conversations. You all have inspired me to continue growing and how to be a positive influence in the world. To all of my fellow graduate students, thank you for building such an amazing community.

To my friends outside of ASU, thank you for changing my life. Thank you to my amazing and inspiring lifelong friends I made internationally, my Italian brother, Aronne Travaglia, and Lizelke Klindt. Thank you to Sensei Dawn Croft for your life lessons inside and outside of the dojo.

And of course, my sincerest thanks to my mom, brother, and dad. Thank you to my dad for planting the dream of studying space in me when I was a child. Thank you to my mom for your support and endless love, you inspire me to be a better person each day, in everything I do. Thank you to my brother for inspiring me with your actions and always being an amazing human being, even from when we were young. You following your dreams empowered me to follow mine.

TABLE OF CONTENTS

LIST OF TABLES

LIST OF FIGURES

Figure   Page

xi

Figure

Chapter 1

INTRODUCTION

In the earliest days of astronomy, humans looked to the sky and saw flickering lights. In time, technology would allow us to gaze upon these in detail and see that they were different. Nearby objects were revealed to be planets, some of which exist beyond our Solar System, while others were bright balls of gas like our Sun. The furthest objects appeared as clouds of dust and gas, and later, came to be known as galaxies. As observational instruments improved, astronomers began analyzing properties of gas found within our own galaxy, the Milky Way, and eventually, those beyond it. The presence of clouds within a galaxy's spiral arms hinted at the possibility of a medium outside the galaxy that possessed a similar pressure. These clouds, along with persistent radio observations of noise suggested an extragalactic origin that lay in a medium surrounding our galaxy. Theoretical discussions that posited the existence of a "galactic corona" extending past the galactic plane were offered to explain these findings (Shklovsky, 1952; Pickelner, 1953; Ter Haar, 1955; Spitzer, 1956). In the time that followed, observations of spectral lines showed singly-ionzed calcium absorption, Ca II, along with neutral sodium, Na I, probed colder clouds that could exist in pressure equilibrium with an encapsulating hot and diffuse medium near 10^6 K (Münch and Zirin, 1961).

This galactic corona is now known as the circumgalactic medium (CGM), the diffuse halo of ionized gas that surrounds all galaxies and plays an important role in regulating their evolution. Much remains to be understood about this medium and the interactions that take place within it. Direct and detailed observations of the CGM are difficult, owing to its diffuse nature which limits the amount of detectable emission.
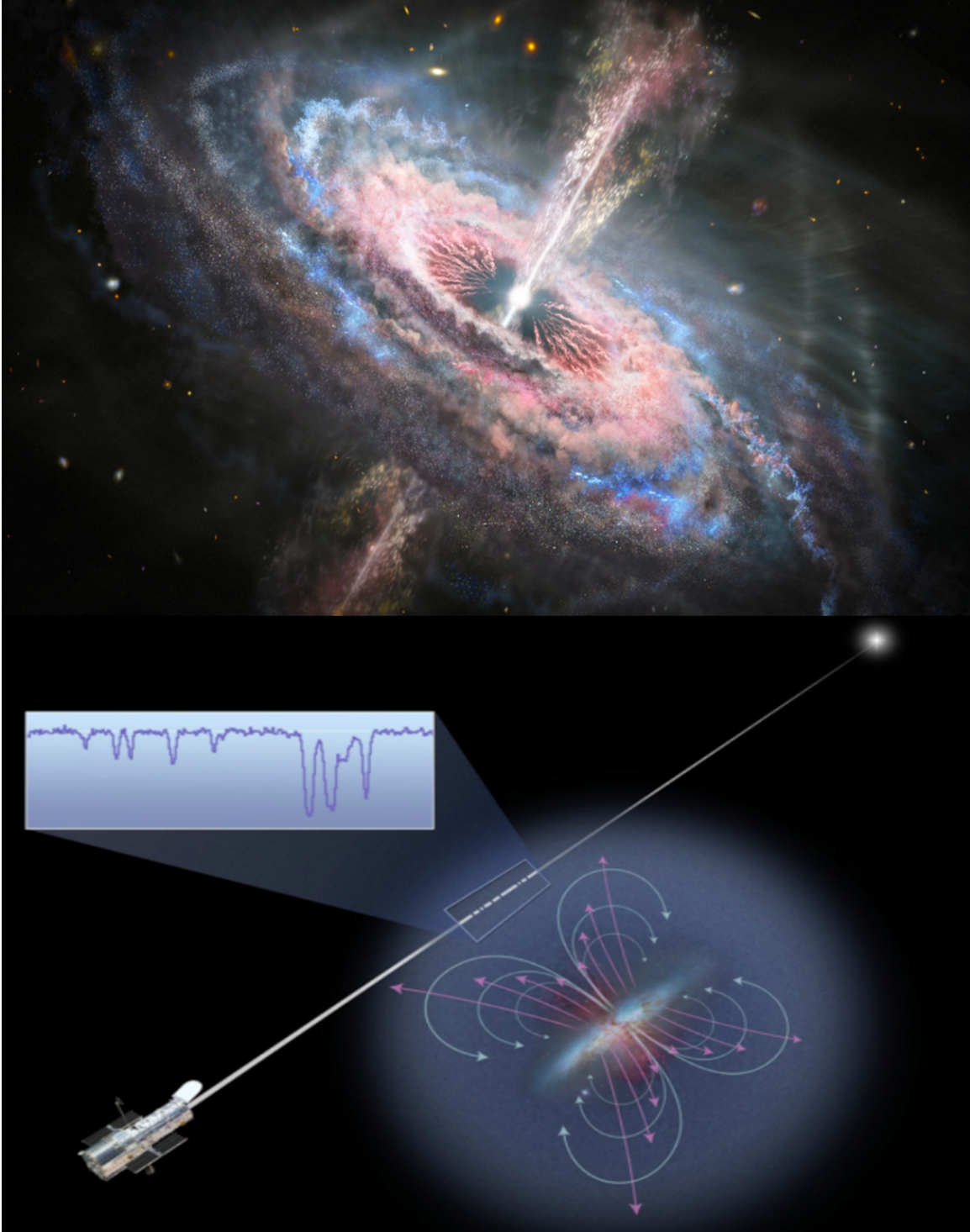
Figure 1.1: Top: An illustration of a quasar in a distant galaxy as it emits large amounts of energy resulting from matter falling into a supermassive black hole. Bottom: An example of quasar light intersecting with intervening CGM gas on its path towards the *Hubble Space Telescope*. Image credit: Top: NASA, ESA, and J. Olmsted (STScl), Bottom: NASA, STScl, and Ann Field

Astronomers, however, have found ways to circumvent this by taking advantage of intervening absorption in the spectra of stars and the brightest objects in the universe, active galactic nuclei, also known as quasars.

While these observations have revealed much, there are difficulties associated with making them, along with a limited sample. These types of observations, known as absorption line spectroscopy, rely on background sources and may only yield information on the gas along the line of sight. Additionally, they are typically limited to a few sightlines per galaxy. As such, there is a need for theoretical approaches to help inform these observations of the CGM. Hydrodynamic simulations allow for a detailed investigation of the physics that dominate this medium and how they influence its dynamics over time. This work aims to improve on the understanding of processes that occur in the CGM and the observable features they produce.

1.1   The Circumgalactic Medium

1.1.1   Theoretical Origins of the Circumgalactic Medium

In the 1950's astronomers began to theorize the existence of an extended halo surrounding galaxies. Hoyle (1953) examined the evolution of this halo as a means to form a galaxy and feed the star formation within it. In that manuscript, the tendency for galaxies to be observed in clusters, their typically mass range of $3 \times 10^{9-11}$ M$_\odot$, and the stars they tend to form led to the idea of fragmentation in an extragalactic hydrogen cloud as a means to form galaxies.

Hoyle (1953) used the idea of an expanding universe to establish a lower limit on the density of this extralactic cloud, while earlier work in Smith (1936) which focused on analyzing the Virgo Supercluster inferred an upper density limit. It was put forth that halos around individual galaxies would possess a mean density at about

3

10^{-27} g cm^{-3} (5×10^{-4} cm^{-3}) with two phases of gas at temperatures near 10^4 K and $\gtrsim 3 \times 10^5$ K. These estimates of the temperature resulted from knowledge of the turbulent motions that would be, over time, converted to heat, along with the assumption that the gas would primarily be composed of neutral hydrogen. These early calculations showed that gas in the higher temperature phase would be unable to fully radiate away its thermal energy and instead adiabatically expand, while a galaxy may form in the center with a mass near 5×10^{11} M$_\odot$

In the following years, Spitzer (1956) theorized about the CGM origins, traits, and further predicted that it would not be observable in optical light due to its high temperature. Spitzer further theorized that the CGM may be at temperatures between 10^5 and 3×10^6 K, in pressure equilibrium with dense clouds embedded within. Based on this temperature and the assumption of hydrostatic equilbrium, he also estimated it to have densities near 10^{-4} cm^{-3}. If it were to be at temperatures much higher than the aforementioned upper limit, it would no longer be bound by gravity. An intergalactic medium was ignored due to the lack of observational evidence at the time, and thus nothing could be inferred about its existence or features. Comments were made about the halo mass content being about a few percent of the total mass within the galaxy, about 10^8 M$_\odot$, assuming isothermal conditions. Lastly, he postulated that observations of this medium would need to be made using absorption at wavelengths shorter than 2000 $\mathring{A}$, relying on the higher state ions that would presumbly be present (e.g. Mg x, O vi, N v, and C iv).

1.1.2   Observations of the CGM

Initial observations of the CGM focused on the cold gas within the halo surrounding the Milky Way, revealed through low and intermediate ion ultra-violet (UV) absorption in the spectra of stars near the galactic plane (Münch and Zirin, 1961).

These observations were limited due to the lack of bright stars found above and below the galactic plane.

Later that decade, other astronomers began to observe similar absorption at higher redshifts ($z \approx 1-3$) as the light from distant, bright quasars intersected these systems along its path towards Earth (Bahcall, 1968; Bahcall $et\ al.$, 1968; Burbidge $et\ al.$, 1968; Burbidge, 1969). Bahcall and Spitzer (1969) suggested this intervening absorption showing multiple ionization states belonged to extended halos of gas surrounding distant galaxies. The gas in these halos would be at temperatures between 10^{4-6} K and in pressure equilibrium, as small clouds would need to be confined by the pressure of an encompassing medium around 10^{-13} dyne cm^{-2} to prevent these clouds from expanding due to the high pressures within.

As time progressed, the amount of data on these intervening absorption line systems increased with additional detections of Lyman-α, C IV, Si IV, and Mg II absorption at high and low redshifts (Sargent $et\ al.$, 1980; Young $et\ al.$, 1982; Bergeron and Stasińska, 1986; Lanzetta $et\ al.$, 1987). These studies provided further evidence for a halo whose extent was larger than the optical size of central galaxies and possessed gas at varying ionization states.

Additional results from these studies were able to show that strong C IV absorption was typically associated with Mg II, while weaker absorption showed an abscence of this low ionization state gas. Furthermore, strong absorption was often revealed with multiple components along the line of sight, while weak absorption only consisted of a single component. Lanzetta and Bowen (1990) further showed a correlation between small radial distances from the central galaxy and large equivalent widths of Mg II absorption in their low redshift study. This meant that the cold clouds that housed this lower ionization state gas were preferentially located near the central galaxy, instead of evenly dispursed throughout the halo or on the outskirts.

Around this same time, Steidel and Sargent (1987) were observing high redshift ($z > 3$) quasars to gain insight on the Lyman α forest, a series of absorption lines in spectra resulting from Lyman α electron transitions in H I. Their observations further supported intervening clouds of hydrogen which were able to reduce the amount of flux from these quasars. Following this, Steidel *et al.* (1994) reported results from a survey that investigated galaxy properties whose intervening halos showed Mg II absorption in background QSO spectra in the redshift range $0.2 \lesssim z \lesssim 1$. This study found that all galaxies, whether star-forming or not, possessed a halo of diffuse gas that was revealed via absorption features. Furthermore, this absorption did not depend on the host galaxy's star formation rate and instead correlated with its mass.

The launch of the *Hubble Space Telescope (HST)* with its Faint Object Spectrograph (FOS) allowed for huge strides to be made in the study of these extended halos due to its powerful resolving capabilities of Lyman-α and C IV absorption in nearby, $z \lesssim 1$, systems (Morris *et al.*, 1991). Using HST, Bahcall *et al.* (1993) constructed a catalogue of lower redshift absorption systems, including those in our Milky Way's halo, in their HST Quasar Absorption Line Key Project. These observations, in combination with those made with other instruments, such as the National Radio Astronomy Observatory (NRAO) and the International Ultraviolet Explorer (IUE), provided new insights into extended halos such as Lyman-α absorption that was typically associated with multiple metal line systems, hinting at large coherent structures in extended halos (Bahcall *et al.*, 1996).

Although it has been rare, emission from the hot ($T \gtrsim 10^6$ K), ambient component has been accomplished by observing soft X-rays. One of the first to observe this was Kuntz and Snowden (2000) who were able to separate emission from the hot halo and that found in the local hot bubble, a cavity in the halo above and below the Milky Way disk that results from supernovae, using the ROSAT All-Sky Survey.

6

More recently, the Keck Baryonic Structure Survey (KBSS; Rudie *et al.*, 2012) targeted distant galaxies between $2 < z < 3$. This period of time was chosen to gain insight into the CGM surrounding galaxies near the peak of star formation to see how resulting feedback impacted the halo. This further confirmed an anti-correlation between large impact parameters and H I absortion, and also mapped the H I distribution around such systems. These authors further derived slightly larger covering fractions for their higher redshift sample in comparison with those found in the lower redshift studies conducted in Chen *et al.* (e.g. 2001b); Wakker and Savage (e.g. 2009); Prochaska *et al.* (e.g. 2011). Additionally, Turner *et al.* (2014) studied the metals in the KBSS galaxy halos and found evidence for more extended absorption from intermediate/higher ions such as Si IV, C IV, and O VI as compared to H I.

Soon after, the COS-Halos Survey (Tumlinson *et al.*, 2013) was undertaken which took advantage of the newly installed Cosmic Origins Spectrograph (COS) that increased the sensitivity to the UV absorbtion of diffuse gas (Shull, 2009). This survey probed nearby galaxies with $z \lesssim 0.5$, finding lower ion absorption that became less prevalent with greater radial distance from the central galaxy in addition to O VI absorption seen at all distances (Werk *et al.*, 2013). Werk *et al.* (2016) further analyzed this data to understand the physical conditions of the O VI absorption, typically finding broad lines with widths > 40 km s^{-1} within the CGM surrounding star-forming galaxies. A subset of these lines did not overlap with any lower ion absorption, leading them to conclude that they must trace the encompassing hot and diffuse portion of the halo. The observed mix of ionization states emphasized the need to view the CGM as a multiphase medium where gas of varying temperatures could simultaneously exist in pressure equilibrium.

Bordoloi *et al.* (2018) further analyzed the equivalent widths of Lyman-α, W$_{Lya}$, in the inner 160 kpc of the CGM surrounding nearby galaxies from the COS-Halos

and COS-Dwarfs surveys (Tumlinson *et al.*, 2013; Bordoloi *et al.*, 2014, respectively) with varying stellar masses between $8 \lesssim M_*/M_\odot \lesssim 11.6$. They were able to see that these nearby galaxies had H I covering fraction $\gtrsim 80\%$, declining equivalent widths as radial distance from the center increased, as well as a positive correlation between W_{Lya} and M_*. They suggest this correlation results from a fundamental plane relationship between the halo mass, W_{Lya}, and radial distance from the center.

Finally, the very recent KODIAQ-Z survey (Keck Database of Ionized Absorbers toward Quasars) looked at high redshift ($z > 2$) H I absorbers with columns $\gtrsim 10^{14.5}$ cm^{-2} in an effort to derive their metallicities (Lehner *et al.*, 2021). Although some of these absorbers were found to be near pristine in their metal content ($[X/H] < -2.4$) many were also found to be metal enriched with $[X/H] > -1$. All of these observations have the commonality of revealing the CGM surrounding galaxies, whether nearby or far, to be at least somewhat metal enriched and definitively multiphase, with ionization states from singly and doubly ionized species embedded in a hotter medium traced by higher ionization state gas.

1.2   Simulations of the CGM

1.2.1   Initial Ionization Models of the CGM Environment

While the earliest theoretical work hinted at the existence of an extended, hot and diffuse halo, the implication of consistent observations of ionization states in multiple phases have been important as many have put forth theories to explain the evolution of such a medium that could result in the observed ionization structure.

Kafatos (1973) was the first to investigate the time-dependent cooling that results in a $T = 10^{4-6}$ K gaseous environment. These early calculations looked at the non-equilibrium radiative cooling albeit at densities larger than those found in the CGM

as the authors were focused on the interstellar gas near a supernova which would lie at densities $\approx 1 \, \mathrm{cm}^{-3}$. Although the densities were higher, this work found faster cooling as compared to recombinations, whereas equilibrium would see these two processes happening at equal rates. As a result, gas emits more energetic radiation into its surroundings in comparison to if this gas were to be in ionization equilibrium.

Following this work, Shapiro and Field (1976) delved into modeling a diffuse hot halo and found a steady-state model failed to reproduce the narrow O vi lines observed and furthermore, the resulting pressures in such an environment would lead to convection wherein hot gas would rise beyond the disk to eventually radiatively cool and condense back onto the disk. Moreover, steady-state models could not facilitate the necessary pressure equilibrium that must exist between the cold and hot material in the diffuse halo.

Edgar and Chevalier (1986) considered isobaric and isochoric time-dependent cooling to derive column densities and UV luminosities that may be observed in this low density environment while it cools from $T \gtrsim 10^6$ K. They found that higher ionization states are able to persist at smaller temperatures as compared to what one would find from collisional equilibrium models. Their ability to match observations were mixed, with an accurately predicted N_{NV}, however underpredicting N_{SiIV} and overpredicting N_{OVI}. Furthermore, predicted fluxes for many ions were not in agreement with observed fluxes of gaseous halos. These early models made great strides in our knowledge of this hot and diffuse environment, however, more complex models would be needed to fully understand its evolution and the underlying mechanisms behind the observations.

1.2.2 Specific Situational Models

Additional authors conducted studies that investigated specific scenarios and environments that may be found in the CGM as a means for the production of the multiphase ions observed. These studies were typically conducted in two dimensions as three dimensional studies were prohibitively expensive at the time.

Turbulent mixing layers was seen as a viable model for explaining the observations as such a scenario would develop between cold and hot ambient material in the CGM (Begelman and Fabian, 1990; Slavin *et al.*, 1993; Kwak and Shelton, 2010). These previous studies found a majority of the mixing to persist in the hotter ambient medium layer of the interface as cold gas is entrenched in the hot medium and is susceptible to mixing. The mixing occurs on shorter timescales than ionization and recombination, making it a viable source for the intermediate ions, even showing low ionization states may persist within this mixed material. Furthermore, UV radiation from the mixing layer could lead to photonionization of low ions to intermediate ions. These layers were able to reproduce the intermediate and highly ionized elements (e.g. C IV, N V, and O VI) that were observed in the halos surrounding galaxies.

Related to the model of mixing layers, authors also focused on conduction in the interface between cool clouds and the hot ambient gas wherein electrons are responsible for transferring heat to the colder medium which may lead to evaporation and eventually, condensation (Borkowski *et al.*, 1990; Gnat *et al.*, 2010). While intermediate and highly-ionized species of elements were found at higher amounts when compared to photoionization equilibrium models, they still fell short of those found in observed systems. Thus, conduction at these interfaces was not enough to fully replicate the multiphase ionization observed in the CGM.

Flows that develop radiative cooling throughout was another situation that re-

ceived further consideration. The earliest of these models found that non-equilibrium chemistry resulted in longer lifetimes for intermediate and highly ionized elements at lower temperatures as compared to collisional equilibrium models, although ions like C IV and Si IV were underproduced (Edgar and Chevalier, 1986; Benjamin, 1994). Gnat and Sternberg (2007) further varied the metallicity between $10^{-3} - 2$ $Z_\odot$, finding non-equilibrium radiative cooling produced the largest departure from equilibrium chemistry at large metallicities as compared to low. Wakker *et al.* (2012) expanded on these by considering gas kinematics and found intermediate and higher ions were able to better match the observations for flow velocities between 10-40 km s^{-1}.

Models that shed light on the ionized gas lying in the wake of shocks have also been considered (Dopita and Sutherland, 1996; Allen *et al.*, 2008; Gnat and Sternberg, 2009). These models revealed a scaling relation that showed greater UV radiation was produced as the shock velocity increased. They also saw varying metallicity to have the greatest influence over the departure from equilibrium models, a result that was similarly found in the radiative cooling flow models. These models were also conducted with magnetic fields, where authors consistently found strong magnetic fields led to a isochoric cooling while no magnetic field typically led to an isobaric situation. Lastly, they saw that cases with a strong magnetic field enabled photoionization to dominate in the cooling layers.

Models such as these added to the foundational work that came before them and showcased how these situations can influence the gas found in the CGM. These studies helped to refine ion properties that were needed to more accurately model the transitions between ionized states; properties that would be used in future simulations. They further highlighted the need for non-equilibrium models as they were most likely to provide a result that included the simultaneous presence of higher and lower ionized species, as well as the intermediate ionization phase which equilibrium

models had the most difficulty in reproducing.

1.2.3   Cosmological Simulations

Some of the most advanced models set out to tackle the problem of the CGM evolution by considering a combination of the relevant physics at a variety of scales. These models, though computationally intensive, allow researchers to gain a more wholistic picture of how the environment surrounding the CGM, as well as the galaxy at its center, influences its dynamics and chemical evolution throughout cosmic time. These simulations also provide insight into the missing baryon problem; a problem involving the ΛCDM model's prediction for the amount of baryons that should reside within galaxies. In reality, however, observed galaxies show a small fraction of the expected baryons in their interstellar medium (ISM) and stars.

One of the first to run such a model was Cen *et al.* (2005). While they aimed to understand the role of galactic superwinds in enriching the intergalactic medium (IGM), they also found results relevant to the CGM. Low density gas in their simulations with $N_{\mathrm{HI}} \lesssim 10^{14}$ cm^{-2} was able to be enriched with metals up to 10^{-2} Z$_\odot$. Following this, Oppenheimer and Davé (2008) used the GADGET-2 cosmological code (Springel, 2005) to understand the impact of feedback mechanisms capable of distributing mass, metals, and energy throughout the CGM, tracking carbon, oxygen, silicon, and iron production by Type II and Type Ia supernovae and asymptotic giant branch mass loss. They found that lower redshift galaxies retained their ejected material as it rained back down on the central galaxy with Type II supernovae dominating the production of the tracked elements at all times.

In the years that followed, Ford *et al.* (2014) revisited the GADGET-2 model to examine the H I and metal absorption lines in low redshift galactic halos, having the ability to track the evolutionary history of gas particles. They found that much of

the mass ($\approx 85\%$) is in the hot ambient portion of the CGM and not cycling through inflows/outflows, and further is best categorized as neutral hydrogen. The majority of metal ion absorption resulted from gas that will rejoin the host galaxy within a Gyr with Mg II and Si IV being good tracers of this material. O VI instead traced gas that left the central galaxies many Gyrs in the past.

The EAGLE project further improved our understanding of the CGM in this cosmological context with their updated subgrid AGN and star formation feedback physics (Schaye *et al.*, 2015). Oppenheimer *et al.* (2016) found their non-equilibrium chemistry network to reproduce the COS-Halos observations of O VI as well as confirming that such gas represented older gas that was ejected in the galaxies' distant past. Furthermore, they found AGN were able to push newly produced metals beyond the virial radius of simulated galaxies. Correa *et al.* (2018) also confirmed this finding of metals that have been ejected outside the CGM while supernovae increased the mass found in the hot halo component.

Others models such as the Illustris-TNG and AGORA, represent the latest advancements in these zoom-in cosmological simulations as they continue to add more realistic prescriptions for cooling, heating, and various feedback phenomena (Marinacci *et al.*, 2018; Roca-Fàbrega *et al.*, 2021, respectively). All of these types of models have been useful in improving the understanding of the CGM dynamics and their influence on the chemical evolution. However, even with these advancements in models, the influence of specific considerations in this environment remains uncertain.

The work presented here delves into the effect of turbulence in a hot and diffuse medium. Turbulence encourages the mixing of material and the exchange of energy through cascades from larger scales to smaller that eventually dissipates energy as heat (Kolmogorov, 1962). The turbulence is also modeled in non-equilibrium gas which has been shown to better match the mixture of ionization states found in the CGM

(Oppenheimer and Schaye, 2013; Oppenheimer *et al.*, 2016). The simulations are most similar to the turbulent mixing layer models, albeit with widespread turbulence instead of only at the boundaries of cold and hot gas. This introduces the additional aspect of being able to produce shocks that ionizes gas, leaving it in their wakes.

1.3 Structure of Thesis

Chapter 2 of this work presents the results from turbulent box hydrodynamic simulations that utilize the non-equilibrium chemistry solver, MAIHEM. These simulations span a relevant range of the paramater space found in the CGM and shows the influence that turbulence and a UV background has on the non-equilibrium chemical evolution. Such turbulence is able to promote mixing between cold and hot gas, further smearing the cooling curve that develops for non-equilibrium gas. In Chapter 3, I present results from an updated model of MAIHEM that solves the non-equilibrium chemistry in a galactic halo initialized with a density gradient and gravity that results from a Milky Way mass dark matter halo. These simulations consider various levels of inhomogeneous turbulence to find if such a treatmenat could lead to convective motions in the halo to produce column densities and ion ratios that match observations from nearby halos. Chapter 4 presents an expansion on this updated model by adding co-rotation in the halo along with magneto-hydrodynamic (MHD) considerations. These additions combined with the inhomogeneous turbulence and non-equlibrium chemistry bring simulations closer to reality as all of these are examined throughout the evolution of the idealized CGM. In Chapter 5, I summarize these results and how they further characterize the disruption and ionization of galactic winds.

Chapter 2

MODELING PHOTOIONIZED TURBULENT MATERIAL IN THE CIRCUMGALACTIC MEDIUM

2.1 Introduction

The circumgalactic medium (CGM) is a highly ionized plasma that resides within the dark matter halo of galaxies. It contains the reservoir of baryons for galaxy formation and has an important role in regulating galaxy evolution through inflow and outflow processes, such as galactic accretion, active galactic nuclei, and galactic winds (e.g. Lilly *et al.*, 2013; Voit *et al.*, 2015; Crighton *et al.*, 2015; Fox and Davé, 2017; Muratov *et al.*, 2017; Tumlinson *et al.*, 2017). Its diffuse nature, however, makes direct observation difficult.

Absorption in the spectra of background QSOs allows us to gain insight into these diffuse systems. Steidel (1998) summarized much of the earlier results that attempted to understand the relationship between the Intergalactic Medium (IGM) and the CGM. At the time, the newly commissioned WFPC-2 on the *Hubble Space Telescope (HST)* as well as the HIRES spectrograph on the Keck telescopes, gave us the capability to observe these systems up to $z \approx 3$ with improved follow-up spectroscopy. The Keck Baryonic Structure Survey (KBSS; Rudie *et al.*, 2012) continued these efforts by targeting galaxies at the peak of star-formation ($z \approx 2 - 3$). It is theorized that at higher redshift there should be a high accretion rate of cold material through filamentary structures (e.g. Birnboim and Dekel, 2003; Ocvirk *et al.*, 2008;

15

Brooks *et al.*, 2009; Faucher-Giguère and Kereš, 2011). They were able to map the H I distribution around these systems as well as show an anti-correlation between H I absorbers and impact parameter.

In recent years, the Cosmic Origins Spectrograph (COS) installed on the HST has vastly improved our sensitivity to diffuse material that absorbs in the UV (Shull, 2009). Specifically, the COS-Halos survey allowed us to probe the CGM of $z \lesssim 0.5$, galaxies (Tumlinson *et al.*, 2013) by using quasar absorption-line spectroscopy. Tumlinson *et al.* (2013) probe $M_* = 10^{9.5} - 10^{11.5}$ $M_\odot$ galaxies out to an impact parameter, $b = 150$ kpc. These observations uncovered a large amount of O VI absorption in the CGM of star-forming galaxies and also showed a neutral H component associated with nearly all of the galaxies.

Werk *et al.* (2013) expanded upon this study by finding significant metal-line absorption corresponding to a cool ($T \approx 10^4 - 10^5$ K) CGM phase. This cooler phase is constrained to the inner CGM such that column densities and detection rates for lower ionization species decrease with increasing impact parameter. Furthermore, in Werk *et al.* (2016, hereafter W16) O VI absorption within the star-forming sample is further explored. They find O VI absorption to span the entire CGM, while also discovering N V absorption to be absent in 35 of the total 38 O VI components.

W16 also looked at many models to explain this phenomenon; these included photoionization models such as CLOUDY (Ferland *et al.*, 2017), shock ionization models (Gnat and Sternberg, 2009), collisional ionization equilibrium and non-equilibrium models (Gnat and Sternberg, 2007), radiative cooling flow models (Wakker *et al.*, 2012) and more. These models either required very high ionization from an extragalactic ultraviolet background (EUVB), unphysically long path lengths for O VI, or a narrow range of parameters to fit the data. This motivates us to explore the effects of turbulence in the CGM.

There are several CGM processes that are likely to drive significant turbulence. Theoretical work has shown that inflows should be distinctly colder than the surrounding medium (Kereš *et al.*, 2005; Dekel and Birnboim, 2006; Kereš and Hernquist, 2009; Stewart *et al.*, 2011) and there is observation evidence of colder inflowing material around star-forming galaxies (Rubin *et al.*, 2012). As this colder material flows inward, there should at least be turbulence along the boundaries between colder and hotter material. Also in the case of outflows, material, momentum, and energy are injected into the surrounding medium, which may also induce turbulence. This leads us to theorize how various ions may change in the presence of isotropic turbulence.

Here we present direct numerical simulations of a turbulent astrophysical media exposed to an EUVB, in an effort to determine the extent to which multiphase observations of the CGM can be explained by the presence of sustained, isotropic turbulence. The paper is organized as follows: in Section 2 we outline the code used to model the CGM. In Section 3 we present our results with a focus on O VI and N V abundances as well as compare our results to W16 and give concluding remarks.

2.2 Methods

2.2.1 The MAIHEM Code

To simulate an isotropic turbulent CGM, we use Models of Agitated and Illuminated Hindering and Emitting Media (MAIHEM[1]), a three-dimensional (3D) cooling and chemistry package built using FLASH (Version 4.3), an open-source hydrodynamics code (Fryxell *et al.*, 2000). MAIHEM explicitly tracks the reaction network of 65 ions: including hydrogen (H I and H II), helium (He I–He III), carbon (C I–C VI), nitrogen (N I–N VII), oxygen (O I–O VIII), neon (Ne I–Ne X), sodium (Na I–Na III),

---

[1]http://maihem.asu.edu/

magnesium (Mg I–Mg IV), silicon (Si I–Si VI), sulfur (S I–S V), calcium (Ca I–Ca V), iron (Fe I–Fe V), and electrons from an initial non-equilibrium state to steady state. This includes solving for dielectric and radiative recombinations, collisional ionizations with electrons, charge transfer reactions, and photoionizations by a UV background.

This package was first developed in Gray *et al.* (2015) and later improved upon with the inclusion of an ionizing background in Gray and Scannapieco (2016). Most recently, in Gray and Scannapieco (2017), several charge transfer reactions, radiative recombination rates, and dielectronic recombination rates from Aldrovandi and Pequignot (1973); Shull and Van Steenberg (1982); Arnaud and Rothenflug (1985) have been added to and updated in MAIHEM. Furthermore, the cross sections for the photoionizing and photoheating rates are taken from Verner and Yakovlev (1995) for the inner electron shell transitions and Verner *et al.* (1996) for the outer electron shell transitions.

The equations solved by MAIHEM are given in Gray and Scannapieco (2016) and are invariant under the transformation $x \to \lambda x$, $t \to \lambda t$, $\rho \to \rho/\lambda$ meaning the final steady-state abundances depend only on the mean density multiplied by the driving scale of turbulence, nL, the one-dimensional (1D) velocity dispersion of the gas, σ_{1D}, and the ionization parameter, U; the ratio of number of ionizing photons to the number density of hydrogen n_H, or alternatively,

$$U \equiv \frac{\Phi}{n_H c}, \tag{2.1}$$

where Φ is the total photon flux of ionizing photons, and c is the speed of light.

Finally, we elect to model turbulence through solenoidal modes ($\nabla \cdot F = 0$) and use an unsplit solver based on Lee (2013) to solve the hydrodynamic equations. In addition to this, we make use of a hybrid Riemann solver that utilizes the Harten
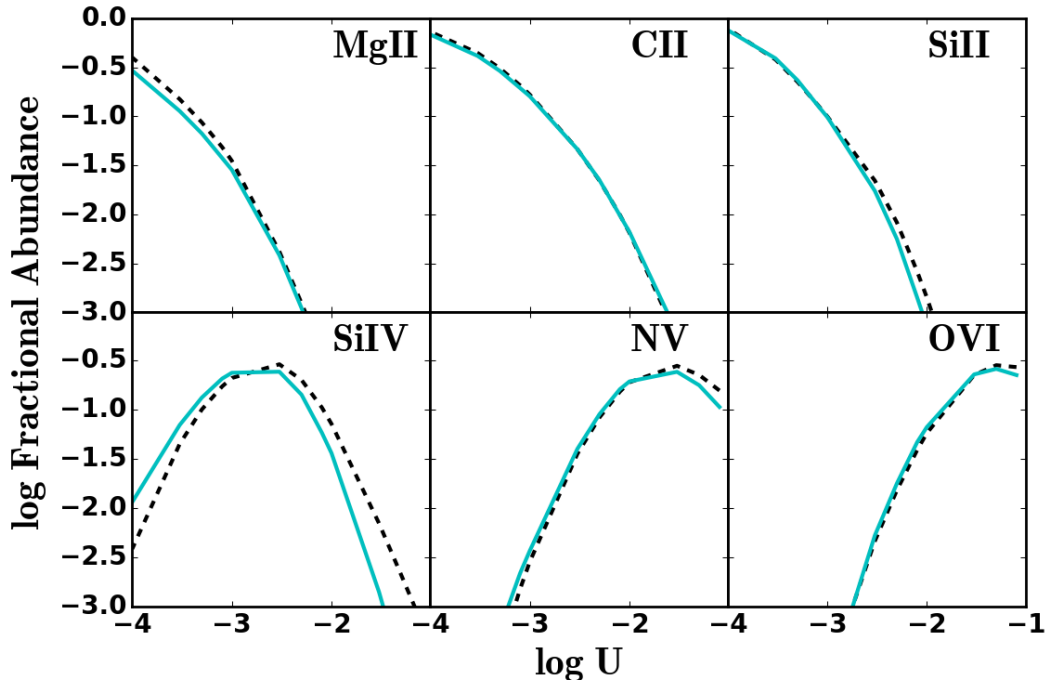
Figure 2.1: Comparison of fractional abundances for MAIHEM (dashed black) and CLOUDY (solid cyan). MAIHEM was run with $nL_{\mathrm{box}} = 10^{21}$ cm^{-2} with $\sigma_{\mathrm{1D}} = 1$ km s^{-1}. CLOUDY was run with a varying hydrogen density such that the resultant U was varied between $-4 < \log U < -1$.

Lax and van Leer (HLL) solver (Einfeldt *et al.*, 1991) in places with strong shocks or rarefactions and the Harten–Lax–van Leer–Contact (HLLC) solver (Toro *et al.*, 1994; Toro, 1999) in smoother flows to stabilize the code as turbulence ensues. We refer the reader to Gray *et al.* (2015) and Gray and Scannapieco (2016) for further details.

2.2.2   Abundance Test

MAIHEM has been rigorously tested over a wide parameter space in Gray *et al.* (2015), Gray and Scannapieco (2016). However, to confirm its accuracy under conditions similar to those in the CGM, we carry out a series of tests at a metallicity of $0.3Z_{\odot}$, which is the median value found by Prochaska *et al.* (2017) for the CGM of

low-redshift galaxies.

MAIHEM abundances are compared to those given by CLOUDY, an open-source photoionization code (Ferland *et al.*, 2013). Specifically, we conduct single-zone CLOUDY runs and MAIHEM runs with $nL = 10^{21}$ cm^{-2} and σ_{1D} of 1 km s^{-1} that both use the Haardt and Madau (2012, hereafter HM2012) EUVB. We also omit the presence of molecules in our CLOUDY tests. Here we show some of the ion abundance comparison plots in Figure 2.1 for ions that we will focus on throughout the paper. Ion abundances for MAIHEM are found using solar relative abundances from Lodders (2010).

We note that out of the abundances plotted, all of them closely agree with CLOUDY with the exception of Si IV at $\log U > -2$. It seems that MAIHEM slightly overpredicts the higher ion fractional abundance, which takes away from the fractional abundance at high U.

2.2.3 Model Parameters

Following this abundance test, we conduct a suite of simulations to see the effect of isotropic turbulence on ion abundances. Our simulations force turbulence by stirring via solenoidal modes (Pan and Scannapieco, 2010) with wavenumbers that vary between $1 \leqslant L_{\mathrm{box}}|k|/2\pi \leqslant 3$. This ensures that the average driving scale of turbulence is $k^{-1} \simeq 2L_{box}/2\pi$ where L_{box} is set to 100 pc.

We carry out these simulations in a 128^3 periodic box and begin with a uniform density of $n = 10^{-2} - 1$ cm^{-3}, with the lower end corresponding to the density of the CGM (Tumlinson *et al.*, 2017). These densities correspond to a driving scale of turbulence that varies from $nL_{\mathrm{box}} = 10^{19} - 10^{21}$ cm^{-2}. The medium is initialized with a fractional ion abundance that corresponds to collisional ionization equilibrium at a temperature of $T = 10^5$ K.
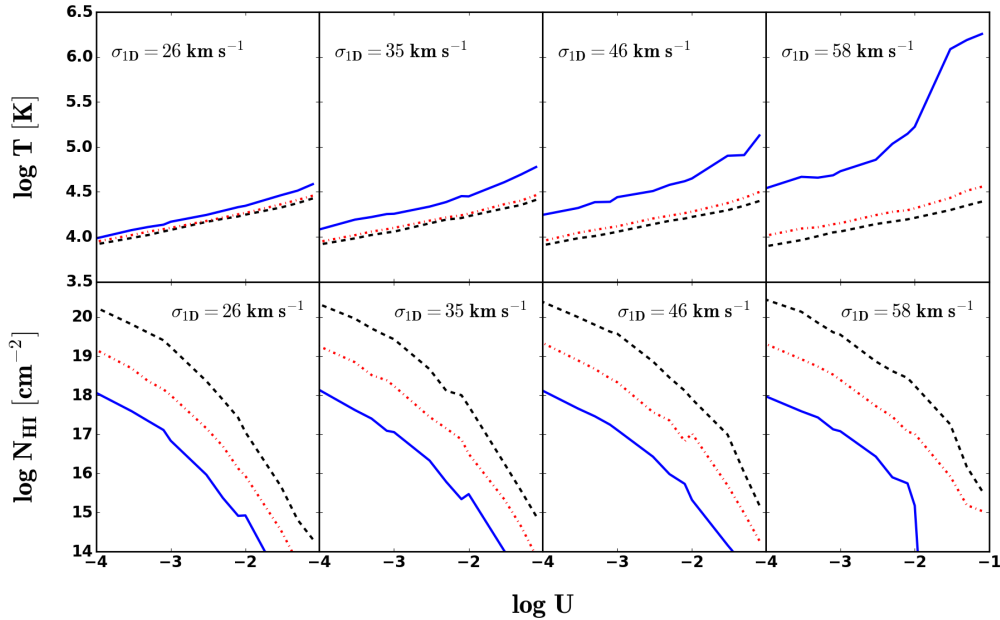
Figure 2.2: Log temperature vs. log U (top row) and log $N_{H\,1}$ vs. log U (bottom row) for the $nL = 10^{19}$ (solid blue), 10^{20} (dotted-dashed red), and 10^{21} (dashed black) cm^{-2} runs. From left to right, $\sigma_{1D} = 26,\ 35,\ 46,\ 58$ km s^{-1}.

The range of σ_{1D} that we test is varied between 26 and 60 km s^{-1} following estimates of the nonthermal velocity components of line-widths measurements (W16). The box is irradiated with a redshift zero HM2012 EUVB whose strength is quantified by U, such that it varies between $-4 < \log U < -1$ in a single run by progressing in increments of $\log U \sim 0.2$ once a steady state is reached. To determine when the box has reached a steady state, the average global abundances were calculated every 10 time steps. To ensure that our simulations reached a steady state, we impose a cutoff value to the change in ion abundances of 0.03 to prevent ions with small abundances from stopping the progression of the ionization parameter. This change in fractional abundances is found with

$$\frac{\Delta X_i}{X_i} = \frac{\overline{X_i^a} - \overline{X_i^b}}{\overline{X_i^a}}, \tag{2.2}$$

where X_i is the abundance of ion i and X_i^a and X_i^b are the averaged ion abundances. Only when all fractional ion abundances are below this cutoff value do we progress

21

to higher U. We vary the background with this range of U to match observational data from the COS-Halos survey (Werk et $al.$, 2014).

2.3   Results

2.3.1   General Features

The CGM is traced by a cool $T \lesssim 10^5$ K phase along with a hotter $T \gtrsim 10^6$ component (Tumlinson et $al.$, 2013; Werk et $al.$, 2014; Werk et $al.$, 2016; Prochaska et $al.$, 2017). The top row of Figure 3.4 shows the density-weighted temperature for all of our runs from left to right, $\sigma_{1D} = 26,\ 35,\ 46,\ 58$ km s^{-1}. We find that this density-weighted temperature falls within the range of temperatures observed in the CGM of nearby galaxies. We also look to match the large H I component observed in these systems and show the H I column density, $N_{\text{H I}}$, in the bottom row of Figure 3.4; finding that our results match the log $N_{\text{H I}} = 14 - 20$ cm^{-2} range found in Tumlinson et $al.$ (2013).

Figures 2.3 and 2.4 show temperature and ionic distributions from $nL = 10^{20}$ cm^{-2} simulations with log $U = -4$ and -2, respectively. Here, Si II and Si IV, which are commonly observed in the halos of low-redshift galaxies (Werk et $al.$, 2013; Borthakur et $al.$, 2016; Heckman et $al.$, 2017), are chosen to sample low and intermediate ionization state material, respectively. O VI, on the other hand, serves to sample the higher ionization state material, commonly observed in the halos surrounding L_* galaxies (W16, Oppenheimer et $al.$, 2016), and likely arising from interactions between different phases as caused by processes that inject energy and material into the CGM (e.g. Hummels et $al.$, 2013; Shen et $al.$, 2013; Ford et $al.$, 2016; Gutcke et $al.$, 2017; Hani et $al.$, 2018; Liang et $al.$, 2018; Nelson et $al.$, 2018a). Finally, N V, which has an ionization potential slightly below O VI, is chosen because it is nearly absent in the
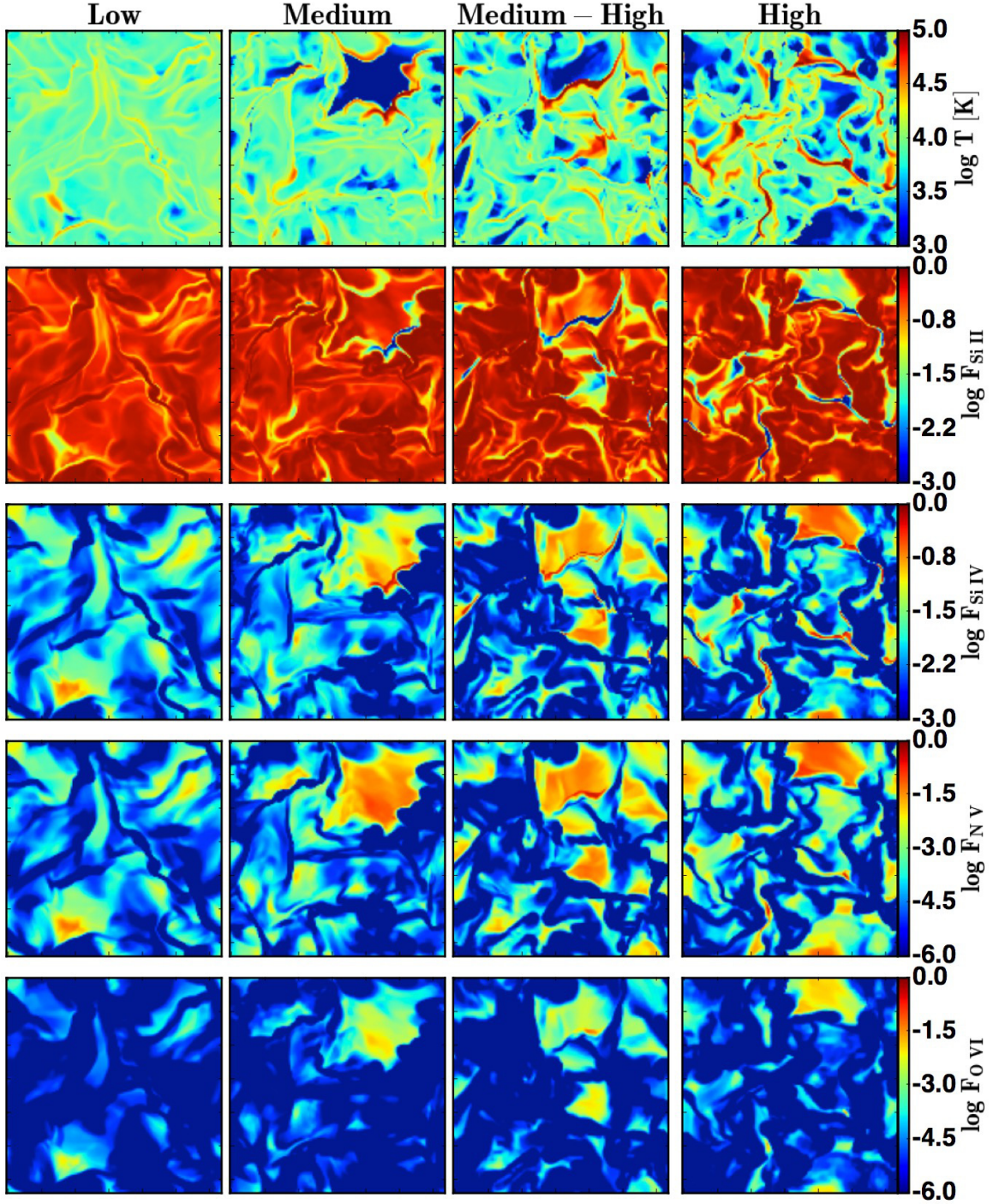
Figure 2.3: Temperature (first row), Si II (second row), Si IV (third row), N V (fourth row), and O VI (bottom row) slices for $\sigma_{1D} = 26$ (Low), 35 (Medium), 46 (Medium-High), and 58 (High) km s^{-1} at log $U = -4$. Each column gives slices from the aforementioned turbulence run.
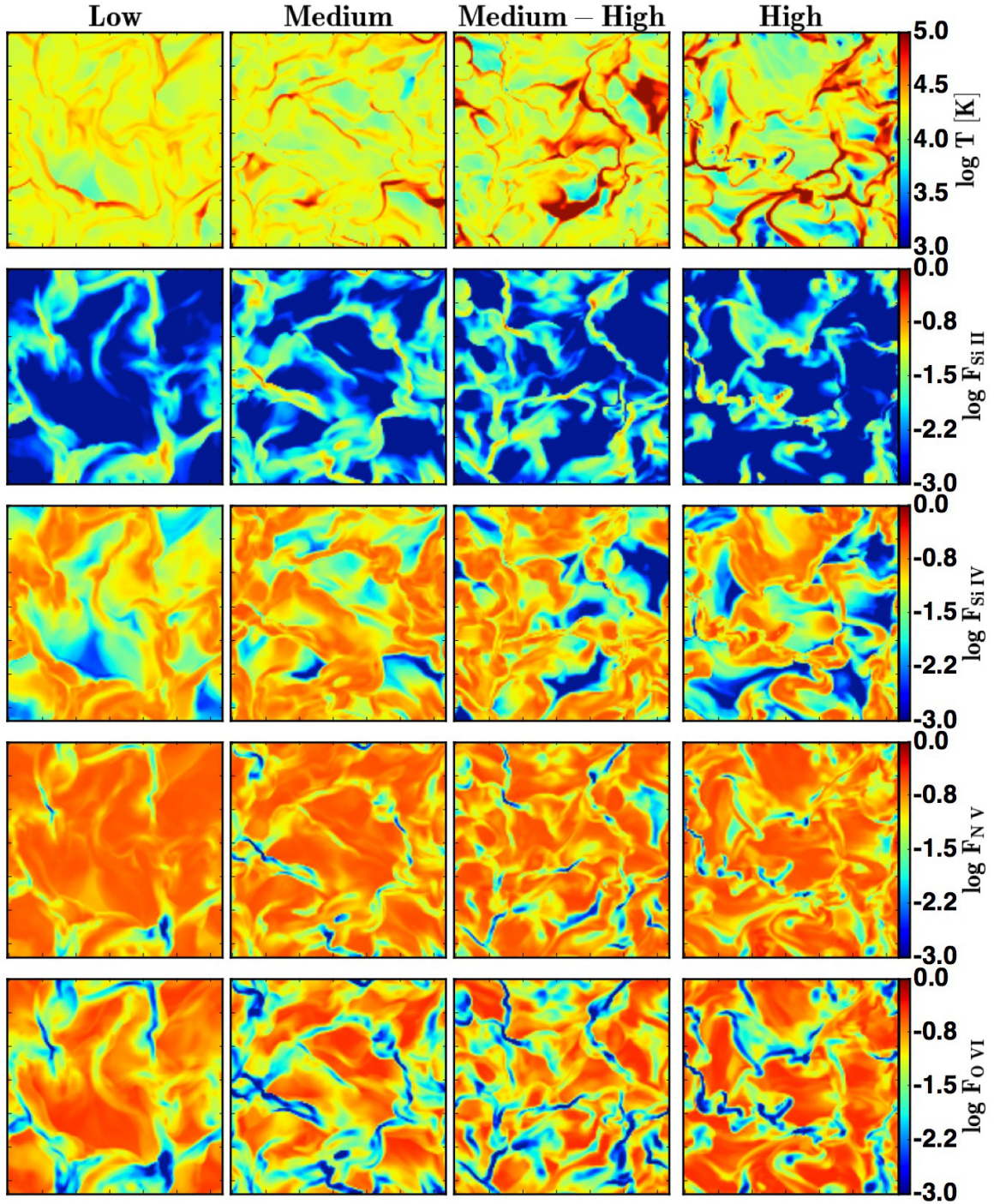
Figure 2.4: Temperature (first row), Si II (second row), Si IV (third row), N V (fourth row), and O VI (bottom row) slices for $\sigma_{1D} = 26$ (Low), 35 (Medium), 46 (Medium-High), and 58 (High) km s^{-1} at $\log U = -2$. Each column gives slices from the aforementioned turbulence run.
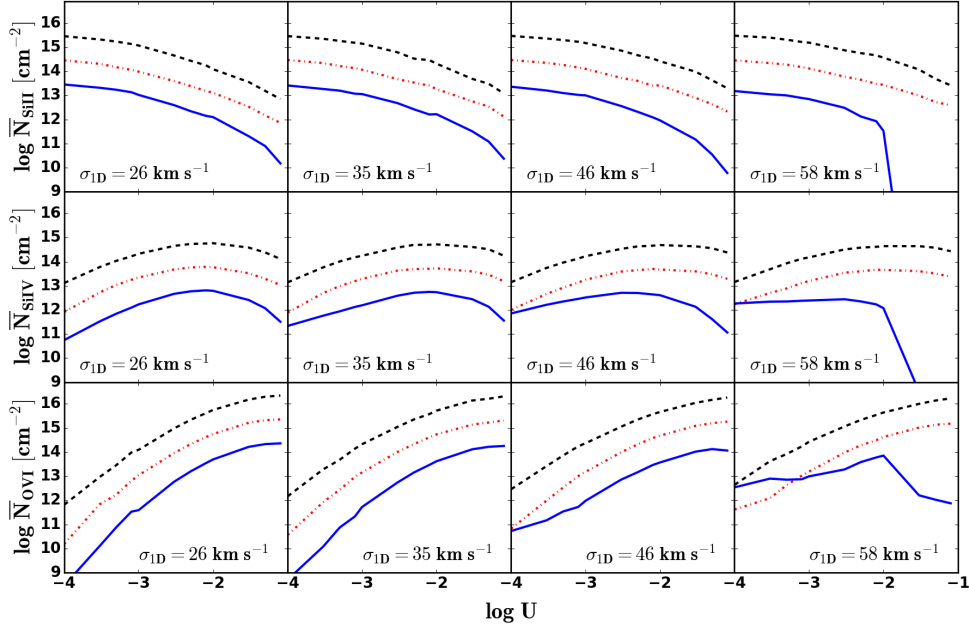
Figure 2.5: log $N_{\text{Si II}}$ (first row), log $N_{\text{Si IV}}$ (second row), and log $N_{\text{O VI}}$ (third row) vs log U for the $nL = 10^{19}$ (solid blue), 10^{20} (dotted-dashed red), and 10^{21} (dashed black) cm^{-2} runs. From left to right, $\sigma_{1D} = 26$, 35, 46, 58 km s^{-1}.

CGM of star-forming galaxies for reasons that remain to be determined.

At lower turbulent velocities ($\sigma_{1D} < 26$ km s^{-1}), the gas is subsonic, yielding weak shocks and small temperature gradients, which ensures that the medium is dominated by a single ionization state material. Low ions, defined to be singly ionized metals, dominate if log U = -4 while intermediate ions dominate in the log U = -2 case. We also begin to see larger temperature gradients as this turbulence is increased, caused by stronger shocks, which sweep across cells carrying newly ionized material. An example of this appears in the upper-right corner of the Medium-High run in Figure 2.3, which features a downward shock that leaves N V and O VI in its wake.
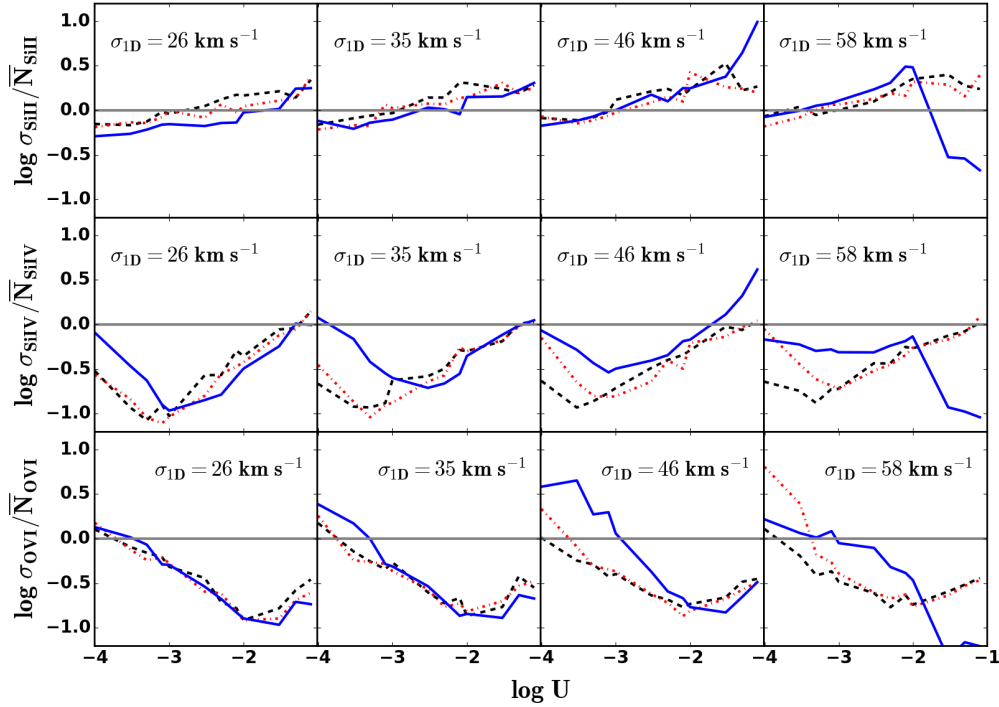
Figure 2.6: log $\sigma_{\mathrm{SiII}}/\overline{N}_{\mathrm{SiII}}$ (first row), log $\sigma_{\mathrm{SiIV}}/\overline{N}_{\mathrm{SiIV}}$ (second row), and log $\sigma_{\mathrm{OVI}}/\overline{N}_{\mathrm{OVI}}$ (third row) vs. log U, for $\sigma_{\mathrm{1D}} = 26, 35, 46,$ and 58 km s^{-1} (from left to right). Normalized standard deviations from the $nL = 10^{19}$ cm^{-2} are plotted in solid blue, $nL = 10^{20}$ cm^{-2} in dotted-dashed red, and $nL = 10^{21}$ cm^{-2} in dashed black. The solid gray line is shown to indicate a normalized standard deviation of one.

2.3.2 Low and Intermediate Ionization State Ions

The mean of their respective column densities of Si II, Si IV, and O VI are shown in Figure 2.5. As mentioned previously, the turbulent state of the medium and its background determine the dominant ionization state. However, sight lines of N V and O VI in the lower background case, and Si II remains in the higher background case with mass fractions of a few percent, which correspond to column densities of $N_{\mathrm{col}} \lesssim 10^{14}$ cm^{-2}. Observationally, low ionization-state ions tend to be more clumpy (Pieri *et al.*, 2014) and congregate in the inner halo of a galaxy (Liang and Chen, 2014) while more highly ionized metals are more abundant in the outer CGM (W16;

Johnson *et al.*, 2015; Oppenheimer *et al.*, 2016, 2017). This translates to the Low and Medium runs being more comparable to conditions of the inner CGM while the Medium-High and High runs are more representative of the outer CGM.

Werk *et al.* (2013) find low ionization-state ions (C II, Si II, Mg II, etc.) to have column densities that vary by orders of magnitude, in contrast to the less variable O VI column densities, suggesting a patchy CGM. This is seen in the Figure 2.4, as turbulence causes the low ionization-state ions, as traced by Si II, to congregate into clumps.

To measure the 'clumpiness' of low ionization-state ions, we computed a normalized standard deviation of the Si II, Si IV, and O VI column densities for all of our runs shown in Figure 2.6. We find N_{SiII} to have the highest average normalized standard deviation, while also having the weakest dependence on the mean density of the medium parameterized by nL. We further point out that this patchiness evolves as the turbulence is increased; such that higher turbulent velocities tend to move the low ionization-state ions into denser clumps.

The intermediate and higher ionization-state ions also tend to evolve as the turbulence is increased, and they depend more on the strength of the background radiation field. Specifically, Si IV has a minimum normalized standard deviation at lower U, at values at which the total Si IV column density is highest. As the ionizing background increases, these intermediate ions congregate into filaments, as shown in Figure 2.4, showing more patchy behavior. Finally, the normalized standard deviation of O VI decreases monotonically as a function of increasing turbulence.

2.3.3   *N V and O VI*

In Figure 2.7 we show the average N V column density, $N_{\mathrm{N\,V}}$ (top row), O VI column density, $N_{\mathrm{O\,VI}}$ (middle row), and the ratio of $N_{\mathrm{N\,V}}$ to $N_{\mathrm{O\,VI}}$ (bottom row) as
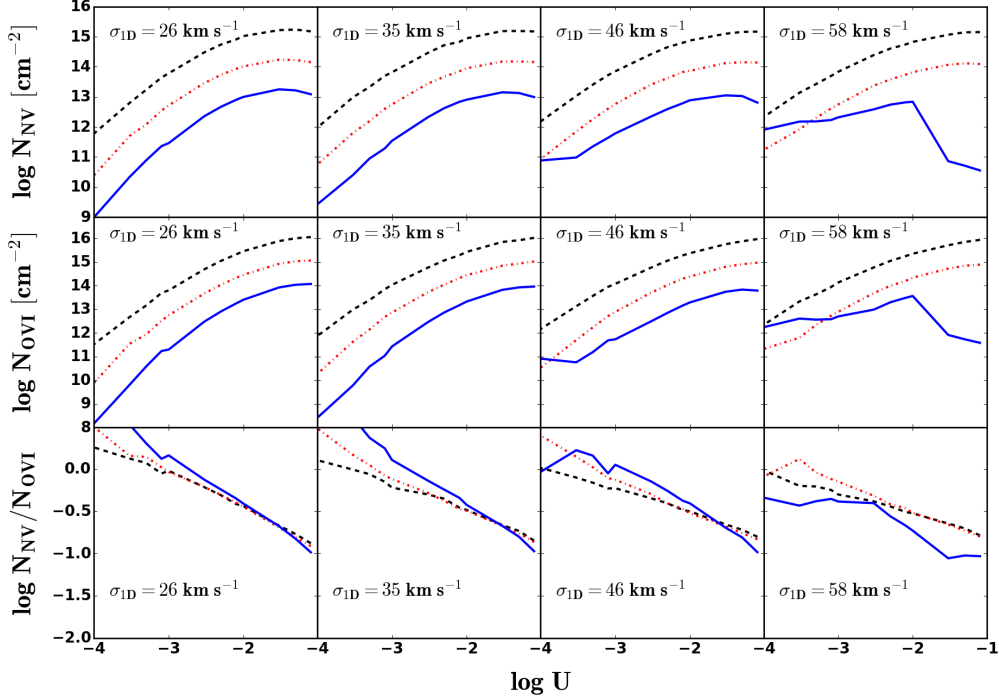
Figure 2.7: $\log N_{\text{N V}}$ vs. $\log U$ (top row), $\log N_{\text{O VI}}$ vs. $\log U$ (middle row), and $\log N_{\text{N V}}/N_{\text{O VI}}$ vs. $\log U$ (bottom row) for the $nL = 10^{19}$ (solid blue), 10^{20} (dotted-dashed red), and 10^{21} (dashed black) cm^{-2} runs. From left to right, $\sigma_{1D} = 26, 35, 46, 58$ km s^{-1}.

a function of the ionization parameter. Here we see that the N V column densities tend to be slightly higher than those of O VI at low U. This trend continues until a higher turbulent state is reached ($\sigma_{1D} \geqslant 46$ km s^{-1}), at which point $N_{\text{O VI}} \geqslant N_{\text{N V}}$ at the lowest U. We also see that $N_{\text{N V}}$ seems to increase at a slower rate than $N_{\text{O VI}}$ allowing for a lower $N_{\text{N V}}$ to $N_{\text{O VI}}$ ratio at higher U.

As the turbulence approaches supersonic speeds, both the minimal $N_{\text{N V}}$ and $N_{\text{O VI}}$ increase for each run while eventually reaching a maximum at the highest U. However, at $\sigma_{1D} \geqslant 58$ km s^{-1}, the $nL = 10^{19}$ cm^{-2} run experiences a peak in N V and O VI at $\log U \approx -2$. Following this, these ions undergo a sharp decline in abundance. Turbulence seems to lower both the $N_{\text{N V}}$ and $N_{\text{O VI}}$ gradients across U allowing for

larger column densities to be found at lower U.

The overall density of the gas sampled is important in determining the ionization state and $N_{\text{O VI}}$. This becomes even more important as the medium becomes more turbulent. W16 find log $N_{\text{O VI}}$ to have a median value of $10^{14.5}$ cm^{-2} for nearby star-forming galaxies. Looking at the $\sigma_{1D} = 58$ km s^{-1} plot in the middle row of Figure 2.7, we see that depending on the total density of the medium, an O VI column density of $10^{14.5}$ cm^{-2} may be found anywhere between $-3 < \log U < -2$.

We continue to compare our results to those found in W16 by plotting the column density ratio N V/O VI as a function U in Figure 2.7. As the turbulence increases, this ratio tends to flatten while never reaching 0.1. However, W16 find their sample to have a median value of ≈ 0.1 while noting most of their ratios to be upper bounds due to the non-detection of N V in the bulk of associated O VI components.

In Figure 2.8, we replicate Figure 12 in W16 by plotting the log $N_{\text{Si IV}}/N_{\text{O VI}}$ versus log $N_{\text{N V}}/N_{\text{O VI}}$. We have overlaid our derived ratios with matched Si IV, N V, and O VI components from W16. Here we see that turbulence moves this curve slightly leftward toward the data but not nearly enough to match the majority of the data, which require much lower levels of N V.

The nonnegligible amount of N V present in isotropic turbulence may be due to two reasons: electron collisional ionization from the shocks, and the constraints imposed by isotropy.

The temperature associated with a shock within the high turbulence run is $\approx 10^5$ K ≈ 10 eV. At this temperature, the recombination rate coefficient for the primary N V to N IV reaction, N^{4+} + e^- = N^{3+}, is much lower than the primary O VI to O V reaction, O^{5+} + e^- = O^{4+}. This means that N V survives longer than O VI.

However, as the ionization potentials of N IV and O V are 77 and 114 eV, respectively, even in the high turbulence case it is only the strongest shocks that are able
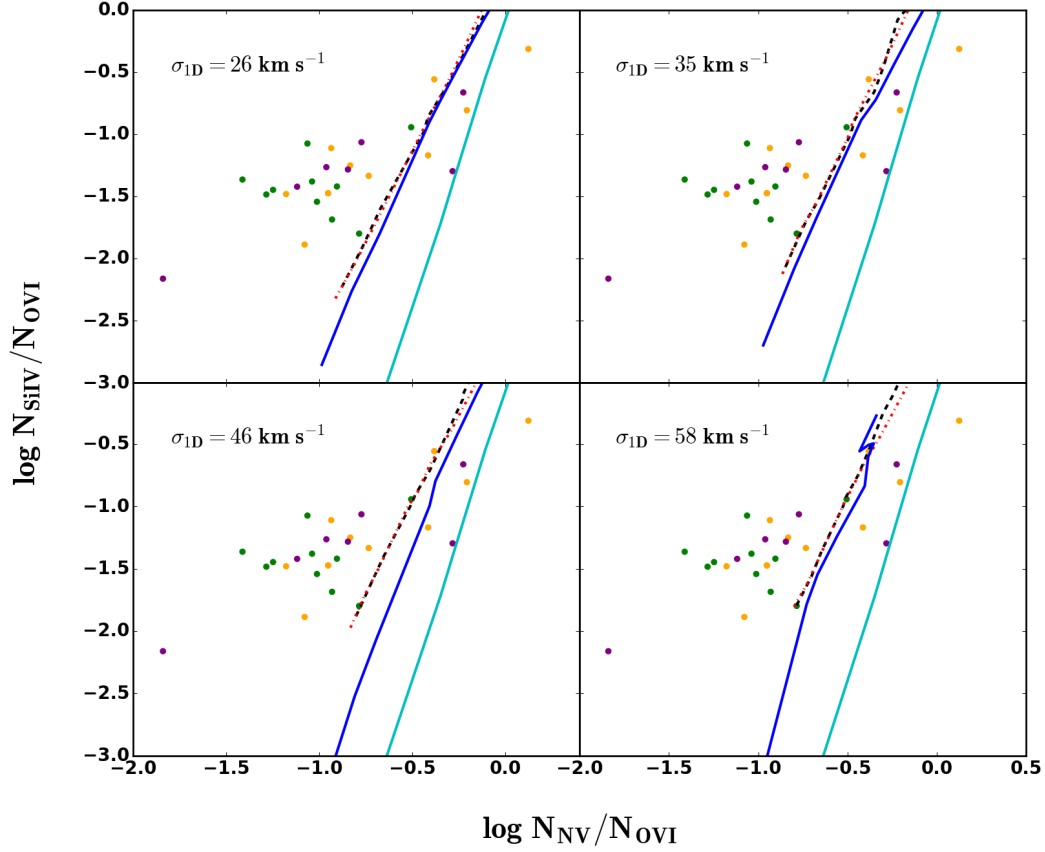
Figure 2.8: $\log N_{\text{Si IV}}/N_{\text{O VI}}$ vs $\log N_{\text{N V}}/N_{\text{O VI}}$ for the $nL = 10^{19}$ (solid blue), 10^{20} (red dotted-dashed), and 10^{21} (black-dashed) cm^{-2} runs. From left to right, $\sigma_{1D} = 26$, 35 km s^{-1} (top row) and 46, 58 km s^{-1} (bottom row). These are overlaid on the matched Si IV, N V, and O VI components from W16 Figure 12. Green circles represent the "broad" type O VI absorption, orange circles are "narrow" type absorbers, and purple circles are "no-low" type absorbers. As a reference, we plot a single-zone CLOUDY model photoionized by an HM2012 EUVB (solid cyan) with $-4 < \log U < -1$.

to produce N v and O vi, with N v being produced more efficiently than O vi. On the other hand, the ionization potential of N v is only 98 eV, while the ionization potential of O vi is 138 eV. This means it is easier to covert N v into N vi than it is to convert O vi to O vii and that the small value of $N_{\text{N v}}/N_{\text{O vi}}$ observed in star-forming galaxy halos must be caused by the production of N vi. However, this would require even stronger shocks, which are not sustainable in an isotropic environment.

Instead, moving to isotropic turbulence levels above $\sigma_{1D} \approx 60$ km s^{-1} causes a thermal runaway. This is because the strongest shocks in such a situation produce ions that cool much less efficiently than those found at $\approx 10^5 K$, and this inefficiency of cooling increases at higher temperatures. Thus, no steady-state condition can be achieved (Gray *et al.*, 2015; Gray and Scannapieco, 2016).

Note however that such levels of continuous turbulence are compatible with an overall steady state in an anisotropic environment, as could occur if turbulence occurred within strongly stratified medium. In this case, thermal runaway may be avoided as hot material cycles convectively upwards in the gravitational potential while a region of efficient cooing remains near the center (e.g. Scannapieco *et al.*, 2012; Sur *et al.*, 2016). This remains a promising possibility for explaining the $N_{\text{N v}}/N_{\text{O vi}}$ observations, but it requires spanning a considerably larger parameter space than the general isotropic case considered in this study.

2.4   Discussion & Summary

Turbulence may be present in the CGM due to outflowing and inflowing processes that inject energy, momentum, and material into the surrounding medium. Recent observations of the CGM's surrounding nearby star-forming galaxies find low ionization-state ions (C ii, Si ii, Mg ii, etc.) with column densities that vary by orders of magnitude, substantial O vi absorption, and very small amounts of N v.

This motivated us to simulate an isotropic turbulent medium exposed to an HM2012 EUVB to see how ion abundances change under these conditions and whether isotropic turbulence can resolve this N v and O vi anomaly.

To test the effect of isotropic turbulence on ion abundances, we have conducted a suite of numerical simulations of a turbulent astrophysical medium exposed to an extra-galactic background using MAIHEM. We first test MAIHEM in CGM-like conditions and find nice agreement between these tests and CLOUDY results.

We then detail our results, finding that turbulence is effective at producing density and temperature gradients that span nearly two orders of magnitude. Using Si ii, Si iv, and O vi, as samples for low, intermediate, and high ions, respectively, we show that a moderate amount of turbulence ($\sigma_{1D} = 26$ km s^{-1}) is able to produce a medium dominated by multiple ionization states. In these runs, subdominant species still maintain sight lines with fractional abundances at the percent level, low ionization-state species are congregated into clumps, and medium and high ionization-state species are more widespread.

We go on to investigate O vi and N v as well as compare our results to those in W16 finding that although we are able to produce larger O vi column densities at lower U, we also produce N v at a level comparable to that of O vi, showing that isotropic turbulence is not able to match all observations of nearby star-forming CGM.

We speculate on this and conclude it to be a consequence of the shocks present within higher turbulent runs, which causes a thermal runaway if the velocity dispersion is increased above the values reported here. This is partially a consequence of the assumption of an isotropic medium, which causes shocks and the energy they carry to be spread throughout the entire volume.

We also look at the recombination and ionization rate coefficients for the relevant

reactions and find N v is produced faster and lives longer than O vi. In addition to this, N v is ionized faster than O v leading us to conclude that N v present in the CGM of star-forming galaxies is able to quickly ionize to N vi leaving little trace of N v.

In a future paper, we will modify MAIHEM with the addition of gravity to simulate a stratified medium. We predict that this will allow for more effective cooling at higher velocity dispersions, a situation that may be important in resolving the origin of the discrepancy between O vi and N v.

Chapter 3

MODELING PHOTOIONIZED TURBULENT MATERIAL IN THE
CIRCUMGALACTIC MEDIUM II: EFFECT OF TURBULENCE WITHIN A
STRATIFIED MEDIUM

This chapter is reproduced from the version published in 2020 in The Astrophysical Journal, Volume 896, Page 136, with permission from the co-authors.

3.1   Introduction

The circumgalactic medium (CGM) is a cloud of diffuse baryons that resides in the gravitational potential of a host galaxy. This medium extends hundreds of kpc, and it plays an essential role in facilitating the host galaxy's evolution through the transfer of baryons in processes such as accretion, galactic winds, and feedback from active galactic nuclei (AGN) (e.g. Lilly *et al.*, 2013; Voit *et al.*, 2015; Crighton *et al.*, 2015; Fox and Davé, 2017; Muratov *et al.*, 2017; Tumlinson *et al.*, 2017). Unfortunately, its diffuse nature makes this medium difficult to observe through emission.

Instead, our knowledge of the CGM relies on observations of absorption in the spectra of background quasars. Much of the earliest measurements of this type made use of the WFPC-2 camera on the *Hubble Space Telescope (HST)* as well as the HIRES spectrograph on the Keck telescopes, which allowed the capability for observations of distant, $z \approx 3$ systems. Steidel (1998) provides a summary of these early findings, which attempted to understand the relationship between galaxies, the CGM, and the intergalactic medium (IGM).

To gain further insight into this relation, the Keck Baryonic Structure Survey (KBSS; Rudie *et al.*, 2012) was undertaken to observe galaxies during the cosmic

peak of star-formation ($z \approx 2-3$). Theory tells us that these higher-redshift systems should be actively accreting material through cold filamentary structures to fuel the high star formation rates observed (e.g. Birnboim and Dekel, 2003; Ocvirk *et al.*, 2008; Brooks *et al.*, 2009; Faucher-Giguère and Kereš, 2011). Rudie *et al.* (2012) revealed this cooler material in H I absorption as well as an anti-correlation between H I absorbers and transverse distance to the host galaxy, otherwise known as the impact parameter.

At low resdshift, the CGM has been probed with multiple generations of HST instruments. Using the Faint Object Spectrograph (FOS), Chen *et al.* (1998, 2001a,c) was able to derive constraints on high equivalent width H I and C IV absorbers in the CGM around $z < 1$ galaxies. More recently, the Cosmic Origins Spectrograph (COS) has given us increased sensitivity to the diffuse absorption (Shull, 2009). Using this instrument, Tumlinson *et al.* (2013) observed the CGM of $z \lesssim 0.5$, $M_* = 10^{9.5} - 10^{11.5}$ M$_\odot$ galaxies out to an impact parameter of $b = 150$ kpc in the COS-Halos survey. The survey showed a neutral H component associated with nearly every galaxy, along with large amounts of O VI absorption in the CGM of star-forming galaxies that was not observed in the non star-forming sample.

Werk *et al.* (2013) and Werk *et al.* (2016, hereafter W16) expanded on the COS-Halos survey and found absorption from singly ionized species resulting from a cooler ($T \approx 10^4 - 10^5$ K) CGM phase. This absorption was found to decrease with impact parameter similarly to earlier trends observed in H I. Furthermore, W16 found O VI absorption in sightlines at a variety of impact parameters and used them to trace the hot ($T \gtrsim 10^{5.5}$) ambient medium. N V absorption, however, was largely absent, an odd finding as the ionization potentials for these ions differs by only $\approx 30\%$.

W16 also included examinations of a variety of models to explain these findings (Gnat and Sternberg, 2007, 2009; Wakker *et al.*, 2012; Ferland *et al.*, 2017), but, to fit

the data,these either required unphysical conditions for the gas or a narrow range in parameter space. Motivating by these issues, in Buie *et al.* (2018, hereafter Paper I) we undertook a comprehensive investigation of the impact of homogeneous turbulence on the properties of the CGM.

Several CGM processes that are likely to drive significant turbulence. Theoretical work supported by observations shows distinctly cooler material flowing into star-forming galaxies (Kereš *et al.*, 2005; Dekel and Birnboim, 2006; Kereš and Hernquist, 2009; Stewart *et al.*, 2011; Rubin *et al.*, 2012). This cooler material will drive turbulence along the boundaries between it and the hotter ambient halo, and possibly throughout the entire medium.

Many galaxies also display global outflows, which inject material, momentum, and energy into the surrounding medium. These outflows are typically driven by supernovae resulting from ongoing star-formation (Veilleux *et al.*, 2005, for a review). Observations of this outflowing gas reveal complex multiphase features with γ and X-ray emission from 10^8–10^7 K plasma (Strickland and Heckman, 2007, 2009; Laha *et al.*, 2018) and UV absorption from 10^6–10^4 K material (Rubin *et al.*, 2014; Fox *et al.*, 2015; Heckman *et al.*, 2017).

Finally, dynamical friction resulting from the gravitational interactions between the CGM and dark matter subhalos may also lead to turbulent motions, as gas is accelerated in the wake of moving gravitational potentials Chandrasekhar (1943). As this material loses angular momentum and energy, it will merge with its host halo, although the merging timescales for these events depend on treatments of the orbital energy, angular momentum, and subhalo mass (e.g. Kauffmann *et al.*, 1993; Somerville and Primack, 1999; Boylan-Kolchin *et al.*, 2008).

In Paper I, we modeled the non-equilibrium chemical evolution of homogeneous turbulent media exposed to the extragalactic UV background (EUVB). We found

that a one-dimensional (1D) velocity dispersion of $\sigma_{1D} \approx 60$ km s^{-1} replicated many of the observed features within the CGM, such as clumping of low ionization-state ions and the existence of O VI at moderate ionization parameters. However, unlike observations, N V arose in our simulations with derived column densities of a similar magnitude to those of O VI. We also found that increasing the turbulent velocity dispersion led to a thermal runaway, resulting in a media not representative of the CGM around star-forming galaxies.

To gain a more realistic picture of turbulent systems, here we conduct direct numerical simulations of a stratified turbulent astrophysical media contained within a gravitational potential. We compare these results directly with observations to determine the extent to which multiphase observations of the CGM can be explained by the presence of sustained, stratified turbulence.

The paper is organized as follows: in Section 3.2 we outline the code used to model the CGM. In Section 3.3 we present our results with a focus on O VI and N V abundances as well as compare our results to W16 and in Section 3.4 we discuss the observational constraints on turbulence and the energy requirements for our turbulence while providing comparisons to real drivers of such turbulence. Finally, in Section 3.5 we give our concluding remarks.

3.2 Methods

3.2.1 The MAIHEM Code

We used Models of Agitated and Illuminated Hindering and Emitting Media (MAIHEM[1]) to simulate a stratified turbulent CGM. MAIHEM is a three-dimensional (3D) cooling and chemistry package built using FLASH (Version 4.5), an open-source

---

[1]http://maihem.asu.edu/

hydrodynamics code (Fryxell *et al.*, 2000). This package evolves the non-equilibrium chemistry network of 65 ions, including hydrogen (H I and H II), helium (He I–He III), carbon (C I–C VI), nitrogen (N I–N VII), oxygen (O I–O VIII), neon (Ne I–Ne X), sodium (Na I–Na III), magnesium (Mg I–Mg IV), silicon (Si I–Si VI), sulfur (S I–S V), calcium (Ca I–Ca V), iron (Fe I–Fe V), and electrons. This includes solving for dielectric and radiative recombinations, collisional ionizations with electrons, charge transfer reactions, and photoionizations by a UV background.

This package was first developed in Gray *et al.* (2015) and later improved upon with the inclusion of an ionizing background in Gray and Scannapieco (2016). Most recently, in Gray and Scannapieco (2017), several charge transfer reactions, radiative recombination rates, and dielectronic recombination rates from Aldrovandi and Pequignot (1973); Shull and Van Steenberg (1982); Arnaud and Rothenflug (1985) and photoionizing and photoheating rates from Verner and Yakovlev (1995) and Verner *et al.* (1996) were added and updated in the code.

The equations solved by MAIHEM are given in Gray and Scannapieco (2016) and are invariant under the transformation $x \rightarrow \lambda x$, $t \rightarrow \lambda t$, $\rho \rightarrow \rho/\lambda$ meaning the final steady-state abundances depend only on the mean density multiplied by the driving scale of turbulence, nL, the one-dimensional (1D) velocity dispersion of the gas, σ_{1D}, and the ionizing EUVB radiation which may be parameterized by U; the ratio of number of ionizing photons to the number density of hydrogen n_H, or alternatively,

$$U \equiv \frac{\Phi}{n_H c}, \tag{3.1}$$

where Φ is the total photon flux of ionizing photons, and c is the speed of light.

In addition, we used an unsplit solver based on Lee (2013) to solve the hydrodynamic equations. Here we made use of a hybrid Riemann solver that uses the Harten Lax and van Leer (HLL) solver (Einfeldt *et al.*, 1991) in places with strong shocks or

rarefactions and the Harten–Lax–van Leer–Contact (HLLC) solver (Toro *et al.*, 1994; Toro, 1999) in smoother flows to stabilize the code as turbulence ensues. We refer the reader to Gray *et al.* (2015) and Gray and Scannapieco (2016) for further details.

3.2.2 Turbulence and Gravity

We modeled turbulence driven through solenoidal modes ($\nabla \cdot F = 0$) (Pan and Scannapieco, 2010). These modes depend on the driving scale of turbulence and undergo a direct Fourier transformation to the physical space and are added to the acceleration. The acceleration was varied with radii as

$$a_{x,y,z} = a^0_{x,y,z} \left(\frac{r + 0.3R_{\text{vir}}}{0.5R_{\text{vir}}} \right)^{\alpha}, \tag{3.2}$$

where $a^0_{x,y,z}$ is the original acceleration term resulting from the direct Fourier transform, r is the radius to a cell, R_{vir} is the virial radius of the halo, and α is a dimensionless parameter that controls how the acceleration behaves with radius. We set $\alpha = -1$ such that stirring was strongest towards the center and falls off with radius to capture the behavior of star-forming galaxies.

Furthermore, we added a dark matter halo to produce a stratified baryonic matter density profile in these simulations that assumes a (Navarro *et al.*, 1996, hereafter NFW) profile under the ΛCDM model.

$$\rho(r) = \frac{\rho_0}{\frac{r}{R_s} \left(1 + \frac{r}{R_s}\right)^2}, \tag{3.3}$$

where $\rho_0 = M_{\text{halo}} \left[4\pi R_s^3 \left[\ln(1 + c) - c/(1 + c) \right] \right]^{-1}$ is the central dark matter density, M_{halo} is the mass of the halo, $R_s = R_{\text{vir}}/c$ is the scale radius, and c is the concentration parameter of the halo.

This dark matter halo was also used to generate the gravitational acceleration of the baryonic matter. The cosmological parameters used in this work are from the
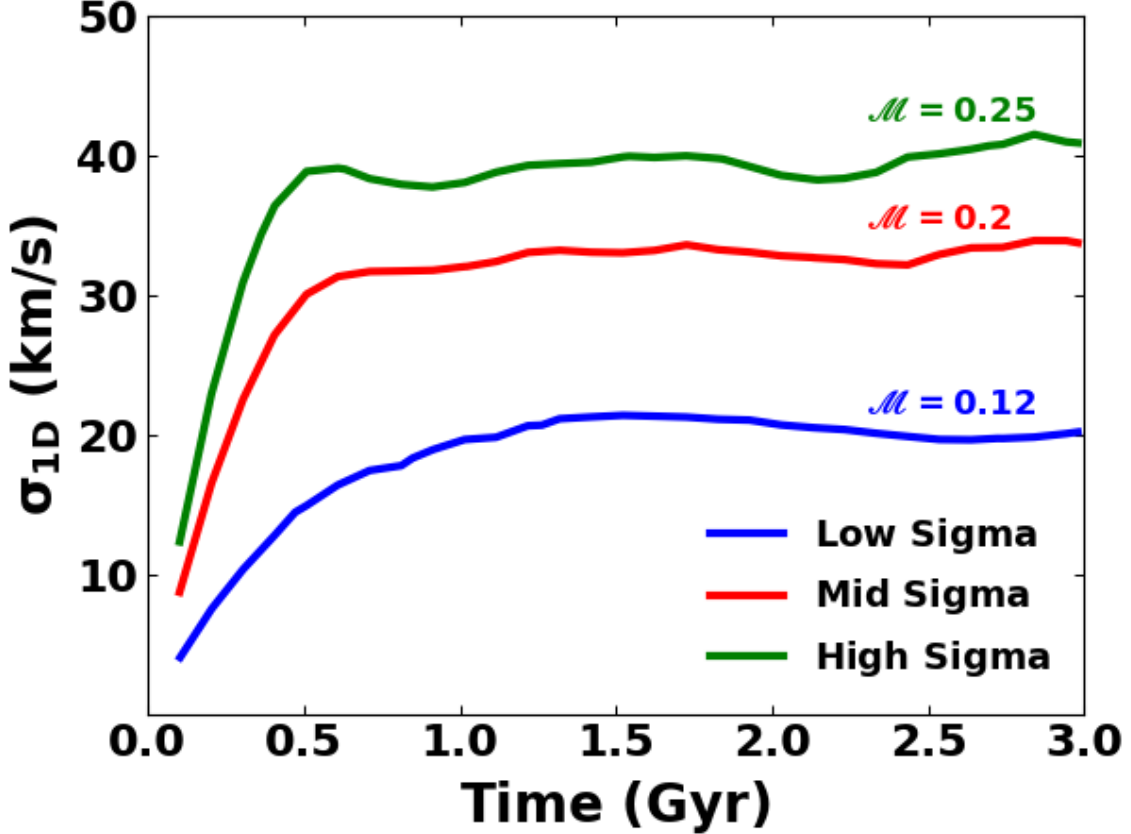
Figure 3.1: 1D velocity dispersion (σ_{1D}) vs. time for the Low (blue), Mid (red), and High (green) runs. We also show the 1D Mach number, $\mathcal{M}$, at 3 Gyrs for the runs in the same colors as their σ_{1D} curves.

Planck 2018 Collaboration (Aghanim *et al.*, 2018) and are $h = 0.674$, $\Omega_m = 0.315$, $\Omega_b = 0.049$, and $\Omega_\Lambda = 0.685$, where h is the Hubble constant in units of 100 km s^{-1} Mpc^{-1}, and Ω_m, Ω_b, and Ω_Λ, are the total matter, baryonic, and vacuum densities, respectively, in units of the critical density.

3.2.3   Model Parameters

We conducted a suite of simulations that assumed a Milky Way mass dark matter halo of $M = 10^{12}$ M$_\odot$, with a virial radius of 220 kpc and a concentration parameter of 10. The medium was initialized with a fractional ion abundance at 0.3 Z$_\odot$ metallicity
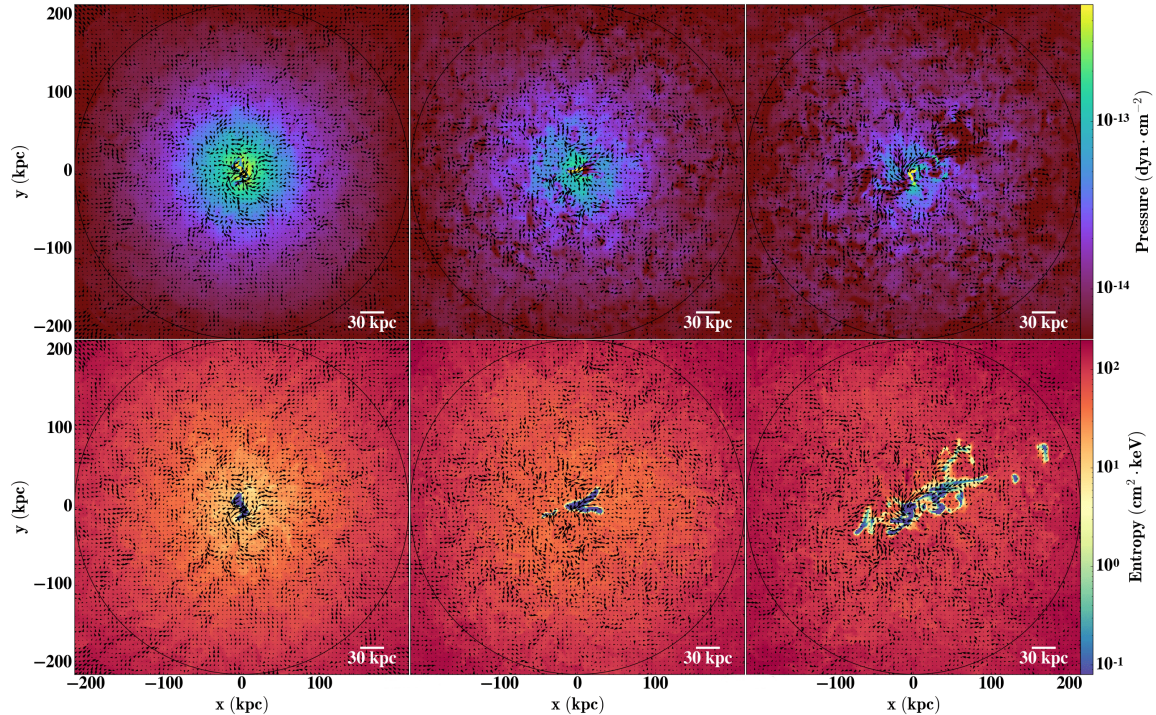
Figure 3.2: Slices at 3 Gyrs along the z-axis showing the Pressure (top row) and Entropy (bottom row) for the Low (left), Mid (middle), and High (right) runs. The arrows show the $x - y$ velocity vectors of the flow and a black circle shows the virial radius at $R_{\text{vir}} \approx 220$ kpc. Note that the cooling streams seen in the Mid and High runs are much larger than the driving scale of the turbulence, and they arise as a result of the convective flow that is set up by the turbulent heating.

in collisional ionization equilibrium (CIE) at the virial temperature of the halo, $T = 1.2 \times 10^6$ K and average sound speed of 166 km s^{-1}. In all cases the material was assumed to be irradiated with a redshift zero Haardt and Madau (2012) (HM2012) EUVB whose specific intensity was normalized to 8.23×10^{-24} erg cm^{-2} s^{-1} Hz^{-1} sr^{-1} at the Lyman limit following the radio-quiet AGN spectral index ($\alpha = 0.157$). Note that our simulations assume chemical homogeneity, while observations indicate that the composition of the CGM is likely to be significantly inhomogeneous (Zahedy *et al.*, 2019). However, the impact of this additional factor is left for future investigation.

The simulations were carried out in an 800 kpc box with periodic boundaries using Static Mesh Refinement (SMR) to accurately capture important structures
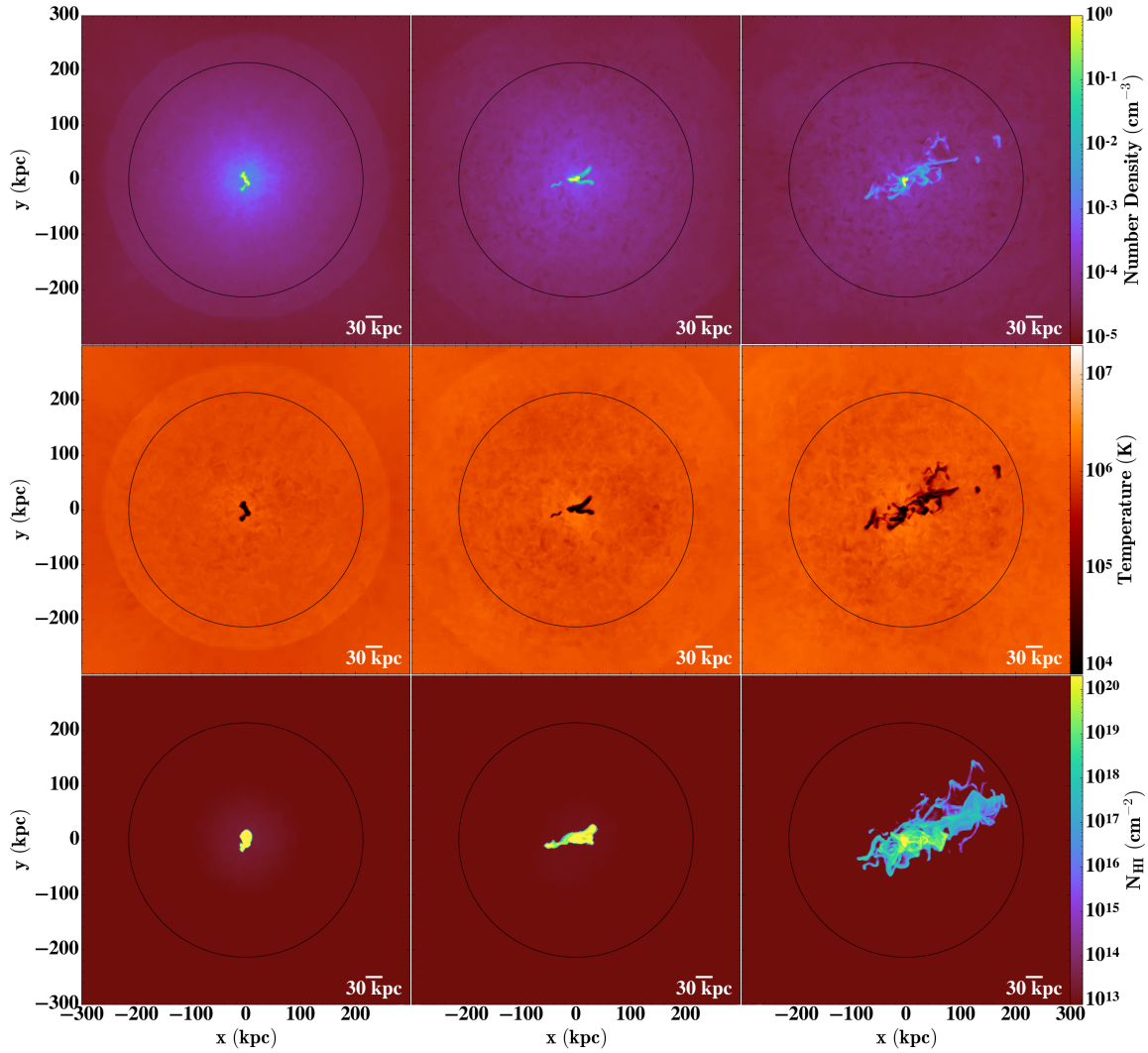
Figure 3.3: Slices at 3 Gyrs along the z-axis showing the number density (top row), temperature (middle row) along with $N_{\text{H\,I}}$ projections (bottom row) for the Low (left), Mid (middle), and High (right) runs. A black circle shows the virial radius at $R_{\text{vir}} \approx 220$ kpc.

that develop in the halo as turbulence ensues. Refinement begins at $\approx$ 300 kpc and continues into the center. The levels of refinement were as follows: for R $\gtrsim$ 300 kpc the domain was at a resolution of 64^3 which translates to 12.5 kpc, for $300 \gtrsim$ R $\gtrsim$ 250 kpc the resolution was 128^3 which translates to 6.2 kpc, $250 \gtrsim$ R $\gtrsim$ 225 kpc the resolution was 256^3 which translates to 3.1 kpc, and for 225 kpc $\gtrsim$ R the resolution was 512^3 which translates to 1.6 kpc.

The turbulence had stirring modes with wavenumbers between $L/3 \leqslant 2\pi/k \leqslant L$, where we choose L to be 30 kpc. This choice in driving scale is informed by the size of the Milky Way disk as we imagine the turbulence to be driven by outflowing and inflowing processes centered around the disk of the host galaxy. Each of our simulations was run for 3 Gyrs until it reached a global equilibrium such that the change in total energy was less than 0.25%.

We looked at 3 cases for the average σ_{1D}: 20, 34, and 41 km s^{-1} which we call the Low, Mid, and High runs respectively. These follow estimates of the non-thermal velocity components of line-width measurements from W16. In Figure 3.1 we show the volume-averaged σ_{1D} found by subtracting the infall velocity from the volume-averaged velocity within the virial radius of the halo along with their respective mach numbers computed as the ratio of σ_{1D} and the volume-averaged sound speed at 0 Gyr.

3.3   Results

3.3.1   Evolution

Initially, gas within $r \approx 30$ kpc cools over ≈ 100 Myrs, forming a low-pressure region in the center of the halo, which promotes an accretion flow. This results in an accretion shock that forms near the core and gradually moves outward. As turbulence develops, it starts to disrupt the flow, such that the cool gas near the
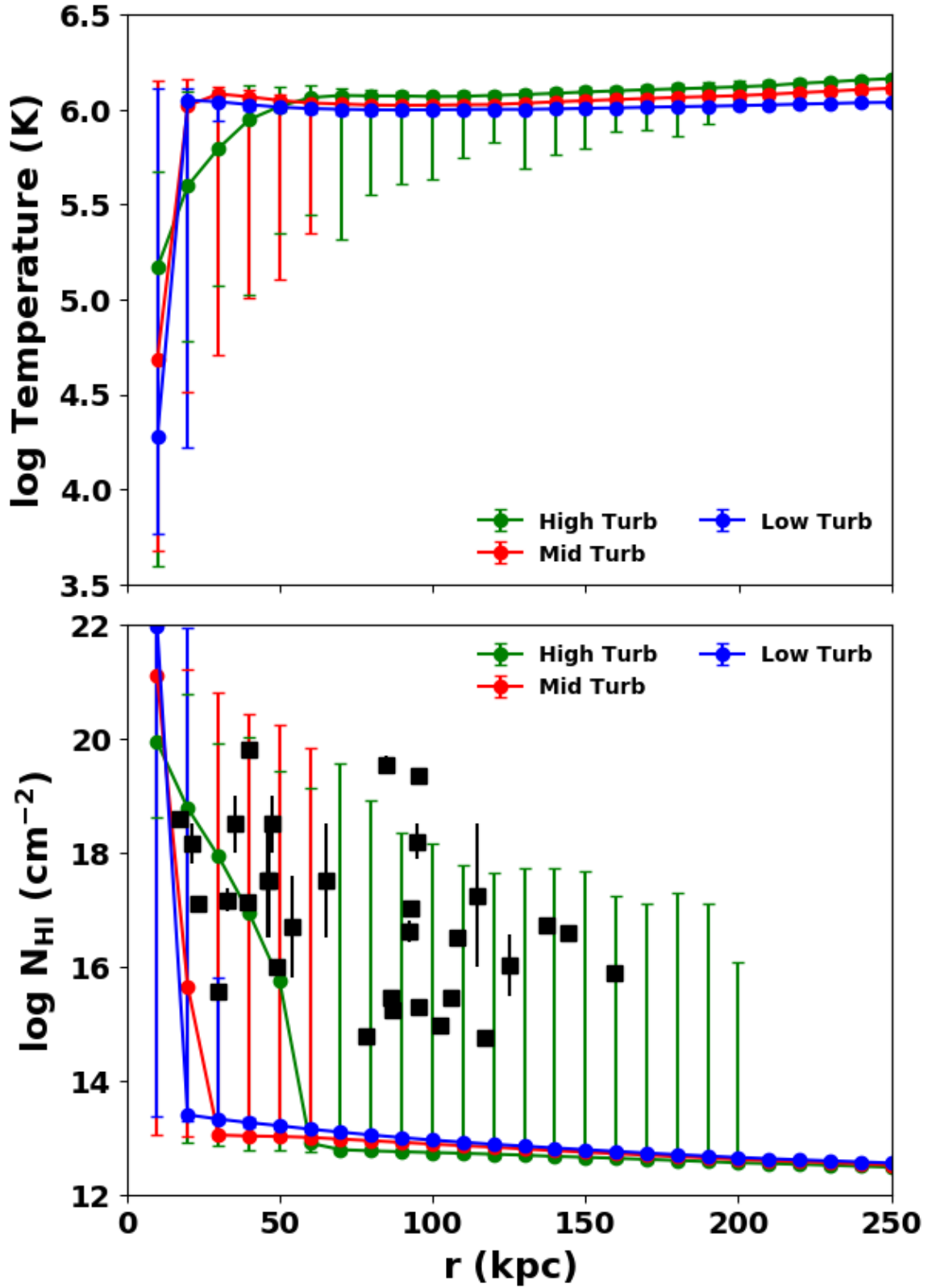
Figure 3.4: Filled circles show the 50th percentile of sightlines in 10 kpc bins for the log Temperature (top) and $N_{H\ I}$ (bottom) vs. radial distance r for the Low (blue), Mid (red), and High (green) runs at 3 Gyrs contained to cells within the virial radius. Error bars show the 1st percentile as the lower limit and 99th percentile as the upper limit. Projections were generated for each sightline as a line integral of the ion number density along the z-axis. The $N_{H\ I}$ data from the COS-Halos sample overlaid are on our projected columns in black.

center is anisotropic and filamentary. Turbulence also acts to stochastically heat the medium, creating buoyant patches of higher entropy gas that moves outward to replace the cooling inflowing gas. This sets up a convective flow that is most extended in the run with the highest level of turbulence.

This flow may be observed in Figure 3.2 which shows slices of the pressure and entropy at 3 Gyrs overlaid with black quivers that show the velocity field. Here we see that gas can flow inwards through the low pressure, low entropy structures into the center where it may cycle out of the center or simply collect there. These low pressure, low entropy structures house lower ionization state gas as we discuss in more detail below.

Note also that the Low run displays a profile that is close to spherically symmetric, while the Mid run develops low pressure/entropy systems near the center of the halo. Finally, the High run shows an extended convection flow that can naturally facilitate the development of low pressure/entropy systems at and beyond 100 kpc, forming low ionization state gas at large distances from the halo center.

This figure also illustrates how the overall entropy profile varies with increased levels of turbulence. In the Low run, the entropy increases strongly with radius, indicating a medium that is largely stable to convection. In the Mid run, on the other hand, the entropy is much more constant near the center, which hosts a limited convective region. Finally, the High run has the largest convective regions and a more gradual radial increase in entropy. This profile is the most similar to the CGM produced in the high mass loading star formation (SF) feedback model in Fielding *et al.* (2017, hereafter F17) as well as the model in Li and Tonnesen (2019) with a star formation rate of 3 $M_\odot$ yr^{-1} and the turbulent core simulations in Su *et al.* (2020). In the High run, higher entropy gas is found throughout the halo, intermixed with low-entropy gas. In between these two are layers of intermediate entropy gas

$(S \approx 10 \text{ keV cm}^{-2})$, which cools rapidly along the interfaces between the cold and hot material.

Overall we find all of the species in the simulations vary by $\lesssim 5\%$ for the last 100 Myrs of the runtime. The elements that are most out of equilibrium differ across the runs, however, we find Ne, Ca, and S to be common elements with the highest percentage difference from equilibrium. Of these, Ne is the least surprising, as it has the most ions that we track in our reaction network.

3.3.2 General Features

To give a more complete picture of the structure of the gas at 3 Gyrs, in Figure 3.3 we show slices of the number density and temperature, along with projections of $N_{\text{H I}}$ for each of our runs. Here as in Figure 3.2, the Low run shows a nearly spherically symmetric distribution. Furthermore the temperature distribution within the accretion shock is largely homogeneous, while density falls off strongly with radius. Meanwhile, the Mid and High cases, with their increased levels of turbulence, produce more structures within the halo. The High run, in particular, shows small clumps of cold $(T \approx 10^4 \text{ K})$ gas at nearly the virial radius of the halo, and a density profile that falls off more slowly with radius. We also see large amounts of H I constrained to the inner 30 and 60 kpc of the Low and Mid runs respectively, while the High run is turbulent enough to facilitate cool, inflowing H I out to 200 kpc, as seen in the positive x/y quadrant.

In Figure 3.4, we show the density-weighted temperature and $N_{\text{H I}}$ taken as the 50th percentile of the spread in 10 kpc bins vs. radial distance r, where projections are integrated along the z-axis, as compared to observations from the COS-Halos sample. The median density-weighted temperature does not vary significantly from the equilibrium temperature of the halos, however, the increased levels of turbulence
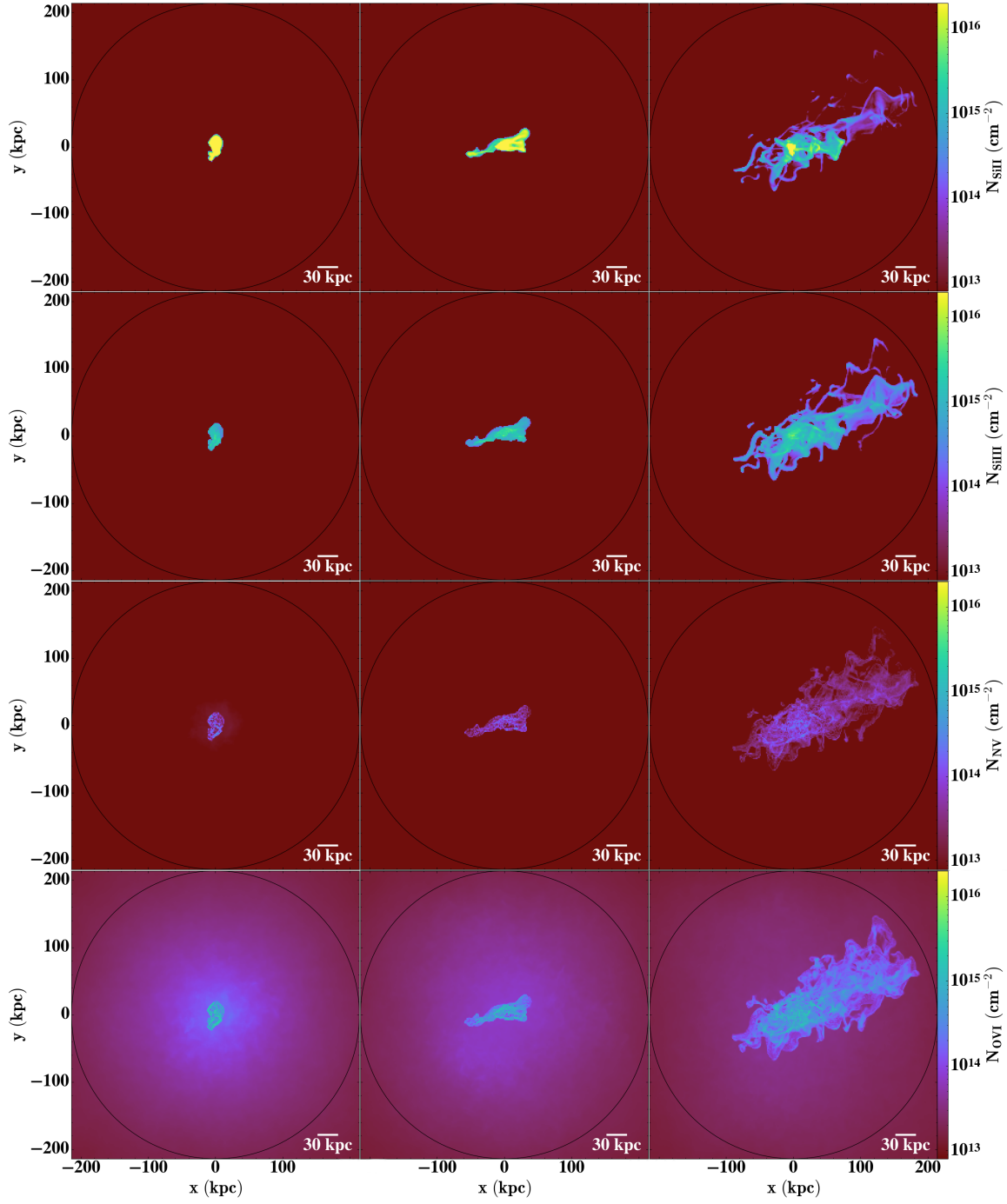
Figure 3.5: $N_{\text{Si II}}$ (first row), $N_{\text{Si III}}$ (second row), $N_{\text{N V}}$ (third row), and $N_{\text{O VI}}$ (fourth row) projections for the Low (left column), Mid (middle column), and High (right column) runs. In all panels, the black ring shows the virial radius at $r \approx$ 220 kpc.

yield a wider spread in the temperature at higher radii and throughout the halo as seen in the temperature slices.

As a consequence, the $N_{\text{H I}}$ distribution shows a steep decrease at ≈ 20 kpc for the Low and Mid runs which becomes more gradual in the High run. The results from this run match well with the COS-Halos data, except for 2 systems which lie above the 99th percentile limits. The High run also shows a high covering fraction of Lyman Limit Systems (defined as systems with $N(HI) > 10^{17}$ cm^{-2}) out to ≈ 50 kpc of the virial radius. This is roughly consistent with the observations of Chen *et al.* (2018), who found a high covering fraction of such systems out to ≈ 150 kpc in a sample of luminous red galaxies, likely associated with massive halos with virial radii $2 - 3$ times larger than the ones considered here (e.g. Artale *et al.*, 2018; McEwen and Weinberg, 2018; Zehavi *et al.*, 2018). The $N_{\text{H I}}$ trend from the High run also matches high mass loading stellar feedback model in F17, as well as the observations of the extended CGM, described in Johnson *et al.* (2015).

Note that when looking at the projections of H I we can say that the sightlines that match the COS-Halos data after about 100 kpc are from the inflowing material in the positive x/y quadrant and not uniformly distributed around the halo. This may or may not be representative of all star-forming galaxy halos, as Lyman α emission has been observed at these impact parameters in $z \approx 2.5$ galaxies (Cantalupo *et al.*, 2014; Prescott *et al.*, 2015).

3.3.3 COS-Halos Comparisons

In Figure 3.5, we show the projected column density maps for several key ions, and in Figure 3.6 we plot the corresponding column density profiles, again showing the 50th percentile of sightlines vs. radial distance r in 10 kpc bins. In the top two rows of Figure 3.5, we focus on Si II and Si III, which sample low and intermediate ionization
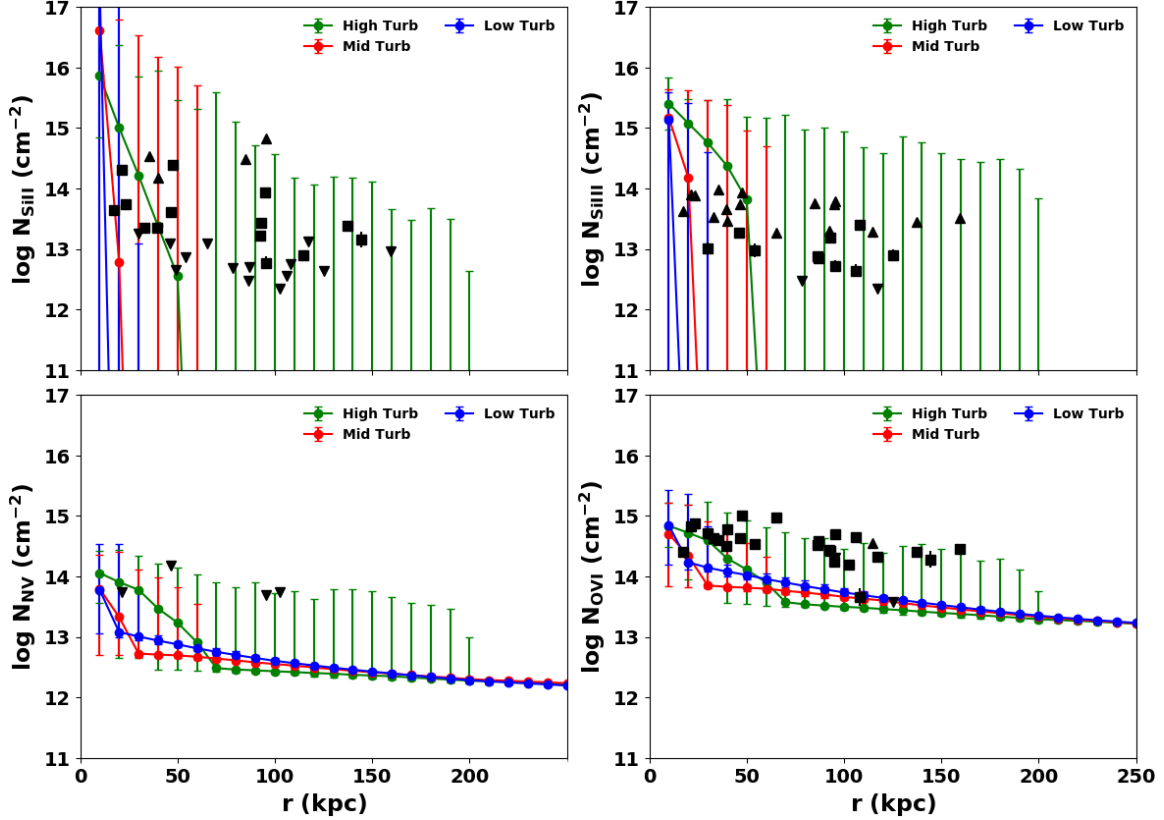
Figure 3.6: Filled circles show the 50th percentile of sightlines in 10 kpc bins for Log $N_{\text{Si II}}$ (top left), $N_{\text{Si III}}$ (top right), $N_{\text{N V}}$ (bottom left), and $N_{\text{O VI}}$ (bottom right) vs. radial distance r for the Low (blue), Mid (red), and High (green) runs at 3 Gyrs contained to cells within the virial radius. Error bars show the 1st percentile as the lower limit and 99th percentile as the upper limit. Projections were generated for each sightline as a line integral of the ion number density along the z-axis. We also show detections (black squares) and limits (black arrows) from the COS-Halos sample overlaid on our projected column densities.

state material commonly observed in the halos of low-redshift galaxies (Werk *et al.*, 2013; Borthakur *et al.*, 2016; Heckman *et al.*, 2017). In the bottom two rows, we show N V, which has an ionization potential just 40 eV below the 138 eV ionization potential of O VI, and is chosen due to its lack of absorption in the CGM of star-forming galaxies for reasons that remain to be determined (W16), and O VI, an ion known to trace the hotter ambient gas within the halo (Sembach *et al.*, 2003; Werk *et al.*, 2016; Tumlinson *et al.*, 2017).

This figure shows that $N_{\text{Si II}}$ is mostly concentrated in the center as this contains

moderately dense ($n \approx 10^{-3}$ cm^{-3}), cold ($T \approx 10^4$ K) clumps. The Low and Mid runs show this low ionization state material being tightly constrained to the inner 50 kpc, while the High run shows Si II extending out to near the virial radius of the halo, embedded within the large inflow of material.

The column density profiles for $N_{\mathrm{Si\ II}}$ at low impact parameter show agreement between all of the runs and the limits/detections from the COS-Halos sample. However, after about 20 kpc the Low and Mid runs show steep declines in their profiles, that do not agree with the observed detections (note COS-Halos limits and detections lie within the 99$^{\mathrm{th}}$ percentile upper limits of the Mid run up to ≈ 60 kpc). However, a more gradual decline in $N_{\mathrm{Si\ II}}$ upper limits is seen in the High run, which agrees well with the COS-Halos results.

The intermediate ionization state component, as traced by Si III, also shows a fairly different view across the varying levels of turbulence in the second row of the column density maps plotted in Figure 3.6. Si III follows a similar spatial distribution to Si II, but traces slightly hotter material surrounding the coldest gas. The $N_{\mathrm{Si\ III}}$ profiles also show a similar picture to $N_{\mathrm{Si\ II}}$ with an agreement between all of the runs and the COS-Halos sightlines, followed by a steep decline at about 20 kpc for the Low and Mid runs while the more steady decline in upper limits of the High run agrees well with the observed detections and limits.

In Figures 3.16, 3.17, and 3.19 in Appendix 3.6 we show projected column density maps for the other COS-Halos ions (C II, C III, Mg II, N II, O I, and Si IV, omitting the iron ions) as well as COS-Halos observations. These column density maps show similar trends as the ones above, and the radial trends in ionic columns from the High run again shows a good agreement with the COS-Halos data. The trends also match well with the recent $z \lesssim 1$ COS CGM Compendium survey described in Lehner *et al.* (2018), and other studies of the cool CGM around the nearby galaxies M31 in Lehner

et al. (2015) and NGC 1097 in Bowen *et al.* (2016). They also are in reasonable agreement with fully cosmological simulations such as the Evolution and Assembly of Galaxies and their Environments (EAGLE; Oppenheimer *et al.*, 2018), Feedback in Realistic Environments (FIRE; Ji *et al.*, 2019), and IllustrisTNG (Kauffmann *et al.*, 2019).

Next we look at N V and O VI as shown in the bottom 2 rows of Figure 3.6. The N V within the halo shows similarities with the O VI, however, it has a significantly lower abundance, a feature more evident in the column density profiles in Figure 3.5. $N_{\text{O VI}}$ limits/detections lie within the 1st to 99th percentile errorbars of the Low and Mid runs at for $r < 60$ kpc while limits/detections further out agree well with the High run. The O VI columns observed in the extended CGM study of Johnson *et al.* (2015) show gradually decreasing columns that lie within our 1st to 99th percentile errorbars. The radial decrease in abundance of both of these ions in Figure 3.6 and their distribution in Figure 3.5, lead us to theorize that sightlines in which O VI is observed without accompanying N V may primarily trace ambient halo gas, while sightlines that show both O VI and N V absorption might instead trace material in a shell around cooler inflowing gas.

We furthermore compare our O VI with other recent theoretical results, and again find very similar trends between the N_{OVI} profile from our High run and the high mass loading model in F17. The simulations done in that work used equilibrium heating and cooling rates from Wiersma *et al.* (2009) that include the effects of a EUVB, which are important at the low densities typical to the CGM. We also find our N_{OVI} profiles to be greater than those given from the chemical equilibrium cooling flow solutions of $11.5 < \log M_{\odot} < 12.5$ halos found in Stern *et al.* (2019), however, the authors state that this may be alleviated with some mechanism to heat the outer CGM or if O VI traces photoionized gas beyond an accretion shock. As we discuss
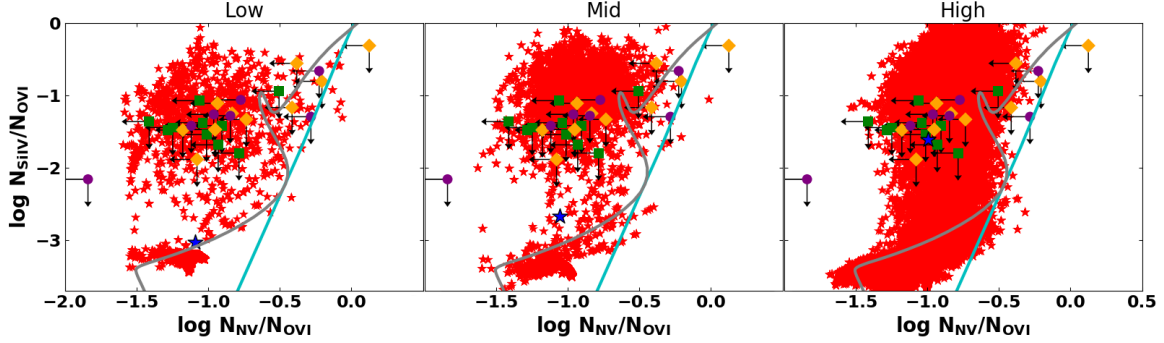
Figure 3.7: Log $N_{\text{Si IV}}/N_{\text{O VI}}$ vs. log $N_{\text{N V}}/N_{\text{O VI}}$ from the Low (left), Mid (middle), and High (right) runs are shown as red stars with the averages shown as blue stars. These are overlaid by the matched Si IV, N V, and O VI components from W16 Figure 12. Green circles represent the "broad" type O VI absorption, orange circles are "narrow" type absorbers, and purple circles are "no-low" type absorbers. As a reference, we plot a single-zone Cloudy model photoionized by an HM2012 EUVB (solid cyan) with $-4 < \log U < -1$ along with an Orly & Gnat time-dependent radiatively cooling isochoric solar metallicity model in gray.
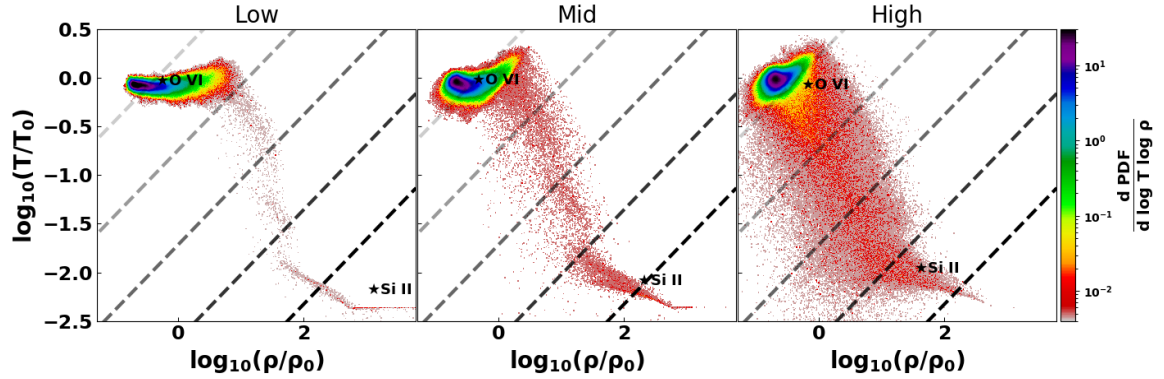
Figure 3.8: Log T/T_0 vs. log ρ/ρ_0 probability density maps from the Low (left), Mid (middle), and High (right) runs where $T_0 = 1.2 \times 10^6$ K and $\rho_0 = 2.1 \times 10^{-28}$ g cm^{-3} are at $t = 0$. The maps omit data within $r = 12$ kpc and are overlaid with the O VI and Si II weighted temperatures/densities as black stars in addition to dashed lines indicating lower (higher) entropy as darker (lighter) lines. The lines of constant entropy are as follows : 0.1, 0.6, 3.1, 17.2, and 95.5 KeV cm^{-2}.

in section 3.3.1, the gas in our simulations is shock heated throughout the first phase of its evolution and thus the ambient O VI primarily traces post-shock, photoheated gas, while higher abundances of this ion surrounding cooling flows may primarily be radiatively cooling gas.

We also compare our results to the $N_{\rm Si\ IV}/N_{\rm O\ VI}$ and $N_{\rm N\ V}/N_{\rm O\ VI}$ ratios observed in Werk *et al.* (2016) in Figure 3.7 where we only show sightlines with log $N_{\rm O\ VI} >$ 13.5 to limit our sample to similar sightlines as the COS-Halos sample in W16. Furthermore, we show a single-zone Cloudy model photoionized by an HM2012 EUVB model in cyan and a Gnat and Sternberg (2007) isochoric solar metallicity model overlaid in grey.

The Cloudy models have the largest values of $N_{\rm N\ V}/N_{\rm O\ VI}$ and are the most discrepant with the observations, indicating that the large observed differences between N V and O VI can not be explained by equilibrium models. Furthermore, Buie *et al.* (2020a) showed that such equilibrium models tend to underpredict the amount of O VI which may explain the high $N_{\rm N\ V}/N_{\rm O\ VI}$ values produced. The non-equilibrium isochoric cooling models from Gnat and Sternberg (2007) lie closer to the data, but still have $N_{\rm N\ V}/N_{\rm O\ VI}$ values larger than most of the observations, suggesting that radiative cooling alone is insufficient to explain these results.

Finally, the MAIHEM results, which include not only radiative cooling but cooling by the mixing between cold and hot material, have a shape that is similar to the Gnat and Sternberg (2007) results, but shifted further to the left, covering the observed range of $N_{\rm N\ V}/N_{\rm O\ VI}$ ratios. This suppressed ratio arises from gas that cools even faster than isochorically, due the combination of radiative cooling and the turbulent mixing of hot and cold media. This ratio is similar for all three runs with the log of the ratios being -1.0, -1.05, and -1.09 for the Low, Mid, and High runs respectively.

The similar dispersion in our model ratios suggests that while strong turbulence is

needed to set up a large-scale convective flow in the halo, leading to cold gas at large radii, it is not essential to reproducing the $N_{\rm N\ V}/N_{\rm O\ VI}$ results. Rather it is a feature that is common to all of our runs: the rapid cooling of gas through simultaneous mixing and radiation, which results in the extreme non-equilibrium ratios observed in nature. Note also that this ratio is not a result of the log $N_{\rm O\ VI} > 13.5$ column density limit imposed by the observations. If we relax this limit we simply see a greater amount of sightlines that agree with the observed $N_{\rm N\ V}/N_{\rm O\ VI}$ values.

Our average $N_{\rm N\ V}/N_{\rm O\ VI}$ is also consistent with ratios from recent re-observations of two CGM systems in Lochhaas *et al.* (2019) and some of the upper limits implied by these observations, however, we do not have any sightlines that fall below log $N_{\rm N\ V}/N_{\rm O\ VI}$=-1.8, implying some other physics may be necessary to fully capture the dynamic CGM, such as thermal conduction and/or magnetic fields. Liang and Remming (2020) showed in their simulations of cold clouds in a hot medium that these considerations increase the efficiency of heat transfer from cooling gas while a weak magnetic field acts to shield developing cold clouds. This would reduce the lifetime of intermediate ions tracing gas transitioning between high and low ionization states while maintaining small clumps of the low ionization state material.

Finally, the average $N_{\rm Si\ IV}/N_{\rm O\ VI}$ values in the MAIHEM models, increase with greater turbulence. This is a result of the increased amount of colder gas in the CGM of the more turbulent, runs which encompasses larger amounts of Si IV. When only considering gas with $n \leq 10^{-4}$ cm^{-3}, the resulting log $N_{\rm Si\ IV}/N_{\rm O\ VI}$ values are $\lesssim$ -0.5.

Finally, we plot the 2D, volume-weighted probability density distribution for our runs in Figure 3.8, which indicates the phase distribution of the media. Here we observe that most of the volume lies at a value slightly lower density than the average at $t = 0$ Gyr and virial temperature of the halo. Increasing turbulence not only disperse a greater number of cells across lower temperatures and densities but also
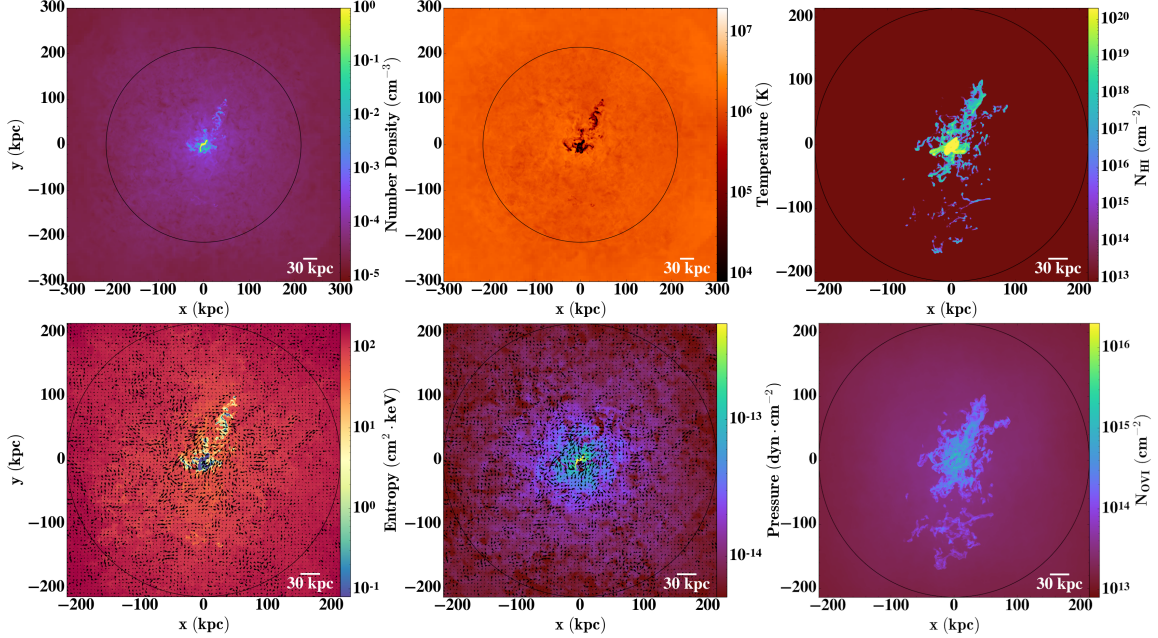
Figure 3.9: Panels showing the number density slice (top left), temperature slice (top middle), projected H I (top right), entropy slice (bottom left), pressure slice (bottom middle), and projected O VI (bottom right) at 3 Gyrs along the z-axis for the double-resolution High run. The arrows show the $x - y$ velocity vectors of the flow and a black circle shows the virial radius at $R_{\mathrm{vir}} \approx 220$ kpc.

promote a trend where the majority of cells go towards a constant entropy, as expected for a convective flow. Finally, increasing turbulence also pushes the Si II weighted temperature/density towards less dense and hotter gas while the O VI weighted temperature/density varies little between the runs.

3.3.4 Convergence Tests

Finally, as a test of convergence, we repeated the High run with double the resolution to see how this affects the results and evolution of the simulation. Specifically, the driving scale and strength of the turbulence were taken to be the same as the High run described above, but the levels of refinement were as follows: for R $\gtrsim$ 300 kpc the domain was at a resolution of 128^3 which translates to 6.2 kpc, for $300 \gtrsim$ R $\gtrsim$ 250 kpc the resolution was 256^3 which translates to 3.1 kpc, $250 \gtrsim$ R $\gtrsim$ 225 kpc the
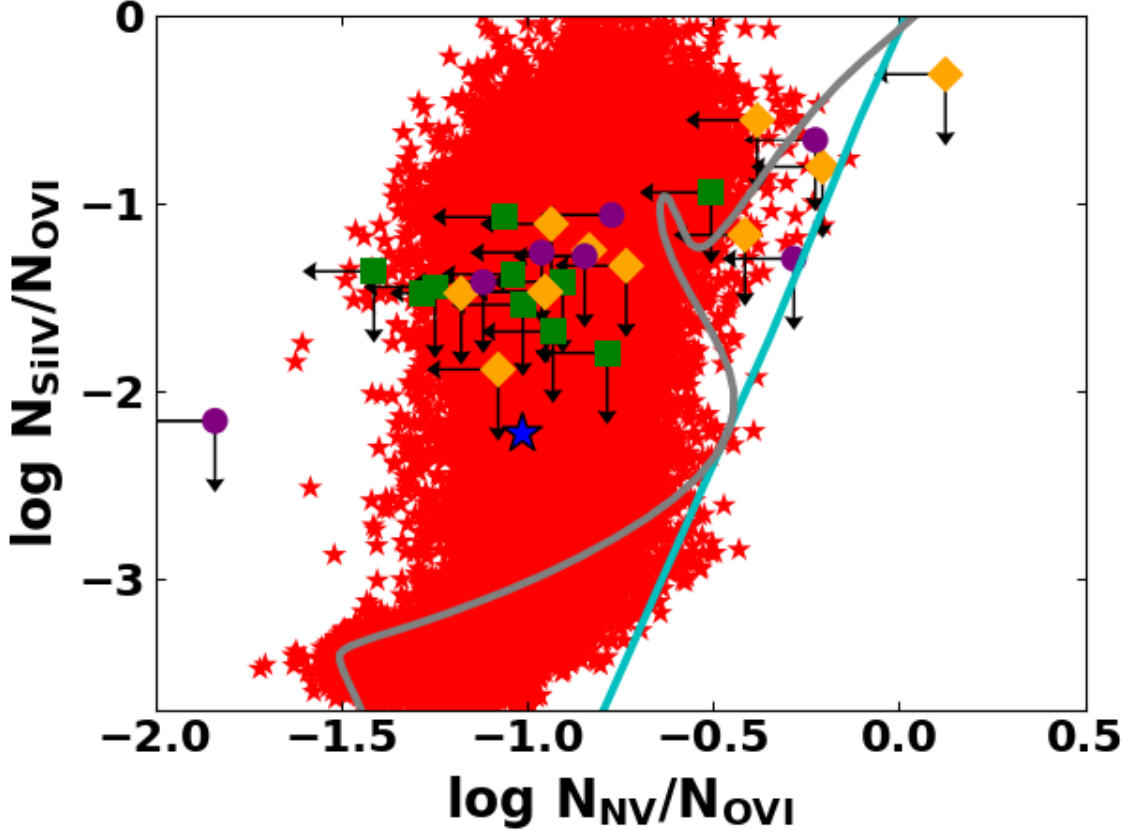
Figure 3.10: Log $N_{\text{Si IV}}/N_{\text{O VI}}$ vs. log $N_{\text{N V}}/N_{\text{O VI}}$ from the double-resolution High run shown as red stars with the average shown as a blue star. These are overlaid by the matched Si IV, N V, and O VI components from W16 Figure 12. Green circles represent the "broad" type O VI absorption, orange circles are "narrow" type absorbers, and purple circles are "no-low" type absorbers. As a reference, we plot a single-zone Cloudy model photoionized by an HM2012 EUVB (solid cyan) with $-4 < \log U < -1$ along with an Orly & Gnat time-dependent radiatively cooling isochoric solar metallicity model in gray.

resolution was 512^3 which translates to 1.6 kpc, and for 225 kpc $\gtrsim$ R the resolution was 1024^3 which translates to 0.8 kpc.

This run evolves similarly to the previous runs, with gas within a 30 kpc radius cooling rapidly for the first 100 Myrs followed by an outward moving accretion shock at 1 Gyr. The average 1D velocity dispersion of this run was 40 km s^{-1}, extremely similar to the 41 km s^{-1} we found in the lower resolution case with the same driving.

However, due to the increased resolution, there is more cooling in the initial stages,
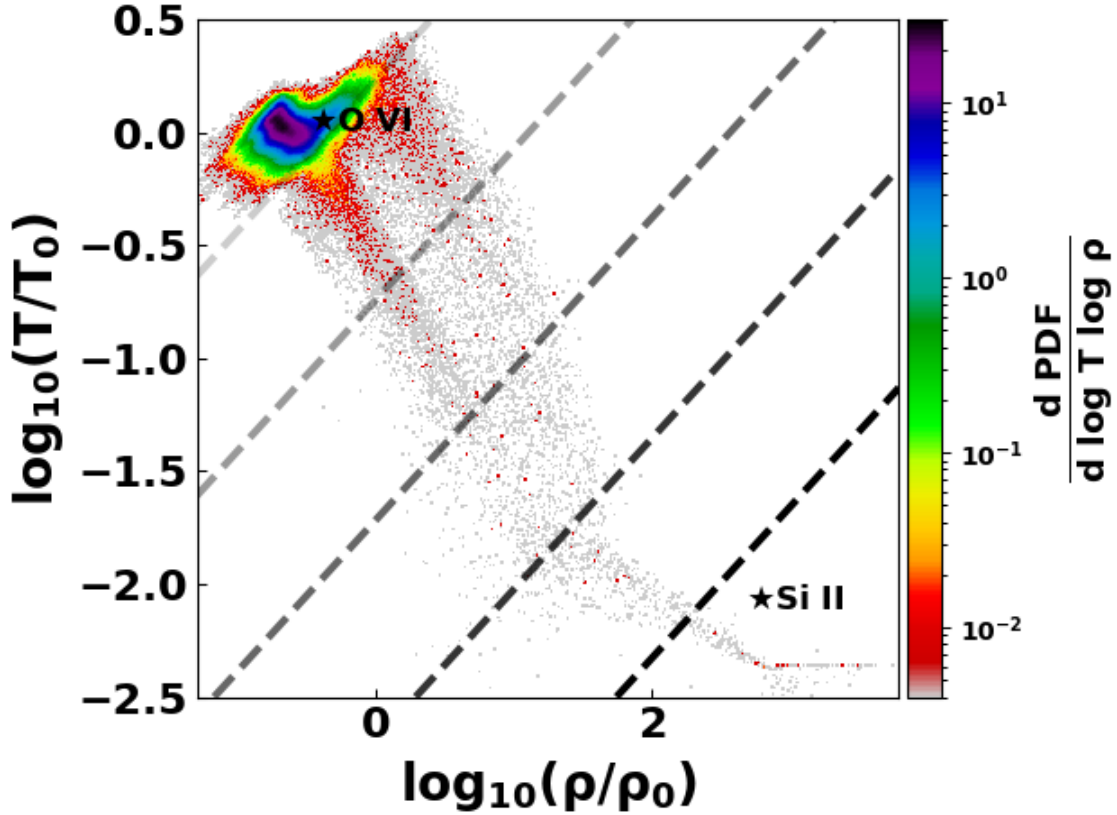
Figure 3.11: Log T/T_0 vs. log ρ/ρ_0 probability density maps from the double-resolution High run where $T_0 = 1.2 \times 10^6$ K and $\rho_0 = 2.1 \times 10^{-28}$ g cm^{-3} are at $t = 0$. The maps omit data within $r = 12$ kpc and are overlaid with the O VI and Si II weighted temperatures/densities as black stars in addition to dashed lines indicating lower (higher) entropy as darker (lighter) lines. The lines of constant entropy are as follows : 0.1, 0.6, 3.1, 17.2, and 95.5 KeV cm^{-2}.

which eventually settles to similar cooling rates as compared to its original resolution counterpart. A consequence of the increased cooling during the initial stages is that more material is able to collapse towards the center through the accretion shock. This results in the density and temperature profiles shown in Figure 3.9, along with pressure and entropy profiles that are similar to a mix between the Mid and High runs. In this double-resolution case we still see the formation of accretion flows similar to those found in the original High run that feeds gas from the hot ambient halo through low pressure/entropy filaments. The higher resolution also allows for

smaller H I clouds to exist further out in the CGM in addition to filaments.

The increased resolution leads to the formation of smaller structures as compared to the larger filamentary inflows observed in its original resolution counterpart, as visible in the column density maps of H I and O VI shown in Figure 3.9, as well as a wide range of ions as shown in Figure 3.18 in the appendix.

Looking at the column density profiles for all our runs in Figure 3.19 in the appendix, we find that the 50th percentiles from this run typically decrease faster than its original resolution counterpart, owing to its more centrally concentrated density profile which is a result of the larger amounts of cooling in the initial stages. The COS-Halos limits and detections remain in agreement with the errorbars of the column density profiles, however, they show smaller columns $\gtrsim$ 100 kpc compared to those from the original resolution run due to the more resolved cooling. Higher feedback in the center, which could take the form of higher velocity dispersion, a more negative α in Equation 4.2, or rotation in the center would likely reduce the amount of gas cooling towards the center while maintaining smaller structures that can cool out of the ambient medium as opposed to the filaments of gas in the original resolution simulation.

When these column densities are converted into ratios, we see a very similar trend in $N_{\text{Si IV}}/N_{\text{O VI}}$ vs. $N_{\text{N V}}/N_{\text{O VI}}$ as shown in Figure 3.10 as compared to the original resolution run. Like the original High run, the increased resolution run produces many sightlines with ratios that agree with limits found in W16, as well as many that trace higher density gas, which lies above the $N_{\text{Si IV}}/N_{\text{O VI}}$ upper limits.

Finally, in Figure 3.11 we show the 2D probability distribution for the double-resolution High run. Here we see that the core of the distribution is extended along the direction of constant entropy, pointing to a large scale convective flow similar to that in the original resolution High run. However, the higher resolution results in a

double-peaked tail towards lower temperatures/densities that is similar to the Low turbulent run.

3.4   Constraints on CGM Turbulent Motions

3.4.1   Observational Constraints on CGM Turbulence

While the levels of turbulence incorporated in our High run provide a good match to multiphase measurements of ions in the low redshift CGM, they are also somewhat larger than those inferred from Doppler b parameters in individual low ionization state absorbers. Recently, Zahedy *et al.* (2019) compared the Doppler parameters of Mg II and H I absorbers within the inner CGM of massive elliptical galaxies at $z \approx 0.4$. Using ratios of the b values of these ions, they found that the gas associated with low ionization state gas has a mean temperature of 2×10^4K and a modest non-thermal broadening of ≈ 7 km s^{-1}. On the other hand, W16 and Zahedy *et al.* (2019) found fairly broad $(b > 40$ km s$^{-1})$ O VI absorption in the CGM of star-forming galaxies with an average non-thermal contribution of $\approx$ 40-50 km s^{-1} although possible blending of narrow components with velocity offsets remains an issue for these measurements, due to the moderate resolution of the COS spectrograph.

At $z = 2$, the KBSS used High-Resolution Echelle Spectrometer (HIRES) measurements of 130 metal-bearing absorbers to determine the b parameters in the CGM of $\approx L^*$ galaxies. They found that O VI and C IV absorbing gas resulted from somewhat hotter gas than low-redshift Mg II, but the non-thermal width of this material was ≈ 6 km s^{-1} (Rudie *et al.*, 2019).

It is important to keep in mind, however, that these measurements constrain the turbulent velocities associated with single absorbers, which due to the turbulent cascade, are smaller than the velocities at the driving scale by a factor of
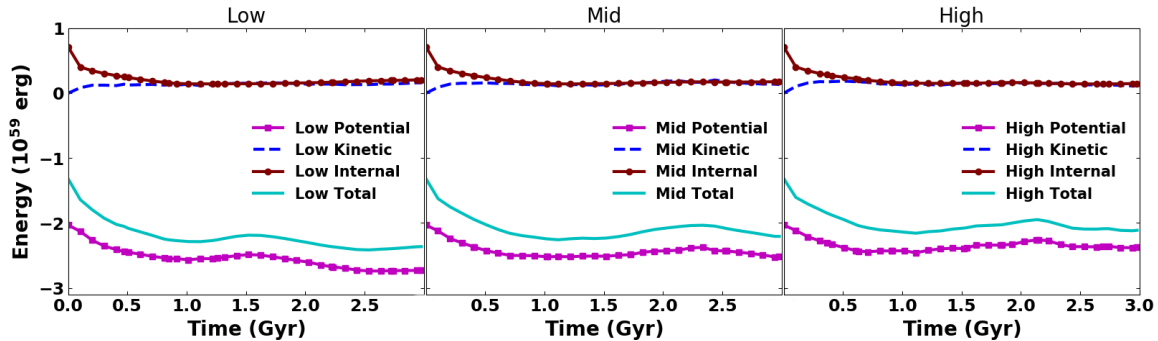
Figure 3.12: Energy vs. time in potential (magenta squares), kinetic (blue dashed), internal (maroon circles), and total (solid cyan) for the Low (left), Mid (middle), and High (right) runs. The energy is shown in units of 10^{59} erg.

$(L_{\text{absorber}}/L_{\text{drive}})^{\alpha}$ where alpha is $1/3$ to $1/2$ depending on the Mach number of the medium Kritsuk *et al.* (2007); Pan and Scannapieco (2010). The sizes of single cold absorbers in our simulations are near the resolution limit of ($L_{\text{absorber}} \approx 2$ kpc). This means that the expected observed b parameters of cold ions in the high run should be about 10 km s^{-1}, consistent with the observations of $\approx 10^{12}$ M$_{\odot}$ halos.

The overall level of turbulence is somewhat better constrained in galaxy clusters and groups, where line emission in the intracluster medium allows for measurements at physical scales at or above the driving scale. Such measurements have been carried out directly in the Perseus Cluster of galaxies by the Hitomi satellite, which found $160 - 200$ km s^{-1} motions in the central regions, corresponding to an energy density in turbulent motions of $\approx 4\%$ or a Mach number of ≈ 0.25 (Hitomi Collaboration *et al.*, 2016, 2018). These values can also be compared to those in a much larger range of objects, as measured by a variety of indirect techniques, including resonant scattering, X-ray surface brightness fluctuation analysis, and measurements of the kinematic Sunyaev-Zeldovich effect (Simionescu *et al.*, 2019).

The resonant scattering approach relies on the fact that several of the brightest X-ray emission lines are moderately optically thick, causing them to be suppressed at a level that is highly dependent on turbulent broadening (Gilfanov *et al.*, 1987;

Churazov *et al.*, 2004). In clusters, this has led to controversial results (Kaastra *et al.*, 1999; Mathews *et al.*, 2001; Sanders and Fabian, 2006), due to complications in interpreting the He-like Fe line at 6.7 keV because of variations of gas temperature and metallicity (Zhuravleva *et al.*, 2013). On the other hand, the results have been clearer around massive elliptical galaxies, in which suppression of the Ne-like Fe line at 15.01 Å was detected (Xu *et al.*, 2002; Werner *et al.*, 2009). Most recently, Ogorzalek *et al.* (2017) obtained velocity constraints for 13 such massive galaxies, determining an averaged 1D Mach number of 0.25, corresponding to a non-thermal energy fraction of $\approx 10\%$.

A second approach is to relate the observations of X-ray surface brightness and gas density fluctuations to the velocity fluctuations in the underlying medium (Gaspari and Churazov, 2013). In this way, Hofmann *et al.* (2016) analyzed deep Chandra observations of 33 well-known clusters, arguing that the observed fluctuations correspond to a sample averaged 1D Mach number of 0.16. Similarly Zhuravleva *et al.* (2018) conducted a statistical analysis of X-ray surface brightness and gas density fluctuations in the cool cores of 10 nearby clusters concluding the non-thermal energy was $\approx 5\%$ of the thermal energy in the inner half-cool-core regions and up to 12% in the outer core regions.

In massive clusters, a third method of estimating the integrated contribution of the non-thermal pressure relies on the fact that measurements of the total baryon fraction of massive clusters are largely insensitive to uncertainties in baryonic physics such as cooling, star formation, and feedback (e.g. White *et al.*, 1993; Kravtsov *et al.*, 2005; Planelles *et al.*, 2013; Sembolini *et al.*, 2016b,a). In this way Eckert *et al.* (2019) used high-precision hydrostatic masses out to the virial radius for a sample of 13 nearby $3 \times 10^{14}!M_\odot < M_{500} < 1.2 \times 10^{15}$ $M_\odot$ clusters, and found a median non-thermal pressure fraction of 6% and 10% at R_{500} and R_{200}, respectively.

Figure 3.13: Energy rates vs. time in cooling (red squares), $\Delta E_{\text{tot}}/\Delta t$ (cyan circles), and ϵ_{turb} (black diamonds) for the Low (left), Mid (middle), and High (right) runs. A grey dashed line indicates no change in energy. The energy rates are shown in units of 10^{50} erg yr^{-1}.

All of these three approaches give a fraction of non-thermal pressure consistent with subsonic turbulence with a Mach number ≈ 0.25, matching that of the High run as shown in Figure 3.1. Thus measurements at or above the driving scale in $\gtrsim 10^{13}$ M$_\odot$ systems and extrapolations down to the scale of individual absorbers in $\approx 10^{12}$ M$_\odot$ systems are both completely consistent with the turbulent velocities assumed in our High simulation.

3.4.2 Energy Requirements for CGM Turbulence

Having shown the ionization state structure and turbulent velocities assumed in our simulations are both consistent with observations, we now investigate the amount of energy needed to sustain these motions. We find the gravitational potential (PE), kinetic (KE), internal (EI), and total energies (PE+KE+EI) within the virial radius for each run and show these in Figure 3.12. We define these energies as the following:

$$PE \equiv -4\pi G \rho_0 R_s^3 \int dV \frac{\rho(r)}{r} \ln\left(1 + \frac{r}{R_{\text{s}}}\right), \tag{3.4}$$

$$KE \equiv \int dV \frac{1}{2}\rho(\mathbf{x})v(\mathbf{x})^2, \tag{3.5}$$

$$EI \equiv \int dV \rho(\mathbf{x})T(\mathbf{x})\frac{N_A k}{[1 - \gamma(\mathbf{x})]\,\overline{A}(\mathbf{x})}, \tag{3.6}$$

62

with $\overline{A} \equiv \left(\sum_i X_i A_i^{-1} \right)^{-1}$, ρ and v are the density and velocity, X_i and A_i are the mass fraction and atomic mass of the ith species, N_A is Avogadro's number, k is the Boltzmann constant, γ is the weighted average adiabatic index, r defines the distance from the center, $\mathbf{x}$ defines the position in space, and the integrals are taken over the full volume within the virial radius.

Given the nature of our turbulence and how it is driven, it is non-trivial to back out the energy injection rate. As turbulence is driven, the energy from it is dissipated in the form of cooling as well as doing work by moving mass within the gravitational potential of the halo. Thus we find the cooling rate and rate of change in total energy, $\Delta E_{\text{tot}}/\Delta t$, the sum of which gives us the turbulent energy injection rate, ϵ_{turb}. We show the cooling rate, rate of total energy change ($\Delta E_{\text{tot}}/\Delta t$), and the sum of these quantities, ϵ_{turb}, as a function of time in Figure 3.13. We also show these quantities for the double-resolution High run in Figure 3.14. Furthermore we provide the average cooling, $\Delta E_{\text{tot}}/\Delta t$, and ϵ_{turb} over 2 time periods in Table 3.1. The first 3 rows show these rates averaged over the full simulation time while the bottom three shows the rates from 1–3 Gyrs.

There is a minimum ϵ_{turb} below which the halo will collapse without viable pressure support and alternatively a maximum ϵ_{turb} which will cause the halo to explode. Between these lies a range of energies that will allow the halo to reach a steady-state after some time which is why we show the rates constrained to 1–3 Gyrs and quote 4×10^{49} erg yr^{-1}, in the High run, as the amount of turbulent energy we inject per year needed to produce a similar structure and ionization state ratios as nearby star-forming galaxy halos.

For comparison, we also show ϵ_{turb} in SN yr^{-1} (found by dividing by 10^{51} erg) in the last column of Table 3.1 and see that the High run, in particular, requires below 5% the kinetic energy released in a typical supernova event per year to sustain
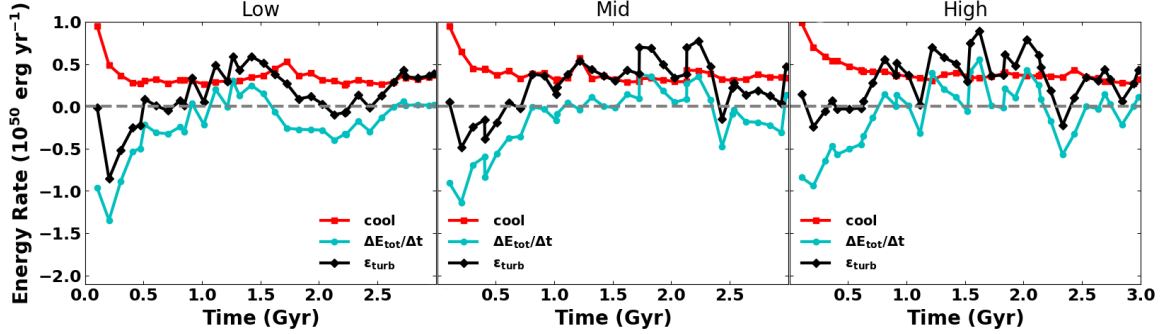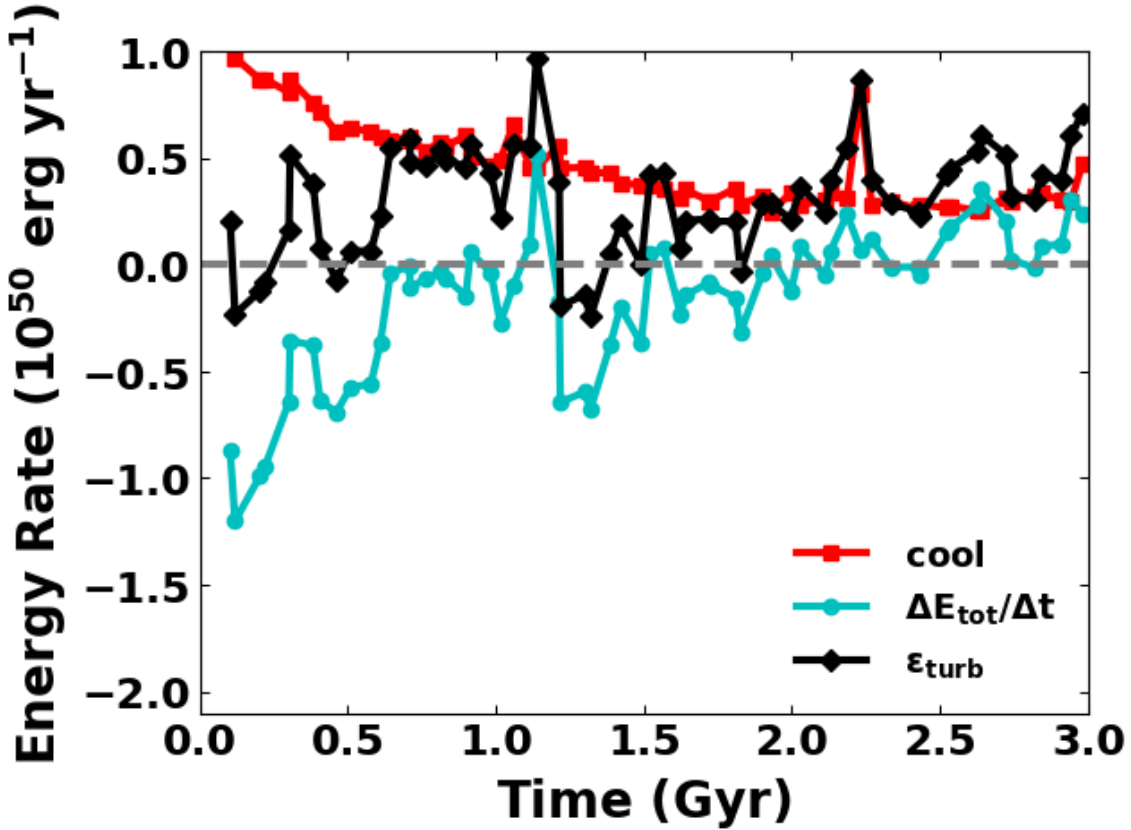
Figure 3.14: Energy rates vs. time in cooling (red squares), $\Delta E_{\text{tot}}/\Delta t$ (cyan circles), and ϵ_{turb} (black diamonds) for the double-resolution High run. A grey dashed line indicates no change in energy. The energy rates are shown in units of 10^{50} erg yr^{-1}.

Run	Cooling Rate	$\Delta E_{\text{tot}}/\Delta t$	ϵ_{turb}	Avg ϵ_{turb}^*
	(10^{49} erg/yr)	(10^{49} erg/yr)	(10^{49} erg/yr)	(SN/yr)
Low (t = 0–3 Gyrs)	3.448	-2.136	1.312	0.013
Mid (t = 0–3 Gyrs)	3.835	-1.436	2.399	0.024
High (t = 0–3 Gyrs)	4.035	-0.883	3.153	0.032
Low (t = 1–3 Gyrs)	3.317	-0.728	2.590	0.026
Mid (t = 1–3 Gyrs)	3.451	0.263	3.713	0.037
High (t = 1–3 Gyrs)	3.475	0.559	4.034	0.040

Table 3.1: Average cooling, energy change ($\Delta E_{\text{tot}}/\Delta t$), and turbulent energy injection rate (ϵ_{turb}) for various times throughout the simulations. * shown for comparison to supernova rates with typical energy input of 10^{51} ergs.

a 10^{12} M$_\odot$ galaxy halo with many features that share similarities to the COS-Halos observations.

We also convert our ϵ_{turb} in SN yr^{-1} to a star formation rate (SFR) by finding the number of stars that are massive enough to explode in a supernova, i.e. stars with masses between 8 M$_\odot$ and 100 M$_\odot$ and multiplying by the average star mass between 0.1–100 M$_\odot$. Assuming a Salpeter (1955) initial mass function, we find that about 0.3% of stars will experience a supernova with an average star mass of 0.4 M$_\odot$ for the aforementioned stellar mass range, obtaining a SFR of 4.8 M$_\odot$ yr^{-1} to supply the ϵ_{turb} found in the High run. This is comparable with the recent SFRs from the COS-Halos star-forming sample at 0.4–12 M$_\odot$ yr^{-1} (Werk *et al.*, 2013), the Milky Way at 1.65 M$_\odot$ yr^{-1} (Licquia and Newman, 2015), and 0.3–10 M$_\odot$ yr^{-1} from the Muse Gas Flow and Wind survey of z $\approx$ 1 star-forming galaxies (Schroetter *et al.*, 2019). We would like to remind the reader that we inject this energy inhomogeneously following Equation 4.2, and that this radial trend results in the shallow entropy profile in the High run, which allows convective motions to occur such that the gas cools while it falls towards the center.

Besides stars, turbulence can also be powered by accretion. If we consider ϵ_{turb} to be fueled purely by accretion onto the dark matter halo from the IGM moving at the escape velocity of the halo, this would require an average gas mass accretion rate of 50 M$_\odot$ yr^{-1} onto the galactic halo from the IGM.

For comparison we compute the actual mass inflow rate within the CGM of the High run by integrating the density times the radial velocity over a shell between 12-214 kpc. In this case, we find a mass inflow rate of $\dot{M} = 29$ M$_\odot$ yr^{-1} at 3 Gyrs (24 M$_\odot$ yr^{-1} for the double-resolution High run) which is similar to the solution for gas between 10-200 kpc Stern *et al.* (2019). This is also close to other theoretical work which give a gas accretion rate of $\approx 10 - 20$ M$_\odot$ yr^{-1} for 10^{12} M$_\odot$ halos at $z = 1$ to
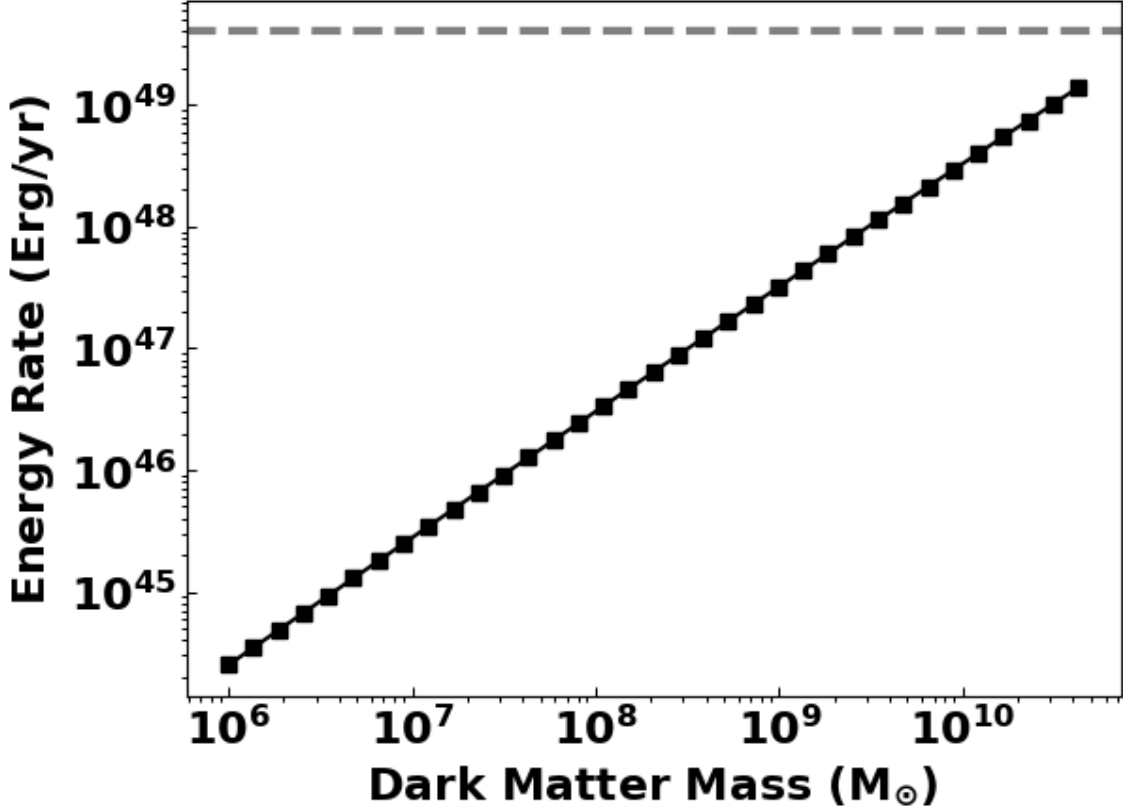
Figure 3.15: Total Energy loss rate vs. dark matter subhalo mass with ϵ_{turb} shown as a grey dashed line.

2 (e.g. van de Voort *et al.*, 2011). If we change the limits of integration to 12-14 kpc, to study the inter halo, we obtain a mass inflow rate of 4 $M_\odot$ yr^{-1}. Interestingly, the mass inflow rate found in the Stern *et al.* (2019) model that produced a good match to the higher O ions was $\dot{M} = 1.65$ $M_\odot$ yr^{-1}, which is close to our results and also matches the SFR of the Milky Way.

Finally, we consider the energy loss rate that would result from the gravitational drag of dark matter subhalos moving through the ambient dark matter density of the galactic halo. To estimate this we convert the ambient baryonic density of 10^{-27} g cm^{-3} to an ambient dark matter density and assume subhalos are traveling at $V = 141$ km s^{-1}, the dispersion velocity of the galactic halo at the virial

radius. This being the subsonic case (the average sound speed at 3 Gyrs is $c_s = 160$ km s^{-1}), we approximate the energy loss rate as:

$$-\frac{dE}{dt} = \frac{(96\pi)^{1/2}G^2 M_{sh}^2 \rho_0 V^2}{c_s^2} \ln \Lambda, \tag{3.7}$$

where ρ_0 is the ambient gas density of the galactic halo, M_{sh} is the mass of the subhalo, V is its velocity, Λ is R_{vir}/r, and r is the radius of the dark matter subhalo (Chandrasekhar, 1943; Rephaeli and Salpeter, 1980). Combining this with the dark matter mass function from Springel $et\ al.$ (2008) gives the integrated energy loss rate from all subhalos below a given mass:

$$-N\frac{dE}{dt} = (1.85 \times 10^{45}\ g)^{0.9}\frac{\rho_0 G^2 M_{sh}^{1.1} v^2}{c_s^3} \ln \Lambda. \tag{3.8}$$

We consider subhalos with masses between 10^6–4.4×10^{10} M$_\odot$, the upper limit being the mass beyond which we have only fractions of a subhalo. We find r by assuming the subhalos have the same density as the central galactic dark matter density, 3.67×10^{-25} g cm^{-3}, as well as a spherical shape yielding radii ranging from $350 - 12{,}000$ pc. Finally, we show the energy loss rate from all subhalos at a given mass as a function of subhalo mass in Figure 3.15 and see that this can reach levels as high as about a third of the overall energy input rate needed.

In reality it is likely a mixture of supernovae, gas inflows, and dynamical friction from dark matter subhalos that work together to drive turbulence in galaxy scale halos. These in turn help to drive convective flows, which produce large scale cold filaments and clouds that are surrounded by layers of rapidly cooling gas, contained within a hot diffuse medium.

3.5   Discussion and Summary

Motivated by recent COS-Halos results, we have used our updated MAIHEM model to carry out a suite of chemodynamical simulations of turbulent media in a

Navarro-Frenk-White (NFW) gravitational potential that match the circumgalactic media of low redshift galaxies. In all runs, turbulence was driven on scales between 10 to 30 kpc, with stirring that was strongest toward the center and fell off gradually with radius. We looked at 3 cases for the average σ_{1D}: 20, 34, and 41 km s^{-1}, which we labeled as the Low, Mid, and High run, respectively.

All three turbulent runs maintain the halo equilibrium temperature throughout their 3 Gyrs runtimes. While the Low run shows a strong entropy gradient and limited inhomogeneities, the High run shows a flatter entropy profile that sets up convective motions throughout the halo. These motions in turn produce an inhomogeneous medium that contains low and intermediate ionization state material at large radii.

Comparing the projected column densities of a wide range of ions with those from the COS-Halos survey, we found that all three runs can reproduce the observations at low impact parameters, but only the High run has sightlines at large impact parameters that overlap with the COS-Halos detections and limits. We also find good agreement between our O VI columns and those from other recent theoretical and observational work. Furthermore, unlike equilibrium models, our simulations produce many sightlines with $n \leq 10^{-4}$ cm^{-3} that match the $N_{\text{Si IV}}/N_{\text{O VI}}$ and $N_{\text{N V}}/N_{\text{O VI}}$ limits observed in the COS-Halos data. The suppressed ratio arises from gas that cools even faster than isochorically, due to the combination of radiative cooling and the turbulent mixing of hot and cold media.

When comparing to more recent results from Lochhaas $et\ al.$ (2019), we find our $N_{\text{N V}}/N_{\text{O VI}}$ in agreement with some of the detections and limits, however, we find no sightlines that agree with their lowest upper limits on this ratio.

The turbulent energy injection rate in our High simulation, $\epsilon_{\text{turb}} \approx 4\times10^{49}$ erg yr^{-1}, is comparable to expectations from several energy generation mechanisms that may be present in the CGM of low redshift star-forming galaxies such as supernovae, mass

accretion, and stirring by dark matter subhalos. In particular ϵ_{turb} is consistent with supernovae arising from a star formation rate of ≈ 5 M$_\odot$ yr^{-1}, or a mass infall rate of 50 M$_\odot$ yr^{-1} onto the galactic halo. Dark matter subhalos, however, can contribute significantly but are unlikely to be able to supply this energy rate by themselves.

We acknowledge that low ions are typically observed with lower velocity dispersions than the higher ions (Tumlinson *et al.*, 2013; Churchill *et al.*, 2015; Werk *et al.*, 2016) and by design our simulations had a higher velocity dispersion near the center of the halo, where low ionization state ions reside. However, we also found that on the smallest scale of our simulations, the internal turbulence within individual low ionization absorbers is comparable to those found in the observations.

Lastly, we conducted a second High run with double the resolution of our other runs and found it to have features similar to a mix between the original Mid and High runs. In this case, the gas cools more efficiently towards the center for the beginning of the simulation, setting up a CGM that is slightly less dense and overall hotter than that of the original High run, but still subject to large-scale convection. This facilitates the production of smaller structures in place of filaments, but the results remain in agreement with observations of the outer CGM, and the ion ratios also overlap the observed $N_{\text{Si IV}}/N_{\text{O VI}}$ and $N_{\text{N V}}/N_{\text{O VI}}$ ratios. More resolved cooling alters the non-equilibrium chemistry at 3 Gyrs only slightly as compared to the original resolution High run, with all of the elements varying by $\lesssim 3\%$ except for Fe, which varies by $\approx 8\%$ as compared to the original resolution simulation.

Future work will include adding more ions to our chemistry network, varying the radial profile of the turbulence, and studying the impact of rotation and electron thermal conduction. This will help yield a more complete understanding of the kinematic structure of the multiphase medium around star-forming galaxies.

3.6 Column Density Maps & Profiles

In this section we show our projected column density maps for C II, C III, Mg II, N II, O I, and Si IV. We also show these projected column density maps for Si II, Si III, N V, O VI, C II, C III, Mg II, N II, O I, and Si IV from the double-resolution High run. In addition to this, we show the column density profiles for the aforementioned ions as well as the temperature and H I column density profiles with data from the double-resolution High run.
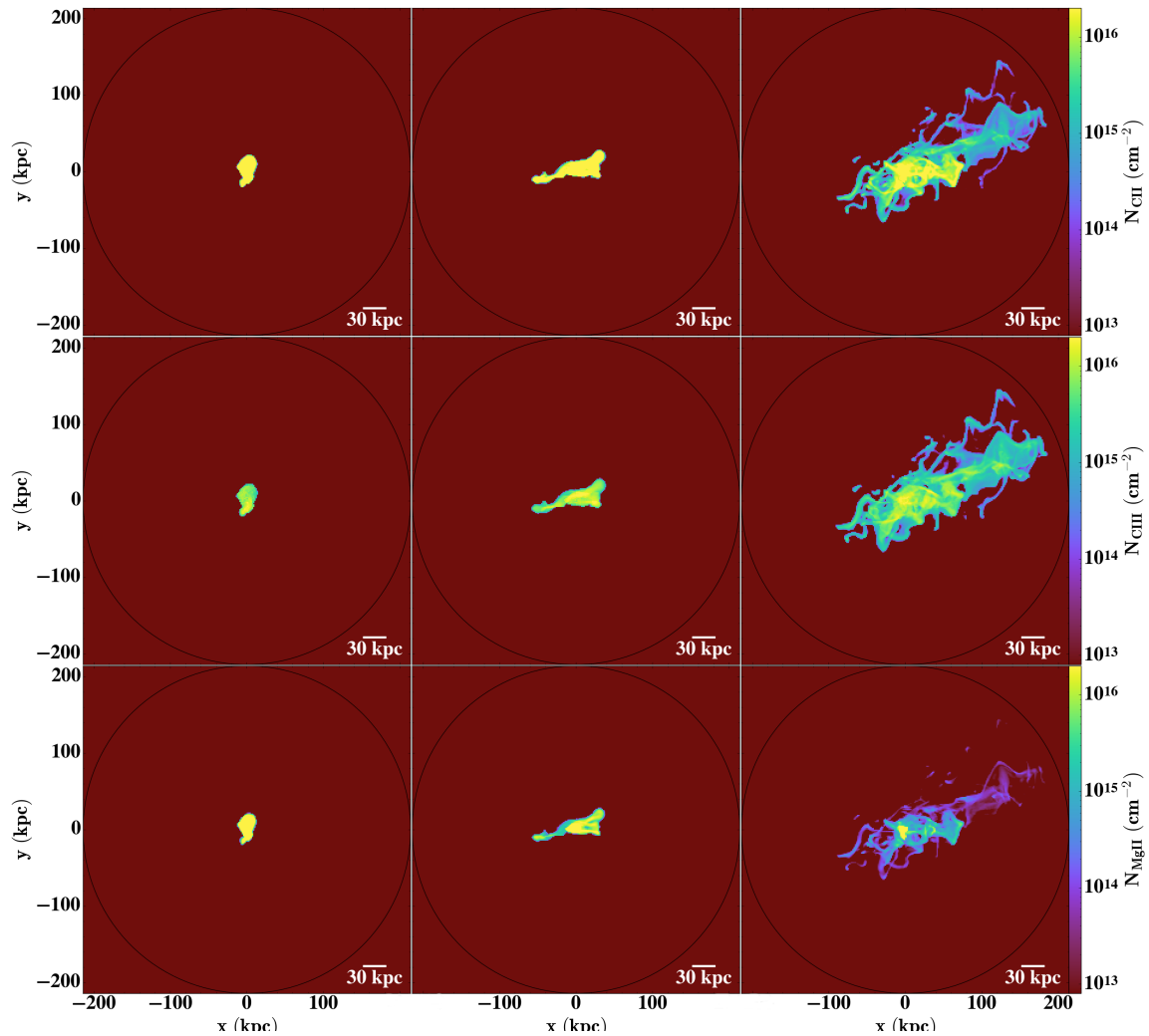
Figure 3.16: $N_{\text{C II}}$ (first row), $N_{\text{C III}}$ (second row), and $N_{\text{Mg II}}$ (third row) projections for the Low (left column), Mid (middle column), and High (right column) runs at 3 Gyrs. A black ring shows the virial radius at $r \approx 220$ kpc.
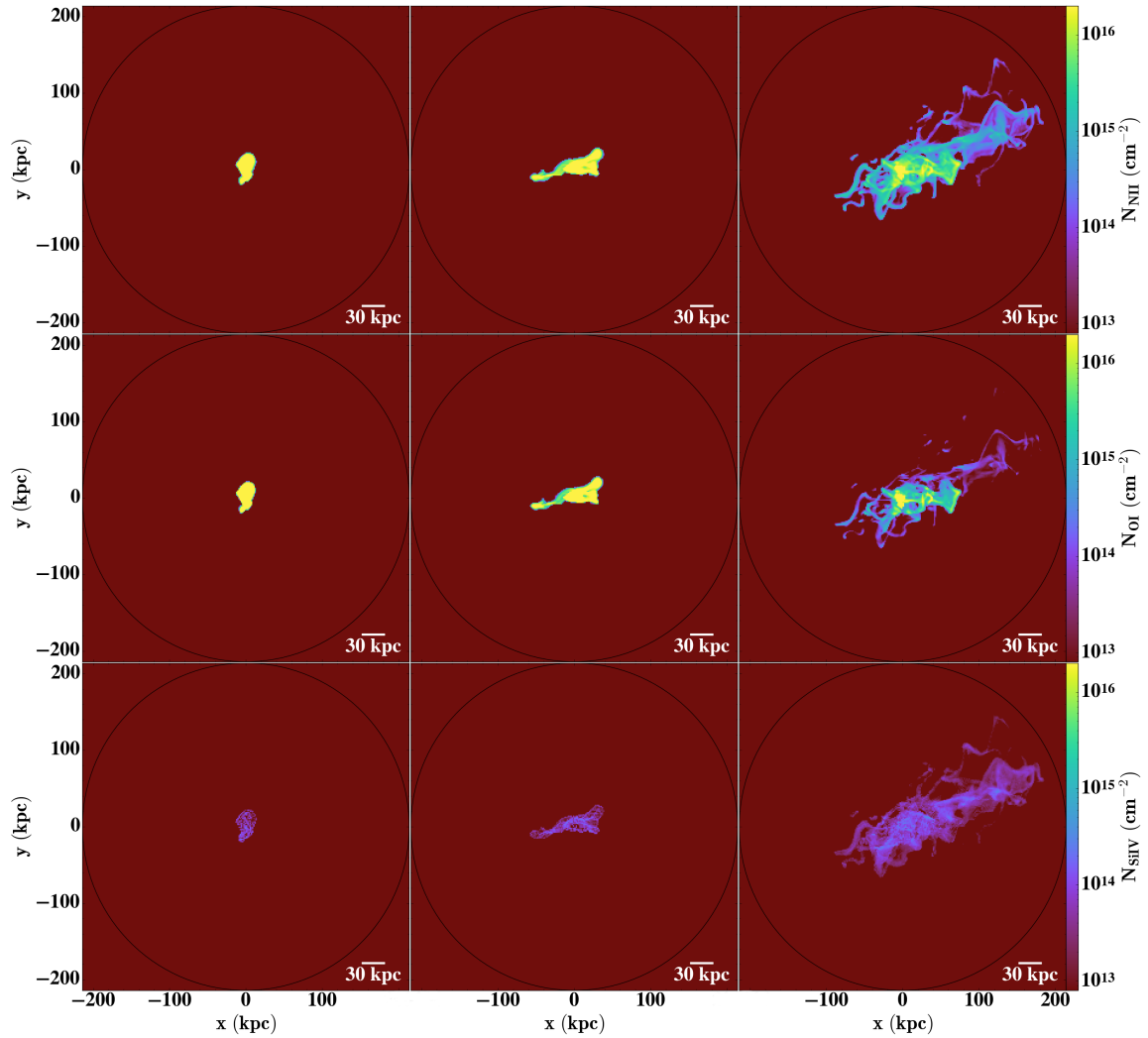
Figure 3.17: $N_{\text{N II}}$ (first row), $N_{\text{O I}}$ (second row), and $N_{\text{Si IV}}$ (third row) projections for the Low (left column), Mid (middle column), and High (right column) runs at 3 Gyrs. A black ring shows the virial radius at $r \approx 220$ kpc.
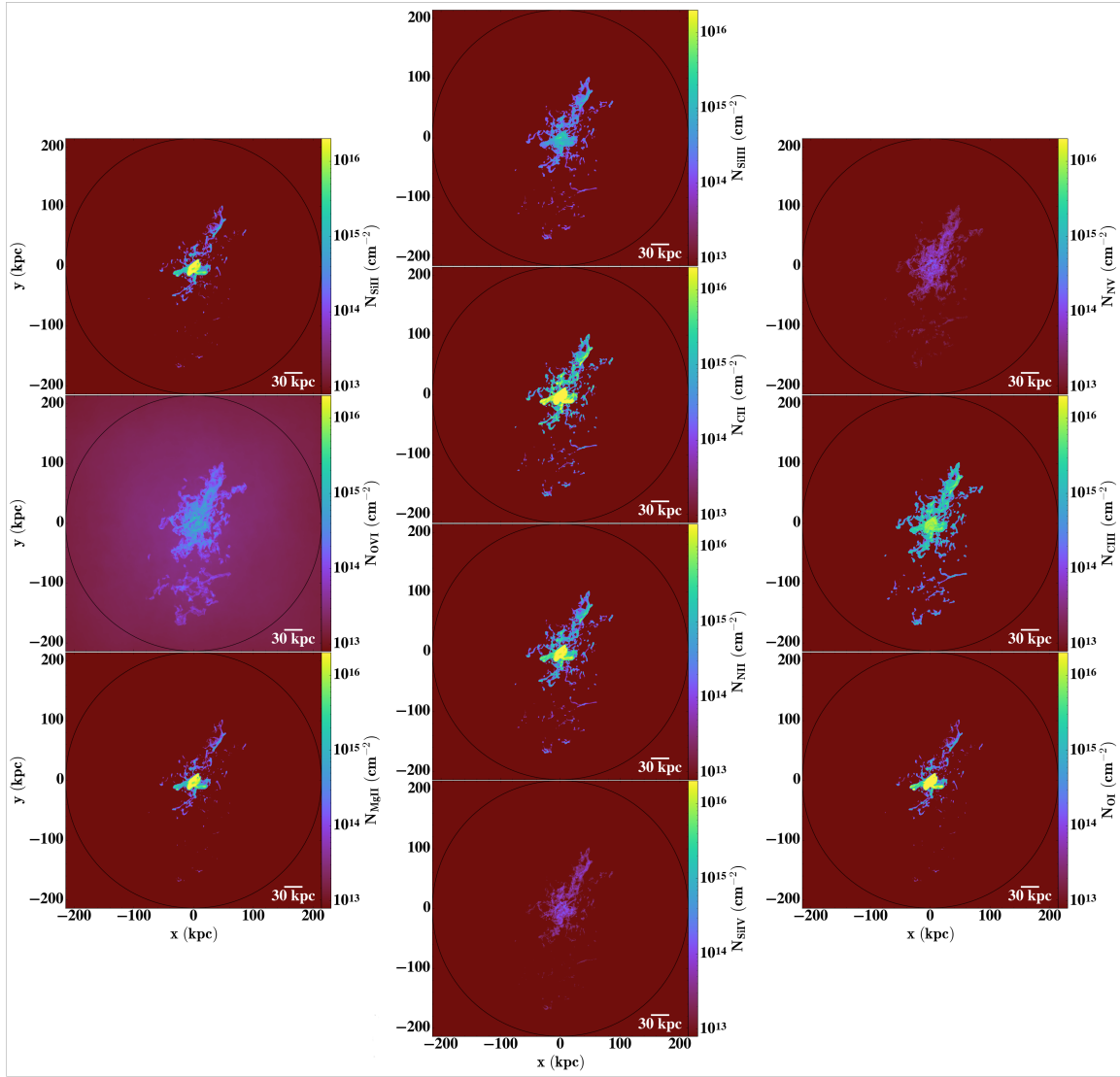
Figure 3.18: $N_{\text{Si II}}$ (top, first column), $N_{\text{Si III}}$ (top, second column), $N_{\text{N V}}$ (top, third column), $N_{\text{O VI}}$ (middle, first column), $N_{\text{C II}}$ (second, second column), $N_{\text{C III}}$ (middle, third column), $N_{\text{Mg II}}$ (bottom, first column), $N_{\text{N II}}$ (third, second column), $N_{\text{O I}}$ (bottom, third column), and $N_{\text{Si IV}}$ (bottom, second column) projections for the double-resolution High run at 3 Gyrs. A black ring shows the virial radius at $r \approx 220$ kpc.
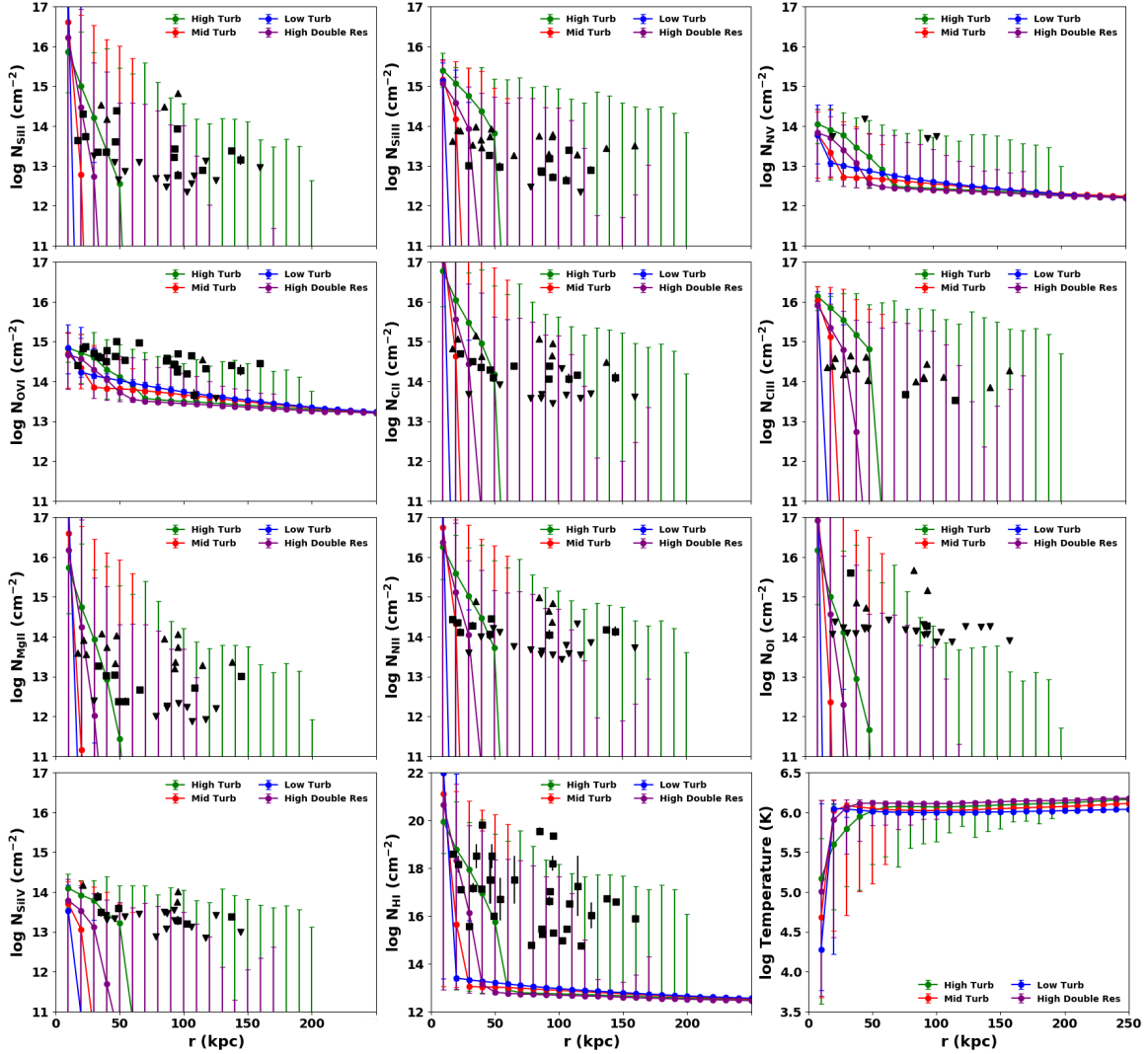
Figure 3.19: Filled circles show the 50th percentile of sightlines in 10 kpc bins for Log $N_{Si\ II}$ (first row left), $N_{Si\ III}$ (first row middle), $N_{N\ V}$ (first row right), $N_{O\ VI}$ (second row left), $N_{C\ II}$ (second row middle), $N_{C\ III}$ (second row right), $N_{Mg\ II}$ (third row left), $N_{N\ II}$ (third row middle), $N_{O\ I}$ (third row right), $N_{Si\ IV}$ (fourth row left), $N_{H\ I}$ (fourth row middle), and Temperature (fourth row right) vs. radial distance r for the Low (blue), Mid (red), High (green), and double-resolution High (purple) runs at 3 Gyrs contained to cells within the virial radius. Error bars show the 1st percentile as the lower limit and 99th percentile as the upper limit. Projections were generated for each cell where each sightline is a line integral of ion number density along the z-axis. We also show detections (black squares) and limits (black arrows) from the COS-Halos sample overlaid on our projected column densities.

Chapter 4

MODELING PHOTOIONIZED TURBULENT MATERIAL IN THE
CIRCUMGALACTIC MEDIUM III: EFFECTS OF CO-ROTATION AND
MAGNETIC FIELDS

4.1   Introduction

The circumgalactic medium (CGM) is the predominantly ionized atmosphere of diffuse baryons that extends hundreds of kpc from a galaxy, contained by the overall dark matter gravitational potential. It is responsible for regulating the galaxy's evolution through processes such as galactic accretion, starburst-driven winds, and feedback from active galactic nuclei (AGN) (e.g. Lilly *et al.*, 2013; Voit *et al.*, 2015; Crighton *et al.*, 2015; Fox and Davé, 2017; Muratov *et al.*, 2017; Tumlinson *et al.*, 2017). While this medium is often modeled as a purely hydrodynamic fluid in numerical simulations, due to its ionized nature, its dynamics and chemistry can be strongly affected by the presence of magnetic fields.

Observations have shown that magnetic fields exist in the CGM at dynamically important field strengths (Kronberg and Perry, 1982; Welter *et al.*, 1984). By correlating Faraday rotation measurements of high-redshift radio sources with those of foreground galaxies with observed Mg II absorption, the line-of-sight component of the B-field in the CGM has been found to be a few μG (e.g. Bernet *et al.*, 2008; Kronberg *et al.*, 2008; Bernet *et al.*, 2010, 2012; Farnes *et al.*, 2014; Malik *et al.*, 2020; Lan and Prochaska, 2020).

In addition to this, absorption lines have shown the CGM to be multiphase: possessing cold, $T \approx 10^4$ K, gas traced by ions such as H I and Mg II in rough pressure equilibrium with a hotter, $T \approx 10^6$ K phase that is traced by O VI and Ne VIII (e.g. Chen *et al.*, 1998; Steidel, 1998; Rudie *et al.*, 2012; Tumlinson *et al.*, 2013; Heckman *et al.*, 2017). Measurements of ion ratios, such as Si IV/O VI and N V/O VI have also been able to probe the $T \approx 10^5$ K transitioning, intermediate phase gas in the CGM (Werk *et al.*, 2016), yielding results that are inconsistent with models that assume that the various phases are in chemical equilibrium.

However, such observations have been difficult to interpret in detail, largely owing to the low densities in the CGM, which lead to low detection rates (Tumlinson *et al.*, 2017). This has left open questions about the magnetic field structure and its evolution (Kronberg and Perry, 1982; Welter *et al.*, 1984), as well as its influence on CGM dynamics, leading to several numerical simulations focused on the impact of magnetic fields on the gas beyond galaxies.

On somewhat larger scales, Dolag *et al.* (2009) ran magneto-hydrodynamic (MHD) cosmological simulations of galaxy cluster environments and found that the dissipation of the magnetic field could play an important role in the determination of the predicted magnetic field profile. Years later, Beck *et al.* (2012) ran cosmological MHD simulations to understand the evolution of B-fields in the context of Milky Way-like galactic halo formation. By injecting a magnetic field at a low rate of 1 nG Gyr^{-1}, they found it exponentially amplified to μG level near the halo center due to shocks and turbulent dynamo action, the process in which the magnetic field strengths are amplified by the stretching and twisting of magnetic field lines from turbulence (Kazantsev, 1968; Krause and Raedler, 1980; Zeldovich *et al.*, 1990; Brandenburg *et al.*, 2012). This rapid amplification was also studied in galaxy clusters in Vazza *et al.* (2014).

Other cosmological simulations of Milky Way-like galaxies have similarly found

initial B-fields to be quickly amplified to μG strengths via turbulent dynamo action. This is initially triggered by feedback processes (e.g. star formation, active galactic nuclei, supernovae, etc.), and maintained by large differential rotation of the central galaxy (e.g. Pakmor *et al.*, 2014; Rieder and Teyssier, 2016; Pakmor *et al.*, 2017; Rieder and Teyssier, 2017a,b). However, these simulations have been predominantly focused on the central galaxy and the immediate region around it, not the entire CGM.

More recently, Nelson *et al.* (2018b) ran large-scale MHD simulations as part of the IllustrisTNG project (Pillepich *et al.*, 2018) and found a correlation between the ratio of magnetic pressure to thermal pressure in the halo gas and the (g-r) color of the central galaxy. Also as part of the IllustrisTNG project, Marinacci *et al.* (2018) investigated magnetic properties of galaxy clusters and galactic halos, finding the ratio of magnetic pressure to thermal pressure reaches a maximum of 3 in the center and declines with increasing distance. Moreover, Pakmor *et al.* (2020) used cosmological zoom-in simulations of Milky Way-like galaxies to understand the B-field evolution in the context of the CGM. They found that outflows initially magnetize the CGM, and that these fields were further amplified via turbulent dynamo action to a strength of 0.1 μG at the virial radius. Nelson *et al.* (2020) also conducted cosmological MHD simulations using the IllustrisTNG model to investigate the cold gas in the CGM of massive halos with $M \gtrsim 10^{13}$ M$_\odot$, showing that such cold clouds possessed magnetic pressures that were at least 10 times greater than their thermal pressures.

In this work, we carry out the first simulation of the evolution of a magnetized Milky Way-like galactic halo that includes full non-equillibrium chemistry, rotation, and turbulence. We complement this simulation with a hydrodynamic case that is otherwise identical, allowing us conduct direct comparisons in a controlled way to better understand the impact of magnetic fields. Together, these simulations allow us

to make detailed models of both the multiphase nature of the magnetized CGM, and its observable properties shown by absorption line tracers that probe a wide variety of ionization states.

The structure of this work is as follows. In Section 4.2 we discuss the model used to simulate this environment. In Section 4.3 we compare between the co-rotating hydrodynamic case and the co-rotating MHD case, and look at how these considerations influence the phase, magnetic field structure/strengths, kinematics of ions, as well as the non-equilibrium chemistry that develops in the CGM. We conclude this work by summarizing and discussing the results in Section 4.4.

4.2   Methods

4.2.1   The Modified MAIHEM Code

To carry out non-equillibrium MHD simulations of the magnetized CGM, we used Models of Agitated and Illuminated Hindering and Emitting Media (MAIHEM[1]). MAIHEM is a cooling and chemistry package built using FLASH (Version 4.5), an open-source hydrodynamics code (Fryxell *et al.*, 2000). This package models the hydrodynamics in three-dimensions (3D) and evolves a non-equilibrium chemistry network of 65 ions, including hydrogen (H I and H II), helium (He I–He III), carbon (C I–C VI), nitrogen (N I–N VII), oxygen (O I–O VIII), neon (Ne I–Ne X), sodium (Na I–Na III), magnesium (Mg I–Mg IV), silicon (Si I–Si VI), sulfur (S I–S V), calcium (Ca I–Ca V), iron (Fe I–Fe V), and electrons. This includes solving for dielectric and radiative recombinations, collisional ionizations with electrons, charge transfer reactions, and photoionizations by a UV background.

MAIHEM was originally developed in Gray *et al.* (2015), later improved upon

---

[1]http://maihem.asu.edu/

with the inclusion of an ionizing background in Gray and Scannapieco (2016), and further updated with several charge transfer reactions, radiative recombination rates, and dielectronic recombination rates from Aldrovandi and Pequignot (1973); Shull and Van Steenberg (1982); Arnaud and Rothenflug (1985) in Gray and Scannapieco (2017). Physical cooling processes are included down to 5000 K.

Most recently, Buie *et al.* (2020b, hereafter B20) modified the MAIHEM code to simulate this gas in a dark-matter Navarro *et al.* (1996, hereafter NFW) gravitational potential, given by:

$$\rho_{\text{NFW}}(r) = \frac{\rho_0}{\frac{r}{R_s}\left(1 + \frac{r}{R_s}\right)^2}, \tag{4.1}$$

where $\rho_0 = M_{\text{halo}}\left[4\pi R_s^3 \left[\ln(1+c) - c/(1+c)\right]\right]^{-1}$ is the dark matter density normalization, M_{halo} is the mass of the halo, $R_s = R_{\text{vir}}/c$ is the scale radius while R_{vir} is the virial radius of the halo, and c is the concentration parameter of the halo. The turbulence, which is used as our driving feedback mechanism, is artificially driven according to the following equation,

$$a_{x,y,z} = a_{x,y,z}^0 \left(\frac{r + 0.3R_{\text{vir}}}{0.5R_{\text{vir}}}\right)^\alpha, \tag{4.2}$$

where $a_{x,y,z}^0$ is the original acceleration term resulting from the direct Fourier transform of the solenoidal modes ($\nabla \cdot F = 0$, where F is the artificial forcing term used in the momentum equation) (Pan and Scannapieco, 2010), r is the radius to a cell, and α is a dimensionless parameter that controls how the acceleration behaves with radius. These solenoidal modes depend on the driving scale of turbulence, total injected energy, and the autocorrelation time for the Ornstein-Uhlenbeck (OU) process that these are modeled as (Uhlenbeck and Ornstein, 1930).

Gray and Scannapieco (2016) details the equations solved in MAIHEM which are invariant under the transformation $x \to \lambda x$, $t \to \lambda t$, $\rho \to \rho/\lambda$ meaning the final steady-state abundances depend only on the product nL of the mean density and the

driving scale of turbulence, the one-dimensional (1D) velocity dispersion of the gas, σ_{1D}, and the ionizing extragalactic UV background (EUVB).

We utilize the unsplit staggered mesh (USM) algorithm which solves multidimensional ideal and non-ideal MHD problems on a Cartesian grid and the equations for these calculations are available in Lee (2013). This study specifically uses the ideal MHD solvers, and we also make use of a hybrid Riemann solver that uses the Harten Lax and van Leer (HLL) solver (Einfeldt *et al.*, 1991) in places with strong shocks or rarefactions and the Harten–Lax–van Leer–Contact (HLLC) solver (Toro *et al.*, 1994; Toro, 1999) in smoother flows to stabilize the code as turbulence ensues. We refer the reader to Gray *et al.* (2015) and Gray and Scannapieco (2016) for further details.

4.2.2   Model Parameters

We conducted a suite of numerical simulations that model an 800 kpc box with periodic boundaries using Static Mesh Refinement (SMR) to accurately capture important structures that develop in the halo as turbulence ensues. The simulations are run in a Milky Way mass dark matter halo of 10^{12} M$_\odot$, with a virial radius of 220 kpc and a concentration parameter of 10. Note that the virial radius remains constant with time, and the simulations are not run in a comoving domain.

Cosmological parameters are solely used to simulate the gravitational acceleration of the baryonic matter and are from the Planck 2018 Collaboration (Aghanim *et al.*, 2018). They are $h = 0.674$, $\Omega_m = 0.315$, $\Omega_b = 0.049$, and $\Omega_\Lambda = 0.685$, where h is the Hubble constant in units of 100 km s^{-1} Mpc^{-1}, and Ω_m, Ω_b, and Ω_Λ, are the total matter, baryonic, and vacuum densities, respectively, in units of the critical density.

The resolution was set to that in B20, meaning that for $R \gtrsim 300$ kpc the domain was at a resolution of 64^3 which translates to 12.5 kpc, for $300 \gtrsim R \gtrsim 250$ kpc the resolution was 128^3 which translates to 6.2 kpc, $250 \gtrsim R \gtrsim 225$ kpc the resolution

was 256^3 which translates to 3.1 kpc, and for 225 kpc $\gtrsim R$ the resolution was 512^3 which translates to 1.6 kpc.

Note that Buie II *et al.* (2018, hereafter B18) used a smaller, sub-parsec resolution and a smaller turbulent driving scale as compared to the runs presented here. Both sets of simulations inject turbulence with stirring modes between $L/3 \leqslant 2\pi/k \leqslant L$, but in B18, L was set to be on the scale of the box, 100 pc, while here it is chosen to be 30 kpc. This is about the size of the Milky Way disk as we assume such turbulence would be primarily driven by outflow/inflow processes on the scale of the disk. However, it is misleading to match these physical scales directly, because for a fixed ionization parameter, the results of the isotropic turbulence simulations such as presented in B18, depend on the product of the density and the driving scale nL, rather than directly on L. As the densities that were used in this previous work were orders of magnitude larger than those found in the study described here, nL is comparable between the two sets of simulations, even though L is not.

Likewise, it is the resolution in units of L rather than in physical units that is the key measure of resolution. In B18 the resolution was $\Delta x = L/128$ while in the current case it is slightly lower, $\Delta x \approx L/20$, where 20 results from the resolution divided by the driving scale of turbulence. However, B20 also conducted a resolution study by doubling the resolution to 1024^3 or 0.8 kpc and found that while the cool structures that developed were smaller in scale, the overall properties and conditions in the halo such as temperatures, densities, and resulting column densities, remained in agreement with the original resolution counterpart. MHD simulations as large as 1024^3 that are run for 9 Gyrs are prohibitively expensive, and we predict that in such simulations, the resulting cool structures would be smaller but the overall properties would be largely similar to the runs presented here.

We initialize the medium with a Keplerian circular velocity modified by the ob-

servational findings from the Mg II studies of Ho *et al.* (2017). Specifically, we use their Equation A2 to inform how the velocities should fall off along the minor axis, which is chosen to be the y axis in our runs. This gives a rotational velocity of

$$v_{\text{rot}} = f_{\text{rot}} \sqrt{\frac{4\pi G r^2 \rho_{\text{NFW}}(r)}{3}} H_s(y), \tag{4.3}$$

where G is the gravitational constant, and $H_s \equiv \exp\left(-|y|/50 \text{ kpc}\right)$ is the dependence of the circular velocity with scale height, and f_{rot} is an overall scaling parameter we set to 60%. In this case the spin parameter of the gas, λ defined as

$$\lambda = \frac{J}{\sqrt{2} M_{\text{gas}} V R}, \tag{4.4}$$

where J is the total angular momentum within a sphere of virial radius R along with its gas mass M_{gas}. V is the circular velocity at the virial radius, $V = \sqrt{G M_{\text{total}}/R}$. The chosen f_{rot} results in $\lambda \approx 0.03$ in our halos, in line with numerical studies of galactic dark matter halos (Bullock *et al.*, 2001; Macciò *et al.*, 2008; Bryan *et al.*, 2013).

In all our runs, the gas was initialized with a fractional ion abundance of 0.3 $Z_\odot$ in collisional ionization equilibrium (CIE) at the virial temperature of the halo, $T = 1.2 \times 10^6$ K and average sound speed of 166 km s^{-1}. Following initialization, the medium is allowed to evolve according to the non-equilibrium chemistry. We note that our simulations assume the metallicity to be constant throughout the halo, while observations support a CGM that is significantly chemically inhomogeneous (Zahedy *et al.*, 2019; Buie *et al.*, 2020a). We also choose a redshift zero Haardt and Madau (2012, hereafter HM2012) EUVB whose specific intensity was normalized to 8.23×10^{-24} erg cm^{-2} s^{-1} Hz^{-1} sr^{-1} at the Lyman limit to irradiate the gas in the runs.

We conduct runs that build off of the previous High run from B20, which was able to match many ion observations of nearby star-forming galaxies' CGMs. That
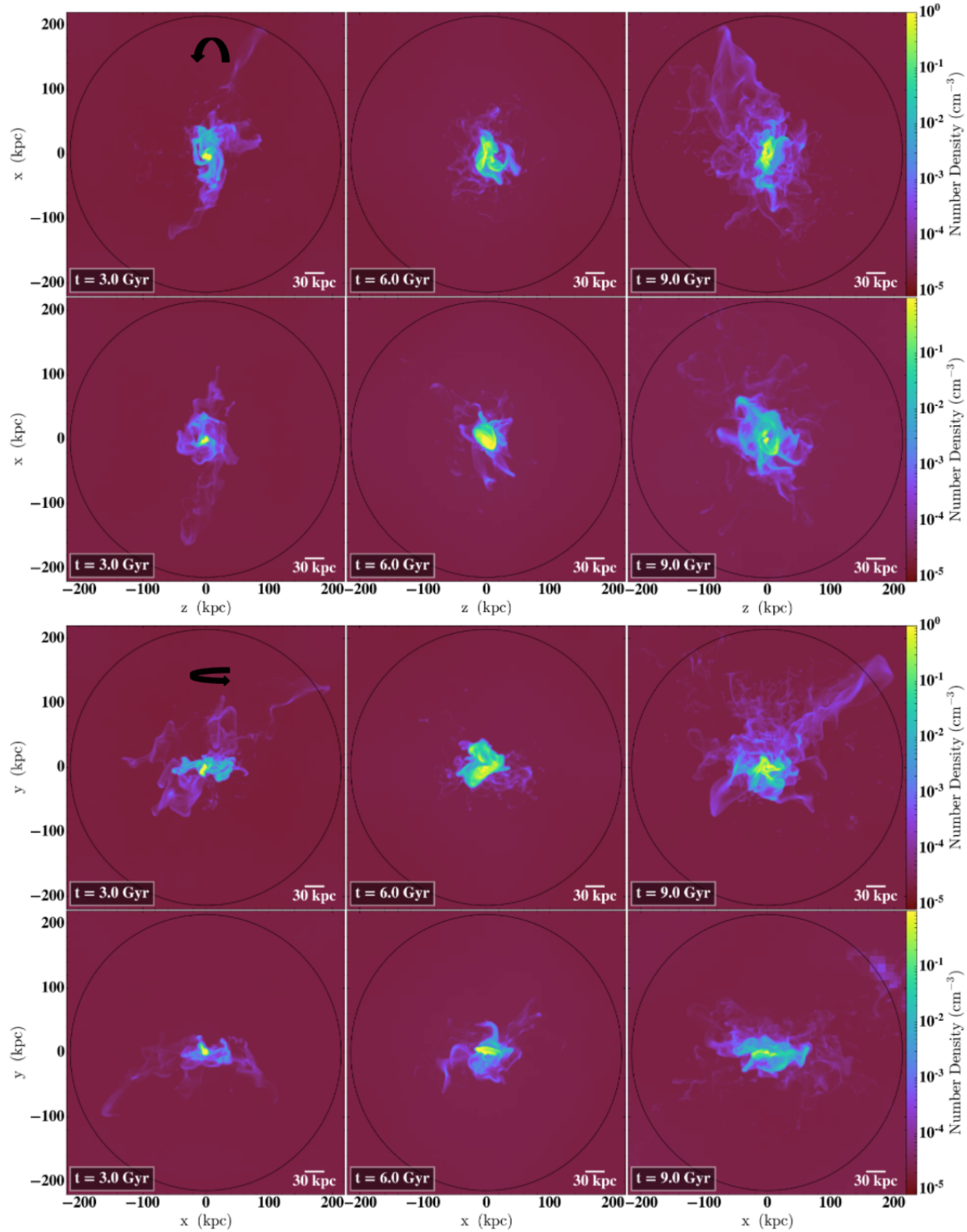
Figure 4.1: Projections of mass-weighted number densities at 3 Gyrs (left), 6 Gyrs (middle), and 9 Gyrs (right). The first and second rows show these from a face-on perspective for the Hydro and MHD Rot halos, respectively. The third and forth rows show these from an edge-on perspective for the the Hydro and MHD Rot halos, respectively. We show black arrows to indicate the direction of rotation in the halo and black circles to show the virial radius at $R_{\mathrm{vir}} \approx 220$ kpc.

83

run was conducted by setting α in Equation 4.2 to -1, and used the same driving scale for turbulence, 30 kpc. This ensured turbulent stirring was strongest towards the center and fell off with radius. Observationally, non-thermal motions that are derived from Voigt profiles are typically smaller for low-ionization state ions, which are more often found near the host, than in higher ionization state ions which may reside at a range of radii from the central galaxy (Tumlinson *et al.*, 2013; Churchill *et al.*, 2015; Werk *et al.*, 2016; Faerman *et al.*, 2017). However this may be largely due to the fact low-ionization-state ions occur preferentially in colder material with higher physical densities than higher-ionization-state ions, meaning that at the same column depth they will probe smaller physical scales, wherein turbulence is much smaller. Additionally, Buie *et al.* (2020a) conducted a MCMC investigation of absorbers in the CGM of nearby galaxies and found the turbulent velocities had no definitive radial trend, but instead covered a range in σ_{1D} between $11 - 60$ km s^{-1}, consistent with our turbulent stirring.

The turbulent stirring employed here, and in the previous B20 study, also allows us to more accurately capture the stronger central feedback of actively star-forming galaxies, as well as the impact of gas accreted from the intergalactic medium, which is likely to deposit the most energy *per unit volume* near the center of the halo. This choice in turbulent stirring led to an average one-dimensional velocity dispersion $\sigma_{1D} = 41$ km s^{-1}. In addition to this turbulent stirring treatment, the aforementioned co-rotation prescription was also considered in the run which we call the Hydro Rot run.

The second run we conducted further included a seed magnetic field in the z-direction of 0.1 μG run in ideal MHD. This choice of initial magnetic field strength translated to a plasma β, defined as the ratio of thermal pressure to magnetic pressure, of ≈ 170. It also used the same turbulent stirring and co-rotation prescriptions and

Figure 4.2: Panels show the gas mass vs. time for the Hydro Rot (blue) and MHD Rot (gold) runs, as compared to our run without rotation from B20, the High run (green). The left panel shows the total gas mass within $R_{\rm vir}$. The middle panel shows the gas mass between 12 kpc and $R_{\rm vir}$, omitting the central region. The right panel shows the gas mass within $R_{\rm vir}$ with $T < 10^5$ K and includes the central region.

is called the MHD Rot run.

Previously in B20, the simulations were run for 3 Gyr until they reached a global equilibrium such that the change in total energy was less than 0.25% per timestep. With the addition of co-rotation, we ran them for 9 Gyrs as interesting features developed post 3 Gyrs and we wanted to capture the full saturation period of the magnetic field in the MHD run.

Note that these simulations are run in a static domain for 9 Gyrs which do not emulate the mass growth that would likely be experienced by a real galaxy in this evolutionary time. Such mass growth would likely lead to increased turbulent motions as new gas enters the CGM. Furthermore, these interactions would likely increase the magnetic field in these areas due to the twisting of magnetic field lines.

4.3   Results

4.3.1   Overall Evolution

To give the reader visual context for the changes in structure as our halos evolve, we show projections of the mass-weighted number density from face-on and edge-on

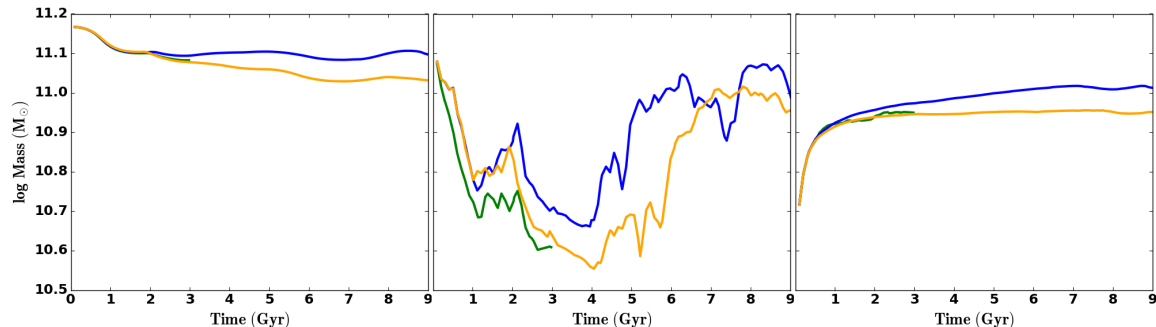**Figure 4.3:** Total cooling in the CGM halo vs. time for the Hydro Rot (blue) and MHD Rot (gold) runs, as compared to our run without rotation from B20, the High run (green). We omit data within 12 kpc as this material primarily traces gas within the galaxy. The grey dashed line shows the turbulent energy injection rate from B20 that was found to be 1.3×10^{42} erg s^{-1} for the High run.

perspectives for the Hydro Rot and MHD Rot halos in Figure 4.1, at 3, 6 and 9 Gyrs. Furthermore, Figure 4.2 shows the evolution of the gas mass within $R_{\rm vir}$ in our new simulations, compared to the High simulation from B20, the mass between 12 kpc and $R_{\rm vir}$, as well as the mass in gas with $T < 10^5$ K. As in our previous simulations, gas within $r \approx 30$ kpc cools in the initial ≈ 500 Myrs, forming a low-pressure region in the center of the halo, which promotes an accretion flow of gas to the inner 12 kpc which may be seen from the middle panel of Figure 4.2. Such cooling may also be inferred from the rapid rise in cool gas observed in the right panel of this figure. Gas

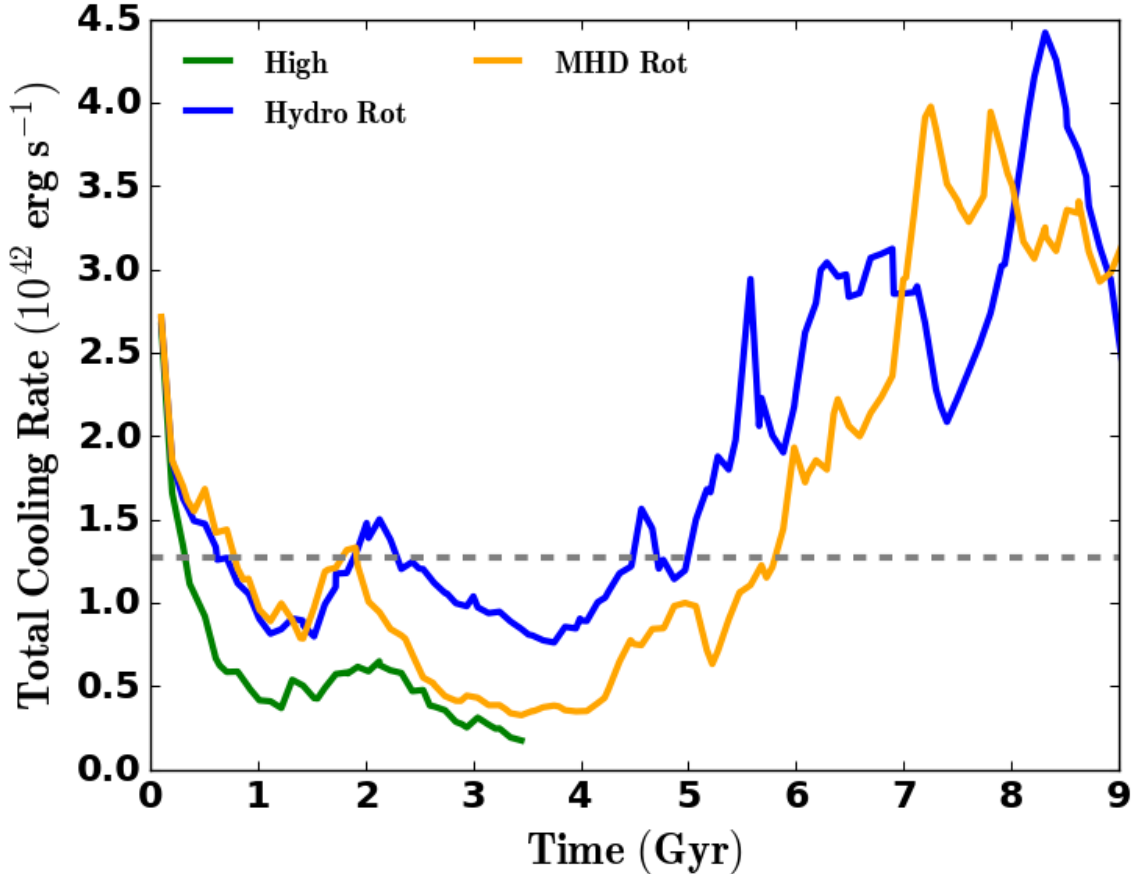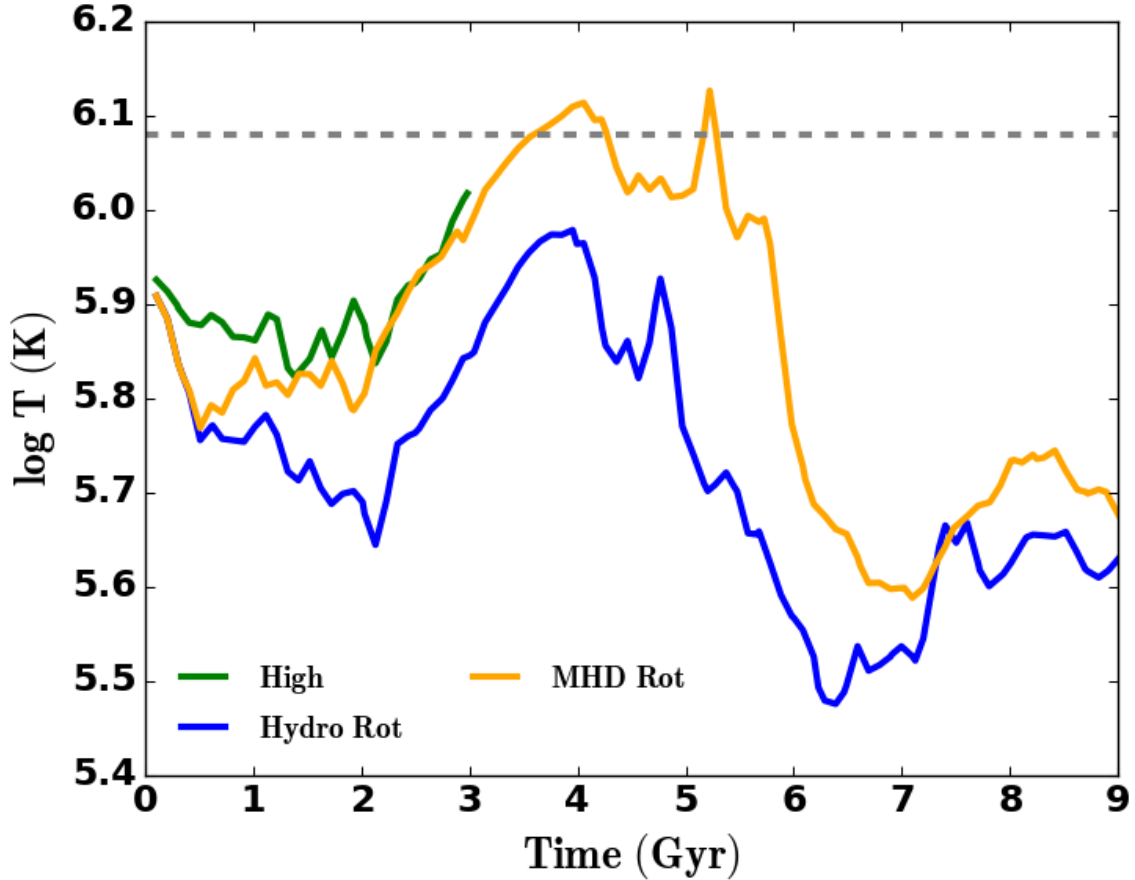**Figure 4.4:** Mass-weighted average temperature in the virial halo vs. time for the Hydro Rot (blue) and MHD Rot (gold) runs, as compared to our run without rotation from B20, the High run (green). We omit data within 12 kpc as this material primarily traces gas within the galaxy.

near the virial radius is pushed beyond it by the initial turbulence, a feature indicated by a decrease in mass shown in the left panel of this figure.

The accretion flow results in an accretion shock that forms near the core and gradually moves outward, dispersing the gas near the core throughout the halo. One observes this feature by looking at the middle panel of Figure 4.2 that shows a rise in gas mass between 1 and 2 Gyrs. We also see the initialization of the turbulence, followed by the accretion shock, both push about 14% of the baryonic mass beyond R_{vir} in the first 2 Gyrs.

Figure 4.5: Number density vs. radius showing the total mass in a bin for the Hydro Rot (top) and MHD Rot (bottom) runs. We specifically show these at 3 (left), 6 (middle), and 9 (right) Gyrs. Plots are made using 128 bins for the x and y quantities. For reference, we include a black dashed line to show the number density at 10^{-2} cm^{-3} and a solid line to show this at 10^{-4} cm^{-3}.

At approximately 2 Gyrs, the accretion shock leaves the halo. Following this, between 2 - 4 Gyrs, both of the new runs follow similar evolutionary trends in their mass confined to the intermediate region between 12 kpc and $R_{\rm vir}$ with the MHD case showing lower mass during this time. This results primarily from the mass loss that occurs as it leaves the halo, which may be seen from the downward slope in the gold line of the left panel. This may in part be influenced by additional pressure support from the amplified magnetic field, described in more detail in §3.3. The amount of gas cooler than 10^5 also steadily rises in both runs for the remainder of the evolution.

As ambient gas in the MHD halo is at lower densities, it is unable to cool as efficiently as compared to the Hydro Rot run. This is shown by the total cooling in Figure 4.3 in additon to the lower amount of cold mass found in this run which may

be seen in the right panel of Figure 4.2. Mass loss is prolonged in the MHD Rot run, continuing on for nearly 7 Gyrs. The total gas mass fluctuates at $\lesssim 1.1 \times 10^{11}$ M$_\odot$ in the MHD Rot run, compared to the Hydro Rot halo which instead fluctuates between 1.2 - 1.3 $\times 10^{11}$ M$_\odot$ for the remainder of its evolution.

We find that the initial co-rotation along with the continuously driven turbulence adds heat to the hot component, thereby raising its pressure and entropy. We see these as subsonic motions on the order of ≈ 10 km s^{-1} and they persist throughout the evolution of both runs. This increased pressure and entropy causes hot gas to buoyantly rise beyond the virial radius. Some of this gas travels far enough to re-enter the 800 kpc box from opposite sides which starts at ≈ 4 Gyrs and is a consequence of our periodic boundary conditions. We consider this to be a numerical artifact and it does not influence the results of this study. The MHD Rot run possesses a hotter ambient medium with higher levels of entropy and pressure, thus more mass leaves its halo. This rising pressure and entropy are discussed in more detail in the following section.

When looking at the mass-weighted average temperature, shown in Figure 4.4, we see a positive slope that approaches T_{vir} in the MHD case and $< T_{\mathrm{vir}}$ in the Hydro Rot case. Gas within the MHD Rot's halo maintains these high temperatures over a longer duration, approximately a Gyr longer than in the case of no MHD.

Both runs appear to come out of their cooling minima after nearly 4 Gyrs of evolution. Soon after, we also see the mass between 12 kpc and R_{vir} rise in the Hydro Rot halo. This is largely due to the ejection of material from the central region and somewhat from the re-accretion of material outside R_{vir}. The ejection of material from the center that causes the rise in mass seen in this region is observed 2 Gyrs later in the MHD Rot halo as the magnetic field helps to keep cold gas contained to the center for longer periods of time. Furthermore, these runs maintain their increased masses
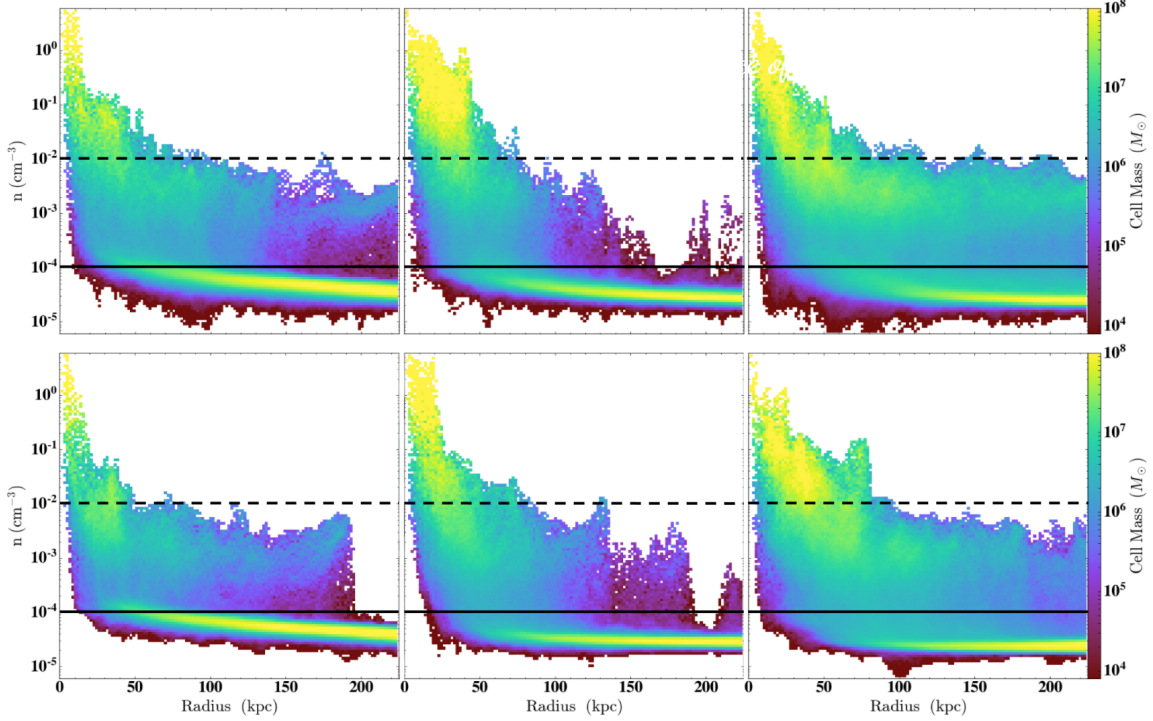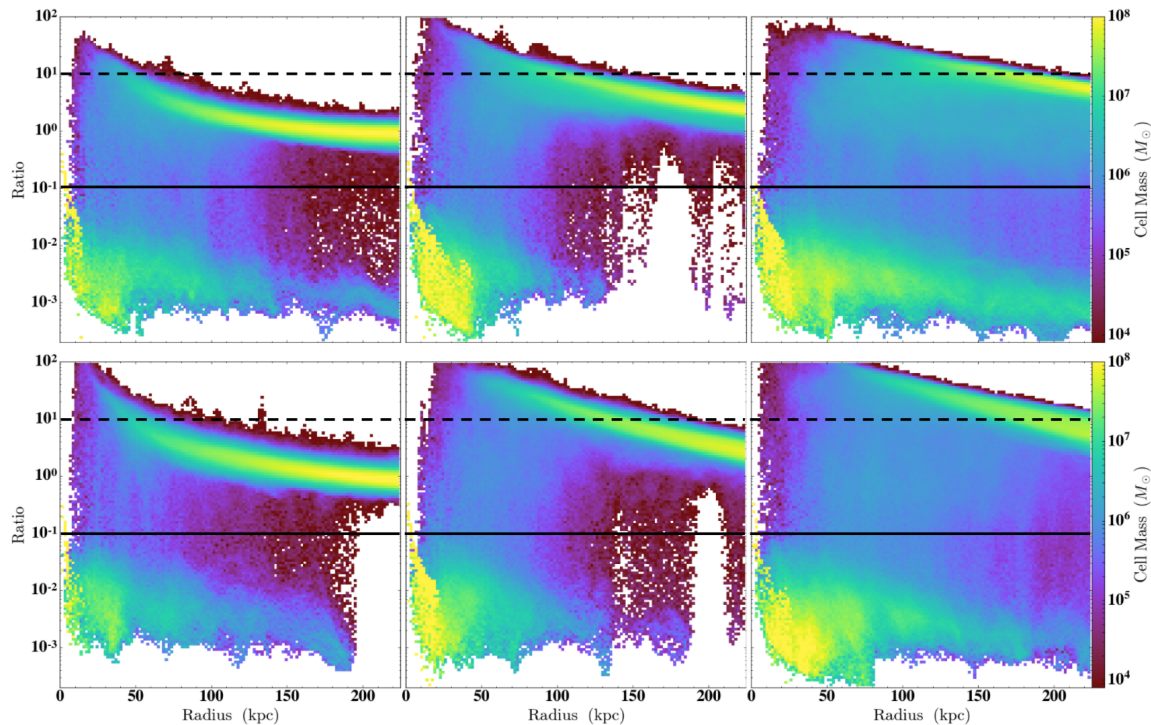
Figure 4.6: $t_\mathrm{cool}/t_\mathrm{ff}$ ratios vs. radius showing the total mass in a bin for the Hydro Rot (top) and MHD Rot (bottom) runs. We specifically show these at 3 (left), 6 (middle), and 9 (right) Gyrs. Plots are made using 128 bins for the x and y quantities. For reference, we include a black dashed line to show this ratio at 10 and a solid line to show this at 10^{-1}.

in this interim region for the remainder of their evolution. The mass-weighted average temperature trends approach a minimum, with log T being ≈ 5.6 in the MHD Rot halo and 5.5 in the Hydro Rot halo prior to rising for the remainder of the simulation.

4.3.2 CGM Structure

In Figure 4.5, we show the radial profile of the number density, n, at 3, 6 and 9 Gyrs. Gas is found at a variety of densities during these times, with most of the mass tracing the diffuse ambient medium and dense structures, such as clouds and filaments. The Hydro Rot run tends to have a wider range of densities, and at 6 Gyrs, it shows a large amount of mass with $n > 10^{-2}$ cm^{-3} spread across the inner 50 kpc of the halo. In the MHD case, however, mass consolidates to smaller radii,

reaching densities above 10^{-1} cm^{-3} along with possessing mass beyond 125 kpc with $n \approx 10^{-3}$ cm^{-3}.

After 6 Gyrs, the halos become very dynamic with angular momentum transfer driving dense, cold outflowing gas throughout, some of which travels beyond R_{vir} by 9 Gyrs, while also having infalling, cooling gas. Both raise the density in the ambient medium by 9 Gyrs. Also at this time, we can see that both runs have moved their mass outward, with less of it having $n \gtrsim 10^{-1}$ cm^{-3} in the inner 50 kpc and more with $10^{-2} < n < 10^{-4}$ cm^{-3} spread throughout the halos.

In Figure 4.6, we examine the radial profile of the ratio of cooling times to free fall times, $t_{\mathrm{cool}}/t_{\mathrm{ff}}$, for these runs at 3, 6, and 9 Gyrs where

$$t_{\mathrm{cool}} \equiv \frac{E_{\mathrm{in}}}{\sum_i \Lambda_i(T, Z, n_i)}, \tag{4.5}$$

$$t_{\mathrm{ff}} \equiv (2r/g)^{1/2}, \tag{4.6}$$

E_{in} is the internal energy, and i denotes the $i-th$ ion.

This ratio gives insight into the self-regulated balance maintained between gas condensing out of the ambient medium and feedback from the host galaxy in the form of an active galactic nuclei (AGN), star formation, and/or supernovae. Once triggered, such feedback may prevent further condensation from the ambient halo (e.g. Silk, 1977; Gaspari *et al.*, 2012; McCourt *et al.*, 2012; Voit *et al.*, 2015; Voit *et al.*, 2017).

The origin of this ratio arises from early theoretical work which attemped to understand thermal instabilities in the galactic context (e.g. Hoyle, 1953; Field, 1965; Rees and Ostriker, 1977). When this ratio becomes too low (i.e. $t_{\mathrm{cool}}/t_{\mathrm{ff}} \lesssim 1$), gas may condense out of the halo and rain onto the central galaxy. As gas precipitates, any one of the aforementioned energetic feedback processes may come into play which raises this ratio in the ambient halo to ≈ 10. This cycle facilitates the formation of a
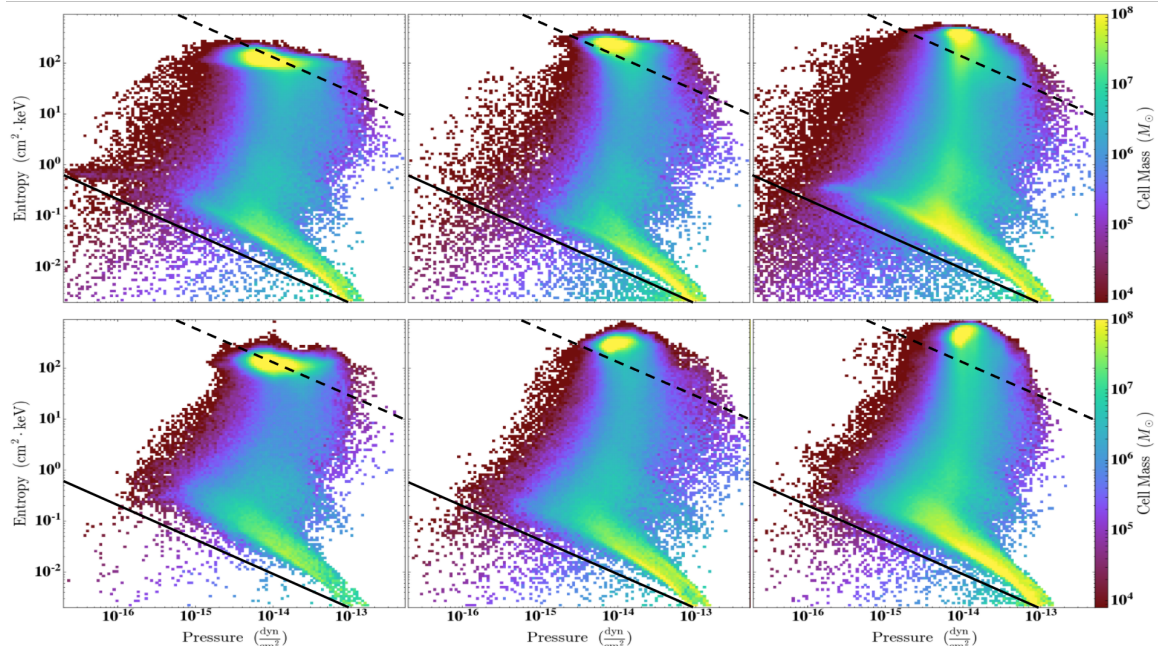
Figure 4.7: Entropy vs. thermal pressure showing the total mass in a bin for the Hydro Rot (top) and MHD Rot (bottom) runs. We specifically show these at 3 (left), 6 (middle), and 9 (right) Gyrs. Plots are made using 128 bins for the x and y quantities. For reference, we include a black dashed line to show the entropy-pressure profile at T_{vir} and a solid line to show this at 5000 K.

multiphase medium around galaxies, especially near the central regions of the CGM.

Others have conducted simulations of the CGM, testing different values of $t_{\mathrm{cool}}/t_{\mathrm{ff}}$ $\lesssim 10$ and their impacts on the development of a multiphase medium (e.g. McCourt *et al.*, 2012; Sharma *et al.*, 2012; Gaspari *et al.*, 2017; Choudhury *et al.*, 2019; Stern *et al.*, 2019), however Esmerian *et al.* (2021) produced a bimodal distribution for these ratios in their Feedback in Realistic Environments (FIRE) simulations of Milky Way-like galaxies. Looking at our halos, we find a similar bimodal distribution for $t_{\mathrm{cool}}/t_{\mathrm{ff}}$, resembling what was found in the Esmerian *et al.* (2021) simulations. The hot and diffuse ambient medium lies between 1 - 100, while the other traces $T \lesssim 10^5$ gas and lies between 10^{-4} - 10^{-1}. We also find a slightly wider distribution of $t_{\mathrm{cool}}/t_{\mathrm{ff}}$ ratios in the MHD Rot case at 9 Gyrs. This run possesses gas with ratios beyond 100 that traces low densities around 10^{-5} cm^{-3}, lying above and below the central

disk-like structure.

We find that earlier in the simulations, this extraplanar gas (not shown), is hot with temperatures $\gtrsim T_{\mathrm{vir}}$ and $t_{\mathrm{cool}}/t_{\mathrm{ff}}$ ratios $\gtrsim 10$. This is likely a consequence of the turbulent stirring, that we set to be strongest near the center, along with this region not having the additional cooling that results from the further mixing brought on by the co-rotation of gas. After ≈ 6 Gyrs, densities in these regions increase in the Hydro Rot run. During this stage, matter falls towards the center from above and below the central disk-like structure. This differs from the MHD case in which infalling matter has more angular momentum and thus funnels through the $y = 0$ plane, within the extended disk. At 9 Gyrs, these regions of cooler gas above and below the disk in the Hydro Rot run extends much farther as compared to the MHD case.

Lastly, we examine the entropy and thermal gas pressure profiles, again, at 3, 6, and 9 Gyrs in Figure 4.7. At 3 Gyrs, the ambient medium possesses a maximum $K \approx 100$ cm^2 keV in both runs which grows to about 350 and 500 cm^2 keV by 9 Gyrs in the Hydro and MHD Rot halos respectively, meaning that unless it is mixed into colder material, its cooling time is much longer than a Hubble time (Voit *et al.*, 2002; Oh and Benson, 2003). We also find the additional heating that results from the continuous stirring and initialized co-rotation previously mentioned in §3.1 causes the ambient medium in both runs to be more constrained to $\approx 10^{-14}$ dyn cm^{-2} by 9 Gyrs. We further find the MHD Rot run possesses a pressure profile that spans a smaller range as compared to the non-MHD case at all times. This may also be seen in gas transitioning between the cold and hot phases with entropy values of 0.1 - 10 cm^2 keV.

Cooling and heating gas also lies across a nearly constant pressure range in both runs. We find that gas with $T \lesssim 10^5$ K possesses entropies < 1 cm^2 keV, and has a wider range of pressures between 10^{-16} - 10^{-13} dyn cm^{-2}. In both runs, some of
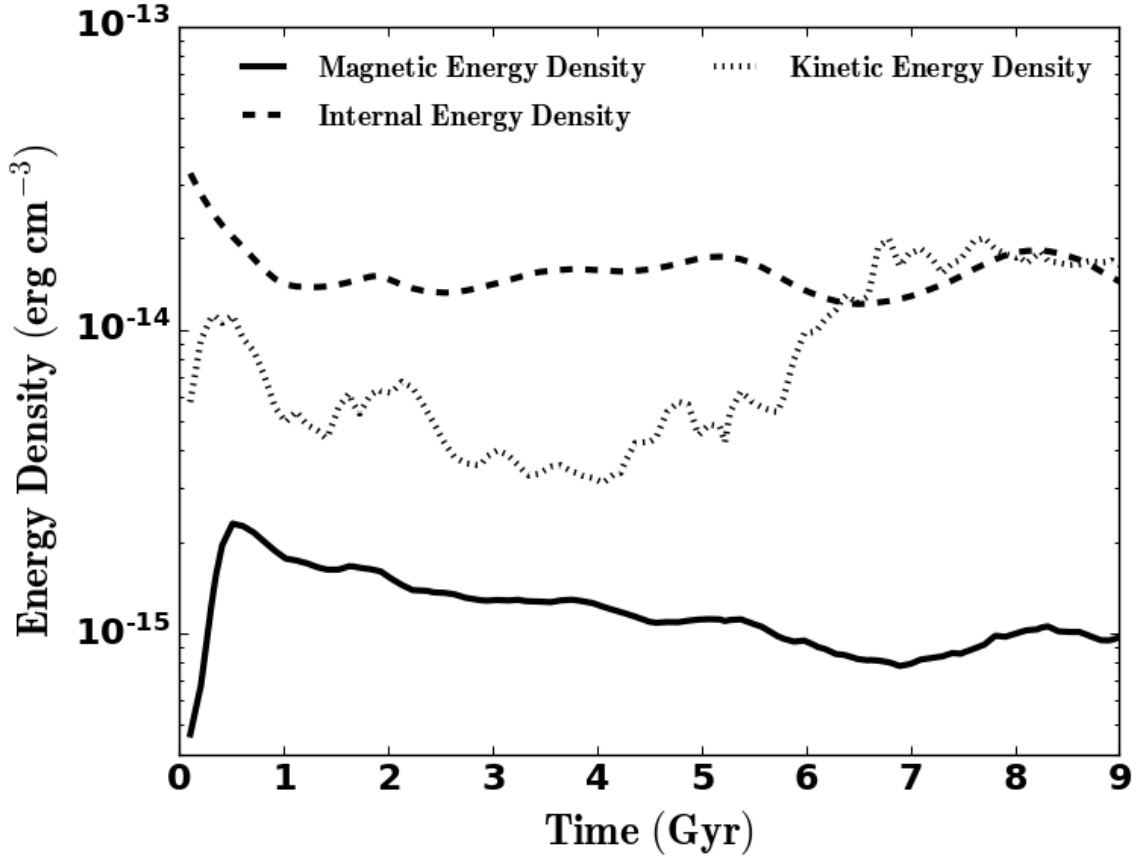
Figure 4.8: Volume-weighted average magnetic energy density, u_{B} (solid), internal energy density (dashed), and kinetic energy density (dotted) in the CGM gas between $12 < r < R_{\mathrm{vir}}$ vs. time for the MHD Rot run.

the mass is able to cool beneath our temperature floor at 5000 K, more of which is seen in our Hydro Rot run. This is where molecular cooling may become dynamically relevant, however this is not included in our simulations. By 9 Gyrs, both runs show lower entropy gas with $K \lesssim 0.1$ cm^2 keV that may be found at lower pressures below 10^{-15} dyn cm^{-2}. Further analysis shows us that this low thermal pressure gas has temperatures ranging from $\approx 10^{4-5}$ K as well as moderate densities around 10^{-3} cm^{-3}. Lastly, we see the ambient medium possesses a nearly isentropic entropy profile at all times in both of our runs, shown in Figure 4.16 in the Appendix.

Finally, the continuous turbulent stirring along with the initialized co-rotation also
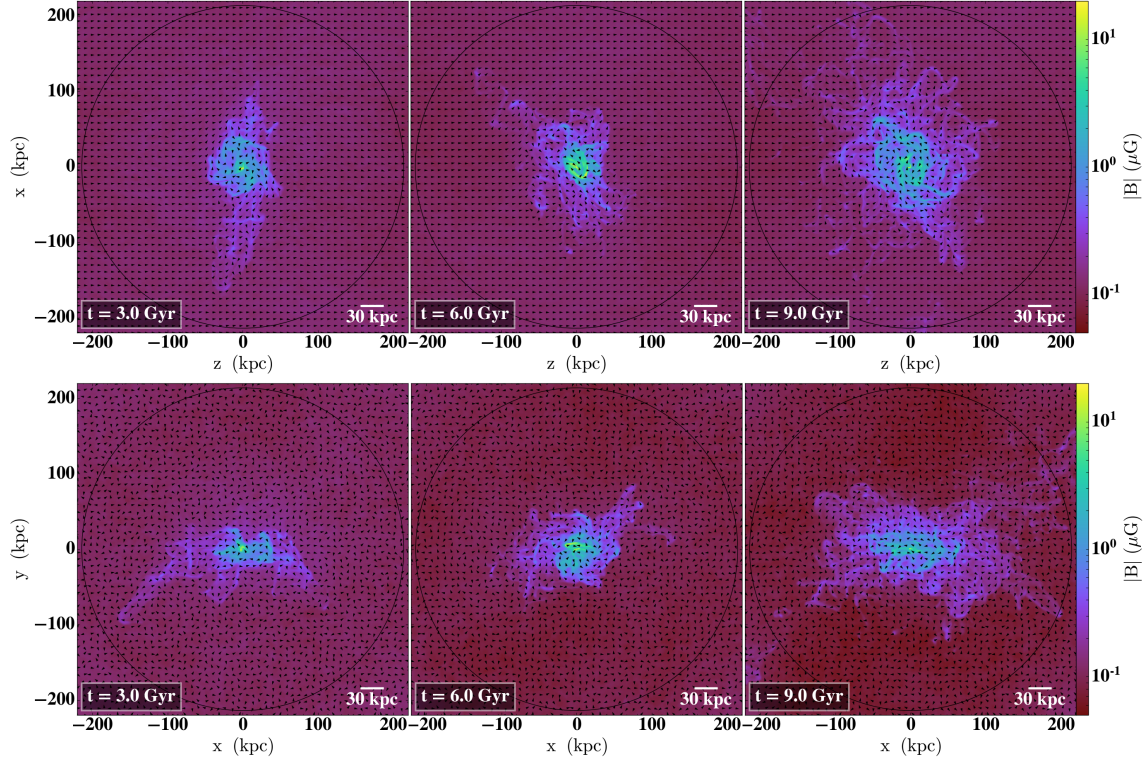
Figure 4.9: Density-weighted projections of $|B|$ at 3 (left), 6 (middle), and 9 (right) Gyrs for the MHD Rot run. Projections through the halo from face-on and edge-on perspectives are shown in the top and bottom rows respectively. A black circle shows the virial radius at $R_{\rm vir} \approx 220$ kpc along with black quivers showing the direction of the normalized magnetic field vectors.

raises the pressure in the medium beyond $R_{\rm vir}$ (not shown). We find that pressures in the medium beyond $R_{\rm vir}$ fluctuate between 6 - 9 $\times$ 10^{-15} dyn cm^{-2}, slightly lower than those found in the hot component within the halo. As gas re-enters the box, it interacts with buoyantly rising gas between 300 and 400 kpc. The periodic fluctuation in pressure beyond $R_{\rm vir}$ is not seen in the gas inside $R_{\rm vir}$. It is unclear if these pressures outside of the virial radius have any influence the observable features within it, however, we do observe a slight increase of the temperature in this distant gas.
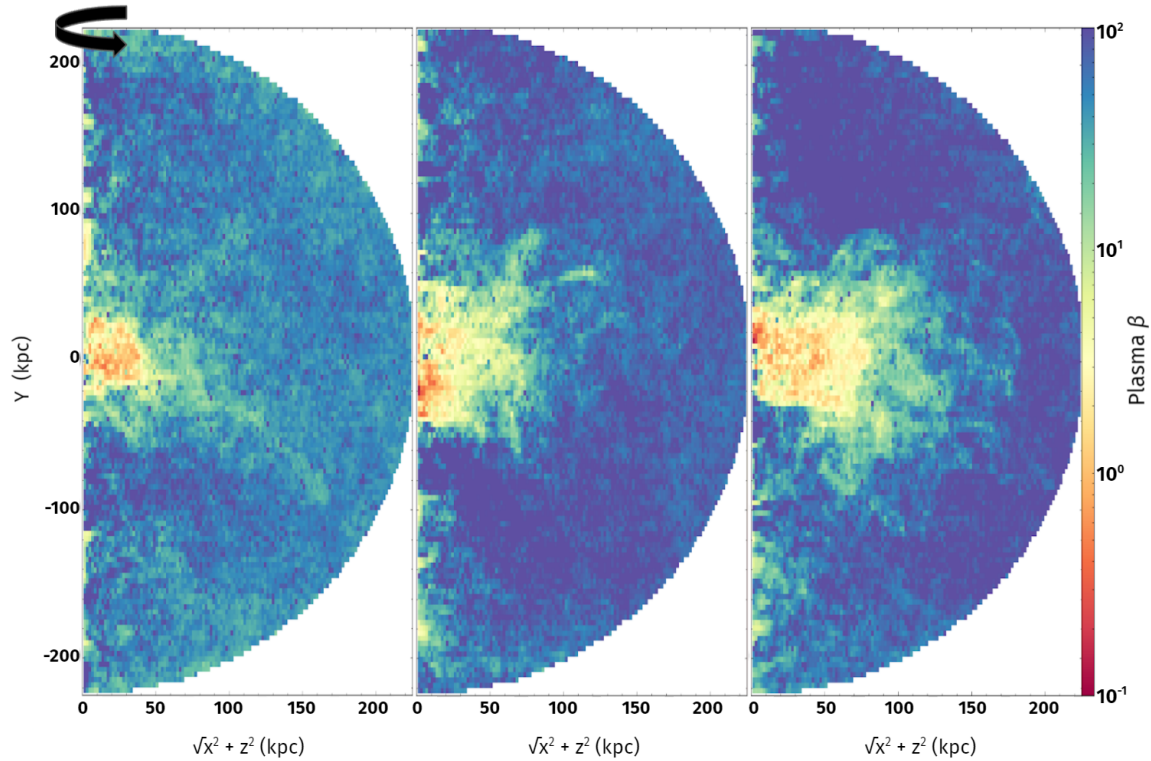
Figure 4.10: Height vs. $\sqrt{X^2 + Z^2}$ maps showing the mass-weighted average plasma β in a bin at 3 (left), 6 (middle), and 9 (right) Gyrs for the MHD Rot run. Plots are made using 128 bins for the x and y quantities.

4.3.3   Magnetic Fields

Next, we examine the magnetic field in the MHD Rot run and show the magnetic, internal, and kinetic energy densities as a function of time in Figure 4.8. We remind the reader that this run began with a seed $B_z = 0.1$ μG which corresponds to $u_B = B^2/2\mu_0 = 4 \times 10^{-16}$ erg cm^{-3} and a plasma β of ≈ 170.

The magnetic energy density grows very rapidly as the turbulent gas cools towards the center, amplifying u_B to nearly 5 times its initial value within 500 Myr. For comparison, u_B is able to reach ≈ 12 % of the internal energy density and ≈ 35 % of the kinetic energy density in the CGM at this time. Following this, u_B saturates until ≈ 7 Gyr where it settles to about 5% of the kinetic energy density for the remainder of its evolution. $|B|$ also fluctuates about 0.12 μG at this time.

As before, we take a closer look at the simulation at 3, 6, and 9 Gyrs, opting to show the density-weighted projections of $|B|$ from edge-on and face-on perspectives at these times in Figure 4.9, overlaid with black quivers that indicate the normalized magnetic field vectors.

Higher magnetic fields strengths between 1-10 μG are found in denser structures such as the cool, extended disk-like gas structure centered at $y = 0$ and cooling filaments found throughout the halo. We generally find $|B|$ decreases more steeply above and below the central disk-like gas structure rather than along the plane of it. $|B|$ strengths nearing a μG may be found out to $r \approx 100$ kpc at 3 Gyr, with these strengths extending to 150 kpc by 9 Gyrs as increased amounts of dense filaments and clouds are dispersed throughout the halo during this time. A time of 9 Gyrs corresponds to when the halo shows outflowing material along with inflowing cooling gas from beyond R_{vir}. The outflowing gas is able to carry magnetic energy from the central region out to distant radii, further magnetizing the halo. Although higher B-field strengths may be found at more distant radii during this later time in the MHD Rot run's evolution, we observe minimal difference in the $|B|$ radial profile throughout its evolution.

In Figure 4.10 we show the distribution of average β as a function of height and $\sqrt{x^2 + z^2}$ distance. As the halo evolves, the thermal pressure associated with the ambient medium increases as it heats and becomes more diffuse. This is shown by the increased volume with $\beta \approx 100$ while the gas with β values $\lesssim 1$ is largely found within the extended disk-like structure at all times. Interestingly, gas above and below this structure and beyond 40 kpc, is mostly hot and diffuse, however, also possesses pockets where it is equally supported by thermal and magnetic pressures. These may be colder voids as higher temperatures would lead to higher β's.

The gas with β values $\lesssim 1$ may be susceptible to magnetic draping, an effect in

97
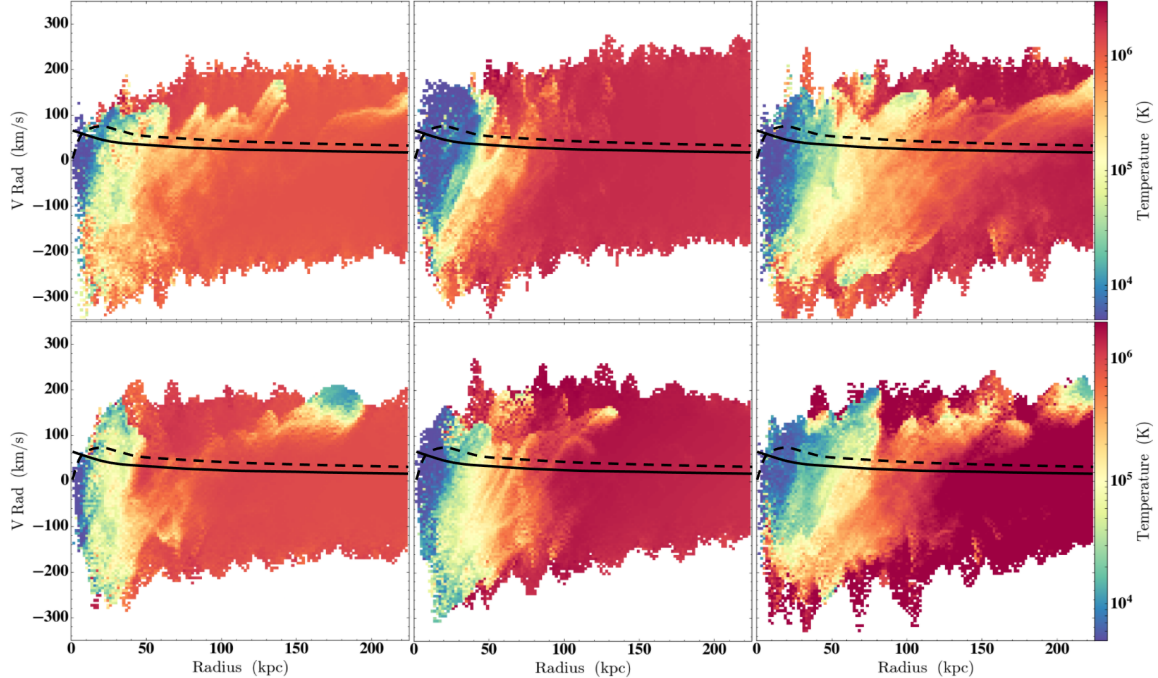
Figure 4.11: The mass-weighted average temperature as a function of radial velocity and radius for the Hydro Rot (top) and MHD Rot (bottom) runs at 3 (left), 6 (middle), and 9 (right) Gyrs. Plots are made using 128 bins for the x and y quantities. For reference, we include a solid black line to show the amplitude of the turbulence and a black dashed line to show the amplitude of the initial v_{rot} at y = 0.

which a gas cloud moving through a magnetized plasma is able to rapidly build up a magnetic layer which may shield it from developing instabilities (e.g. Semenov and Bernikov, 1980; Dursi and Pfrommer, 2008; Cottle *et al.*, 2020). When looking at the quivers in Figure 4.9, we indeed see magnetic fields that have oriented themselves to be predominately parallel to the surface of the cool structures such as the extended central disk-like structure. We speculate that this allows for the persistence of the extended disk-like structure at later times as mixing directly above and below it is inhibited.

Furthermore, the gas that we observed to have low thermal pressures in Figure 4.7 tends to be supported by a comparable amount of magnetic pressure as compared to thermal pressure. In fact, we find the gas with $K \lesssim 0.1$ cm^{-2} keV typically corresponds to gas with β values $\lesssim 1$.

4.3.4 Kinematics & Ions

Finally, we compare the kinematics and distributions of ions in the two runs, the properties that are most often constrained by observations. In Figure 4.11, we show the mass-weighted average temperature as a function of radial velocity, V_{radial} and radius at 3, 6, and 9 Gyrs, overlaid with the amplitude of turbulence and initial v_{rot} at $y = 0$ for reference.

In general, we find a smaller spread in radial velocities for the MHD case as the magnetic field seems to restrict the most extreme motions of the gas. We see that velocities are, on average, ≈ 10 km s^{-1} lower than those found in the Hydro Rot run. We can also see how the MHD Rot halo progresses towards hotter temperatures, leading to a difference in the cooling that develops at late times. Both runs develop cool, typically dense outflowing gas structures that originate from the central region at 9 Gyrs, albeit more pronounced in the MHD Rot case. This is due to the combination of turbulent driving, which is the only source of feedback in these simulations, and angular momentum transfer which helps to expel cool gas from the central region.

Figure 4.12 shows ion-weighted projections of the line-of-sight velocities for these runs, illustrating how the MHD influences the motions of commonly-observed ions. From the face-on perspective shown in this plot, we do not have to consider the overall co-rotation velocity component. Here we find the hot component tracing the ambient medium to be largely static, with low line-of-sight velocities near zero while the gas within cooling structures traces the fastest moving material. In particular, the low and intermediate ions, Mg II and Si IV, show the largest line-of-sight velocities, approaching ± 200 km s^{-1} in the dense cores of cooling structures while the high ion phase, as traced by O VI, shows smaller velocities overall. The kinematics of the gas is a combination of turbulent motions from the consistent driving, thermal motions

99
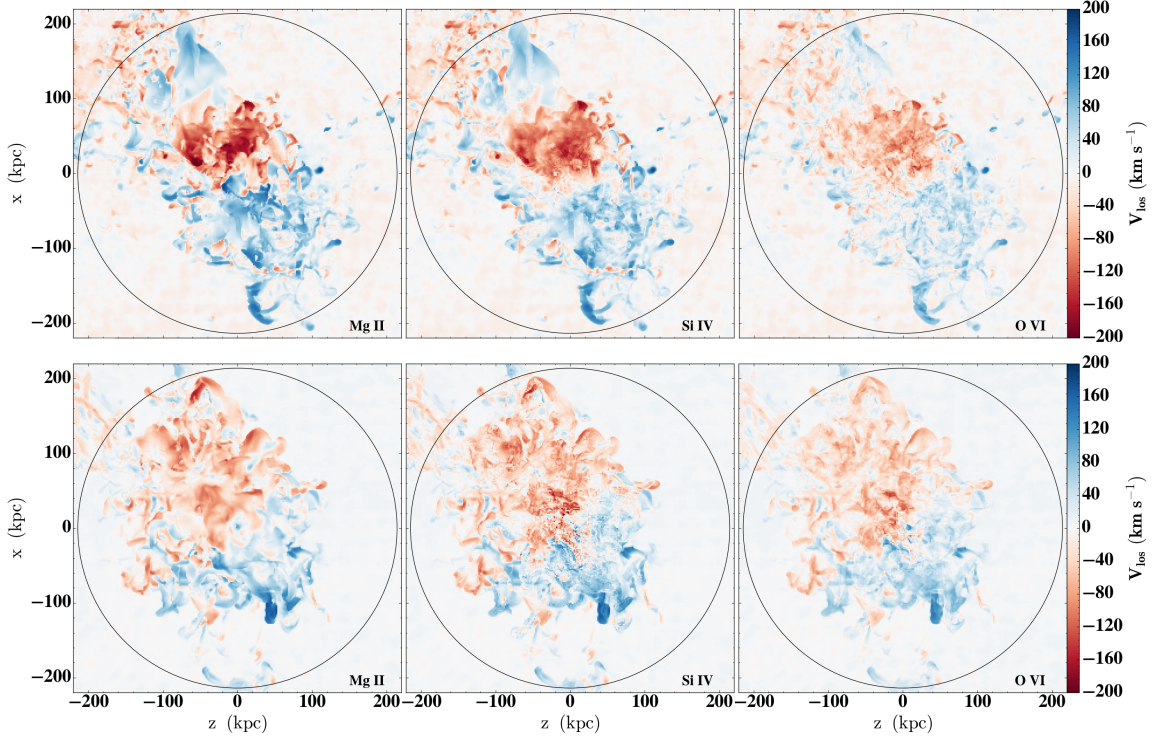
Figure 4.12: Mg II (left), Si IV (middle), and O VI (right) weighted line-of-sight velocity projections for the Hydro Rot (top) and MHD Rot (bottom) runs. Projections are from a face-on perspective at 9 Gyrs. A black circle shows the virial radius at $R_{\mathrm{vir}} \approx 220$ kpc.

from its inherent temperature, and motions due to the gas residing in a gravitational potential.

In B20, inhomogeneous turbulent stirring was made to be strongest near the center to mimic the star-forming galaxy environment with the majority of its feedback resulting from the center, as well as the impact of gas accreted from the intergalactic medium, which is likely to deposit the most energy per unit volume near the center of the halo. This stirring profile promoted a convective flow as hot material was driven to distant radii and replaced by gas condensing out of the ambient halo. When lower degrees of stirring were tested, gas simply collapsed towards the center with very limited mixing between the cold and hot components.

In this study, however, co-rotation provides a natural mechanism for distributing

gas and promoting interactions between cold and hot material. Therefore, a change in the amount of turbulent stirring, or in its radial profile by adjusting α in Equation 4.2, may lead to different features arising. In the case of stronger stirring, one may observe more outflows and possibly more gas that has been collisionally ionized in the central region, while less stirring may result in less of these. In the case of inhomogeneous stirring that instead increased with radius, one might observe slightly hotter distant ambient gas, as the turbulence would eventually dissipate its energy as heat, along with an increased level of variance in densities found in the outer regions (which may produce changes in the resulting ion column densities in these regions). These considerations may be explored in a future study.

Although not shown here, we find gas moving at faster velocities in the MHD case as compared to the hydrodynamic case when the halos are projected through from an edge-on perspective. It may be the case that magnetic fields help to move gas through the central, $y = 0$, plane which results in faster motions of this gas.

Moreover, we find the fastest moving clouds also have $t_{\rm cool}/t_{\rm ff}$ ratios $\lesssim 10^{-1}$ meaning they are cooling at least 10x faster than they are falling, which could potentially lead to star formation in their cores (e.g. Turner *et al.*, 2015). These simulations do not consider star formation (and have a maximum resolution of 1.6 kpc), however this may have implications higher resolution simulation that do consider the formation of star clusters.

To further examine the similarities and differences between the cooling structures found in these two runs, we include the projected column density maps for H I at 9 Gyrs from both the face-on and edge-on perspectives in Figure 4.13. Again, 9 Gyrs is a point in the evolution that is characterized by large-scale, fairly dense outflowing and inflowing gas clouds and filaments. We see that there are less cool clouds distributed throughout the MHD Rot run's CGM as compared to the hydrodynamic case.
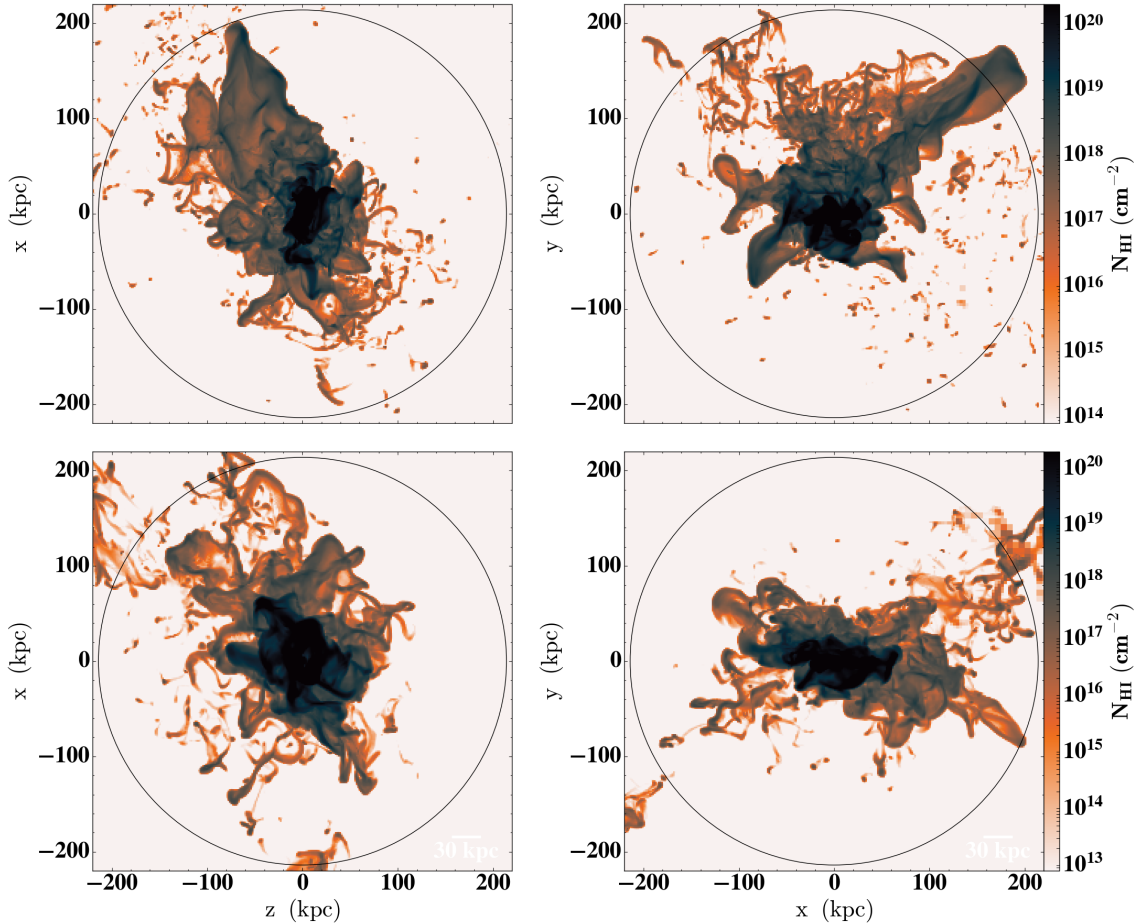
Figure 4.13: H I column density maps for the Hydro Rot (top) and MHD Rot (bottom) runs at 9 Gyrs. Projections through the halo from face-on and edge-on perspectives are shown in the left and right columns respectively. A black circle shows the virial radius at $R_{\rm vir} \approx 220$ kpc.

The smaller amount of cool clouds dispersed throughout the MHD halo may be a consequence of evaporation as the surrounding medium is hotter in this run as compared to the Hydro case. Furthermore, it has been shown that magnetic fields do not significantly increase the lifetime of cool clouds due to compression (in the case of tranverse fields) or the development of cloud tails (in the case of aligned fields), both of which promote mixing with the ambient medium (Cottle *et al.*, 2020). As both simulations evolve, we find an increasing lower limit of H 1 columns as well as a covering fraction of 100% for H I, both seen within ≈ 50 kpc.

This high covering fraction is most likely a consequence of the idealized nature of our simulations as the amount of cool gas near the central region continues to build without additional ionizing sources of feedback, such as a star-forming UV background, AGN feedback, or cosmic rays. Also, our simulations do not consider radiative transfer, which would provide additional means for heating and possibly ionization. These relevant radiative backgrounds (i.e. star-forming UV background, AGN feedback, or cosmic rays) would provide additional heating to the central region of both halos, likely reducing some of the cooling that takes place in the central region, and even ionizing some of the dense H I that accumulates there.

In Figure 4.14, we show the Si IV/O VI and N V/O VI ratios for the MHD Rot run at 9 Gyrs and a single-zone CLOUDY model for reference. Although we do not show these ion ratios for the Hydro case, we find that both of the run's ion ratios look very similar to what is shown. Moreover, these ion ratios do not change shape throughout the 9 Gyr evolution, except for being slightly less dispersed at earlier times. In the MHD case, gas with Si IV/O VI ratios $\gtrsim 1$ has temperatures $\lesssim 40{,}000$ K and β values $\lesssim 1$, whereas this gas has no magnetic pressure support in the hydrodynamic case.

We also performed a cut on the data to see whether the ratios change considerably if we consider "realistic" outer CGM observations, i.e. those with O VI column densities above 10^{13} cm^{-2}. We assumed a path length of 100 kpc to obtain a conservative lower limit on $n_{\rm OVI}$ of 3×10^{-11} cm^{-3}. This cut essentially removes the most diffuse ambient halo gas that would be unlikely to be observed in the spectra of background quasars. The removal of this gas, however, does not alter the overall shape of these distributions.

The majority of COS-Halos detections and limits presented in Figure 12 of Werk et al. (2016) have Si IV/O VI $\lesssim 10^{-1}$ N V/O VI $\lesssim 10^{-1}$. While these are difficult to explain from equilibrium models, they naturally correspond to gas with T between
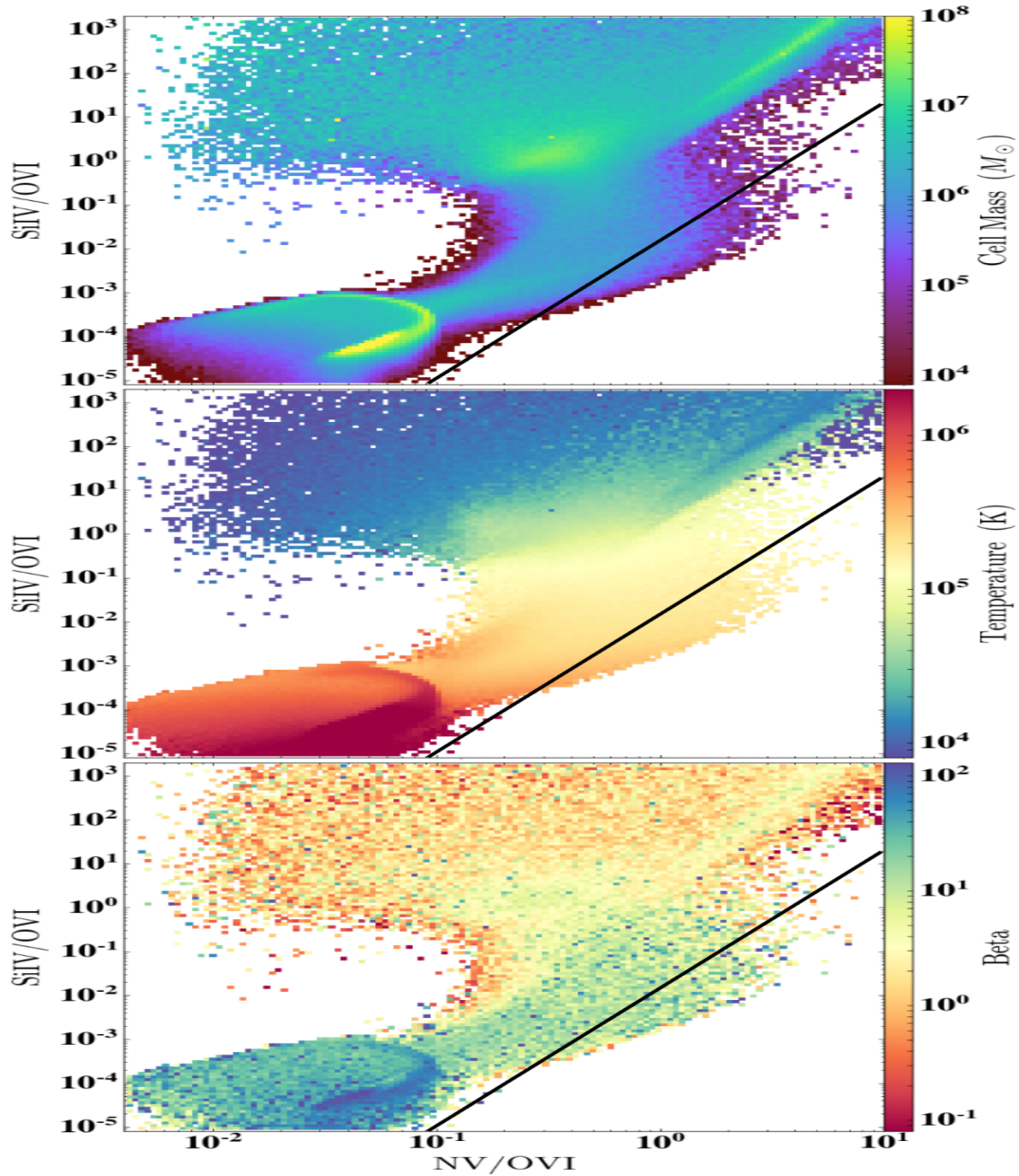
Figure 4.14: Panels showing the Si IV/O VI vs. N V/O VI ratios with the total mass in a bin (top), mass-weighted average temperature (middle), and mass-weighted average β from the MHD Rot run at 9 Gyrs. These are made using 128 bins for the x and y quantities. The black line shows a single-zone Cloudy model at 30% solar metallicity photoionized by a redshift zero HM2012 EUVB with $-4 < log\ U < -1$ as a reference. This range in U spans hydrogen densitites between 10^{-1} and 10^{-6} and yields temperatures between 10^{4-5}. COS-Halos detections and limits from Werk *et al.* (2016) would be located in the $T = 10^{5-6}$ K region of these plots.
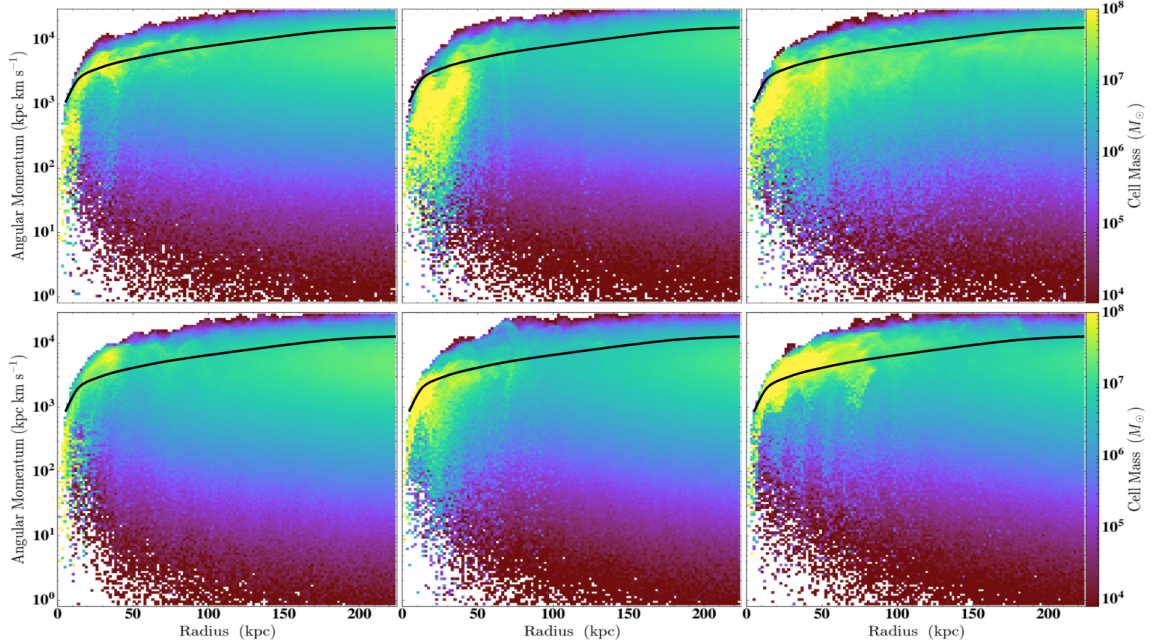
Figure 4.15: Distribution of CGM mass as a function of radius and angular momentum per unit mass, for the Hydro Rot (top) and MHD Rot (bottom) runs at 3 (left), 6 (middle), and 9 (right) Gyrs. These are made using 128 bins for the x and y quantities. For reference, we include a solid black line to show the specific angular momentum profile for Keplerian orbit.

10^{5-6} K in our simulations. In the MHD Rot run, this region of parameter space also houses gas with β's $\lesssim 1$, meaning some of these systems could trace gas in which the dominant pressure is magnetic.

In Figure 4.15, we show the distribution of CGM mass as a function of radius and angular momentum per unit mass (otherwise known as the specific angular momentum). We further show a Keplerian specific angular momentum profile for comparison, which we will denote as L_{Kep}. At 3 Gyrs, we find that the majority of the mass in the inner 50 kpc of the Hydro Rot halo lies along L_{Kep} and the majority of this mass in the MHD case is above the Keplerian profile. Such gas is under the influence of turbulent stirring along with co-rotation and this difference indicates larger velocities in the gas residing in the inner halo of the MHD run. This higher angular momentum gas is found near the plane of the central disk structure, centered at $y = 0$. At 6 Gyrs,

we observe the majority of the mass in the inner 50 kpc has decreased in specific angular momentum in both runs. Being that the mass does not seem to have moved to larger distances, this may indicate a decrease in associated velocities. The mass in this inner region of the MHD halo lies along L_{Kep}, while the mass in this same region of the Hydro Rot lies below it.

At 9 Gyrs, however, the velocities of the majority of the mass within 100 kpc increase again. At this time, the majority of mass in this inner region lies closer to L_{Kep} in the Hydro case and at or above the Keplerian profiles in the MHD case, indicating that it has been spun up at this later time in its evolution. Thus, it may be inferred that most of the mass within 100 kpc in the hydrodynamic case is traveling at smaller velocities as compared to the gas in the MHD central disk-like structure. Again, gas with the highest specific angular momentum is found along the plane of rotation at $y = 0$. We can also see this from the last two rows in Figure 4.1 which shows that in both of our runs the densest ($n \gtrsim 10^{-2}$ cm^{-3}) material containing most of the mass in the inner ≈ 100 kpc region lies within ± 50 kpc of $y = 0$.

Being that this dense gas also houses the largest magnetic fields, it is likely that the magnetic fields help to facilitate this transfer of angular momentum throughout the cold gas. This transfer of angular momentum in the MHD case, occurs between 6 - 8 Gyrs, and is likely caused by the combination of large outflows of $v_{\mathrm{r}} \gtrsim 100$ km $^{-1}$ material along with infalling condensate from the ambient medium that occurs predominantly along the central disk plane centered at $y = 0$.

Finally, we note that Hodges-Kluck *et al.* (2016) found a spherically rotating model, rather than the thick disk model model adopted here, provided a good match to the observations of O VII absorption lines in the Milky Way halo. Adopting such a model would result in a slightly higher total angular momentum of the system, requiring a smaller f_{rot} in Equation 4.3 to obtain a λ near 0.03 for our halo. We

speculate that spherical rotation may result in slight changes to the mixing and eventual cooling of hot gas, more so in the gas at the outer regions of the halo. However it is unlikely that these would lead to substantial changes in the structures, column densities, and other properties, especially since the scale heights of disk models that were compared to a spherical rotational model in Hodges-Kluck *et al.* (2016) were on the order of a few kpc, rather than the 50 kpc adopted here.

4.4   Discussion and Summary

In this work, we describe the first simulation of the evolution of a magnetized Milky Way-like galactic halo that includes full non-equilibrium chemistry, rotation, and turbulence. Our idealized setup allows us to directly contrast this simulation with a hydrodynamic case in and draw conclusions on the impact of magnetic fields on the state multiphase CGM and its observational properties.

The addition of a co-rotational component enhances the mixing of hot and cold gas in both simulations, which leads to increased cooling. Halos in both simulations lose $\approx 14\%$ of their total baryonic mass due to the initial accretion shock and turbulent motions. At about 4 and 6 Gyrs for in the Hydro and MHD Rot runs respectively, mass begins to be ejected from the central 12 kpc region out into the CGM. The MHD halo also continues to lose mass from the ambient medium for the remainder of its evolution, leading to a somewhat less dense and hotter medium than in the hydrodynamic case.

One consequence of the MHD Rot halo forming a hotter, more diffuse CGM, is that the gas above and below the extended disk attains longer cooling times with $t_{\mathrm{cool}}/t_{\mathrm{ff}}$ ratios > 100 by 9 Gyrs. Without MHD, gas is able to cool at more distant radii, which lowers the maximum $t_{\mathrm{cool}}/t_{\mathrm{ff}}$ ratios of extraplanar gas to < 100 as the densities in these regions increase. Both halos, however, develop bimodal $t_{\mathrm{cool}}/t_{\mathrm{ff}}$

distributions where one phase traces the hot component with $1 < t_{\rm cool}/t_{\rm ff} < 100$, and the other traces cold, dense gas with $10^{-4} < t_{\rm cool}/t_{\rm ff} < 10^{-1}$.

When examining the entropy-pressure phase space of our runs, we find that the MHD ambient medium rises to greater entropy throughout its evolution. Due to expansion, some of the lower entropy gas is able to cool below our temperature floor at 5000 K, the temperature below which radiative cooling is dominated by molecules, which are not included in our chemical network. We find that the MHD run keeps more gas above this temperature limit, and by 9 Gyrs, this case leads to a restriction in the pressure phase space of the intermediate, $T \approx 10^5$ K, gas to a narrower range as compared to the Hydro Rot run. Finally, gas in the MHD Rot run with $K \lesssim 1\,{\rm cm^2\,keV}$ also possess low β values that indicate significant magnetic pressure support.

We find ambient halo B-field strengths saturate to $\approx 0.1\,\mu$G in the 9 Gyr evolution, back to the initial seed field strength. We also find higher strengths $\lesssim 10\,\mu$G in denser structures that form in the inner halo. These denser structures typically show B-field lines that are oriented parallel to their surfaces, which may be an indication of magnetic draping that has become dynamically important. The presence of a magnetic field also helps enable the transfer of angular momentum throughout the cold gas. In the MHD case, we find a slightly more extended disk-like structure that forms in the central region and moves with faster velocities as compared to the hydrodynamic case in the later stages of evolution. This may also help to maintain the extended disk-like structure at late times as nearby gas outside of it interacts with it and gains angular momentum thereby keeping the nearby cooling and heating gas constrained to the disk plane.

Kinematically, we find that magnetic fields, overall, inhibits the radial motions of gas, with the MHD run showing a slightly smaller dispersion in radial velocities throughout its evolution. We find that dense structures showing outflowing and

inflowing material, and the ions associated with them, are moving the fastest, at v_r upwards $\pm\,200$ km s^{-1} in the Hydro Rot case. This material is observed to be moving somewhat slower in the MHD case when viewed from a face-on perspective. In both runs, it is the low, singly-ionized states, such as Mg II found in the densest cores of the outflowing and inflowing gas, that typically possess the largest line of sight velocities, whereas the highest ionization states, such as O VI, move the slowest.

When looking at the Si IV/O VI and N V/O VI ratios, we find very little difference between these runs, and furthermore, throughout their 9 Gyr evolution. One difference is that in the MHD Rot run, gas with Si IV/O VI $\gtrsim 1$ finds itself comparable or greater magnetic pressure support.

Future work may include an expansion on our chemistry network to include dynamically relevant molecular cooling processes, as well as higher resolution to better resolve the densest structures that develop. This may also include varying the initial magnetic field strength to achieve higher β's at initialization to observe how this may influence the saturation of the magnetic field.

Moreover, we may investigate different turbulent feedback prescriptions (changing α in Equation 4.2) to see if varying initial turbulent driving leads to very different results. Finally, including an additional star forming background in the inner CGM will allow us to gain a better understanding of how this radiative feedback would influence the large column densities that form around the central galaxy.

4.5   Entropy Radial Profile

In this section we show the radial profile of entropy as a function of total mass for the Hydro and MHD Rot runs. These are shown so the reader may see where the majority of the mass lies and that the ambient medium is isentropic. Buoyancy therefore is unable to inhibit the progression of thermal instability into multiphase condensa-

tion. The centralized turbulent stirring creates a convective flow that progressively heats the entire atmosphere, facilitating the creation of the isentropic profile.
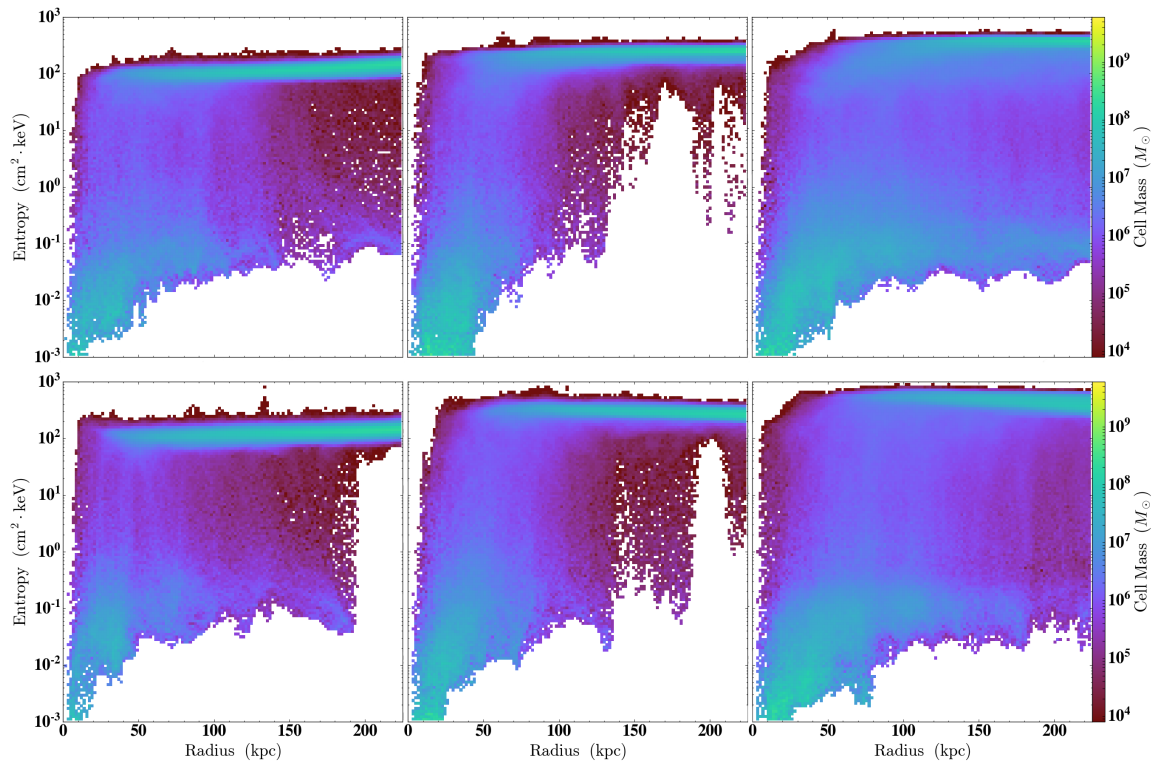

Figure 4.16: Entropy vs. radius showing the total mass in a bin for the Hydro Rot (top) and MHD Rot (bottom) runs. We specifically show these at 3 (left), 6 (middle), and 9 (right) Gyrs. Plots are made using 128 bins for the x and y quantities.

Chapter 5

CONCLUSION

This work presents the culmination of modeling focused on the evolution of non-equilibrium chemistry in a turbulent circumgalactic medium. Most observations of this medium can only provide information on single sightlines while numerical modeling helps us fully understand its state by following the time and spatial evolution of the gas. This gaseous halo is influenced by many feedback mechansims that can drive the observed turbulence seen in absorption lines of ions. When modeled, such turbulence promotes mixing between cold gas and the hot ambient medium, resulting in intermediate states that are in better agreement with observational findings as compared to those found in equilibrium models.

The first attempt at simulating the non-equilibrium chemical evolution that occurs in this turbulent environment was constrained to isochoric domains and considered homogeneous stirring. Such simulations probed a range of turbulent velocities commonly observed in the CGM, producing density and temperature gradients spanning 2 orders of magnitude and the full range of ionization states observed. Low ions typically congregated in clumps while being surrounded by the hotter ambient medium. Furthermore, while O VI could be produced at lower densities, and consequently lower ionization parameters, it often arose with comparable amounts of N V. This finding showed that homogeneous turbulence in these column density analogues was not enough to match the observations of the CGM surrounding star-forming galaxies.

The next suite of simulations built on this foundation by considering the full halo, and tested varying degrees of inhomogeneous turbulent stirring strengths. As theorized, this setup allowed for a natural cooling path towards the center which removed

the possibility of overheating to unphysical temperatures, an issue encountered in the previous set of simulations. Only the run with an average σ_{1D} of 41 km s^{-1}, corresponding to a turbulent energy injection rate of 4×10^{49} erg yr^{-1}, developed a convective flow where hot gas bouyantly rose to be replaced by cooler, inflowing gas that also yielded projected column densities that matched those inferred from observations at large radial distances from the central galaxy. All of the runs, regardless of turbulent stirring, produced Si IV/O VI and N V/O VI ratios that agreed with the observed ion ratios. This seemed to show that such ion ratios primarily result from the density gradient that promotes gas which is able to cool on shorter timescales than what was found in the previous isochoric simulations.

To bring the simulations closer to reality, we further included a co-rotating halo while delving into the similarities and differences between the hydrodynamic and magneto-hydrodynamic evolution of a Milky Way-like CGM. Rotation led to enhanced cooling while the magneto-hydrodynamic run showed additional mass loss throughout its evolution, resulting in a hotter and more diffuse ambient medium as compared to the hydrodynamic case. Gas in this hotter ambient medium also found itself with larger cooling times, pressure, and entropy. These differences, however, did not alter the ion ratios found between both halos, although those in the MHD case that traced 10^{4-5} K gas were equally, if not more, supported by magnetic pressure as opposed to thermal pressure. Magnetic field lines were also found to orient themselves parallel to dense structures which may have enabled magnetic draping to become relevant, inhibiting mixing between the dense and diffuse gas. The magnetic field also played a role in transferring angular momentum throughout the colder gas as it was able to maintain a central disk structure at late times while the hydrodynamic run produced cooling and heating gas that was found beyond the disk plane.

Observations of the multiphase CGM gas gives information on its temperature,

density, and velocity structure, however models that simulate this non-equilibrium chemistry are needed to gain a more complete understanding of the CGM and its evolution. Moreover, idealized simulations that consider a few of the relevant physics and dynamics are able to isolate their influences on ionized elements. While this work has examined many physical processes (turbulence, co-rotation, magnetic fields, etc.), actual CGM environments have additional physics that should be studied to reveal their influence on the multiphase gas evolution as well as gauge their importance in determining the ionized states observed. Such relevant physics include cosmic rays, central star-forming UV backgrounds, molecular cooling channels for dense clouds, radiation transfer, and more. Furthermore, the inclusion of a co-rotating halo was shown to enable mixing between hot and cold gas, and thus varying the turbulent feedback and strength should be tested to gauge its impact on the multiphase features.

The CGM is the interface that connects galaxies to the entended intergalactic medium and serves as the reservoir for interactions amoungst baryons through recycling processes. Outflows transfer mass, metals, energy, and momentum to the ambient material where it may mix, cool, and eventually flow back into the central galaxy where it may be processed into new stars. There is still much to be learned about the dynamics and their specific influences on the cooling and heating that occurs within this environment. The continuous advancement of models adds to the knowledge of its physical state, and we hope this work contributes to that endeavor.

REFERENCES

Aghanim, N., Y. Akrami, M. Ashdown, J. Aumont, C. Baccigalupi, M. Ballardini, A. Banday, R. Barreiro, N. Bartolo, S. Basak *et al.*, "Planck 2018 results. vi. cosmological parameters", arXiv preprint arXiv:1807.06209 (2018).

Aldrovandi, S. and D. Pequignot, "Radiative and dielectronic recombination coefficients for complex ions", A&A **25**, 137 (1973).

Allen, M. G., B. A. Groves, M. A. Dopita, R. S. Sutherland and L. J. Kewley, "The MAPPINGS III Library of Fast Radiative Shock Models", ApJS **178**, 1, 20–55 (2008).

Arnaud, M. and R. Rothenflug, "An updated evaluation of recombination and ionization rates", Astronomy and Astrophysics Supplement Series **60**, 425–457 (1985).

Artale, M. C., I. Zehavi, S. Contreras and P. Norberg, "The impact of assembly bias on the halo occupation in hydrodynamical simulations", MNRAS **480**, 3, 3978–3992 (2018).

Bahcall, J. N., "A Systematic Method for Identifying Absorption Lines as Applied to PKS 0237-23", ApJ **153**, 679 (1968).

Bahcall, J. N., J. Bergeron, A. Boksenberg, G. F. Hartig, B. T. Jannuzi, S. Kirhakos, W. L. W. Sargent, B. D. Savage, D. P. Schneider, D. A. Turnshek, R. J. Weymann and A. M. Wolfe, "The Hubble Space Telescope Quasar Absorption Line Key Project. I. First Observational Results, Including Lyman-Alpha and Lyman-Limit Systems", ApJS **87**, 1 (1993).

Bahcall, J. N., J. Bergeron, A. Boksenberg, G. F. Hartig, B. T. Jannuzi, S. Kirhakos, W. L. W. Sargent, B. D. Savage, D. P. Schneider, D. A. Turnshek, R. J. Weymann and A. M. Wolfe, "The Hubble Space Telescope Quasar Absorption Line Key Project. VII. Absorption Systems at Z abs ¡= 1.3", ApJ **457**, 19 (1996).

Bahcall, J. N., J. L. Greenstein and W. L. W. Sargent, "The Absorption-Line Spectrum of the Quasi-Stellar Radio Source PKS 0237-23", ApJ **153**, 689 (1968).

Bahcall, J. N. and J. Spitzer, Lyman, "Absorption Lines Produced by Galactic Halos", ApJ **156**, L63 (1969).

Beck, A. M., H. Lesch, K. Dolag, H. Kotarba, A. Geng and F. A. Stasyszyn, "Origin of strong magnetic fields in Milky Way-like galactic haloes", MNRAS **422**, 3, 2152–2163 (2012).

Begelman, M. C. and A. C. Fabian, "Turbulent mixing layers in the interstellar and intracluster medium.", MNRAS **244**, 26P–29 (1990).

Benjamin, R. A., *The Origin and Evolution of Galactic Halo Gas.*, Ph.D. thesis, University of Texas at Austin, United States (1994).

Bergeron, J. and G. Stasińska, "Absorption line systems in QSO spectra : properties derived from observations and from photoionization models.", A&A **169**, 1–3 (1986).

Bernet, M. L., F. Miniati and S. J. Lilly, "Mg II Absorption Systems with W $_0$ ¿= 0.1 Å for a Radio Selected Sample of 77 Quasi-Stellar Objects and their Associated Magnetic Fields at High Redshift", ApJ **711**, 1, 380–388 (2010).

Bernet, M. L., F. Miniati and S. J. Lilly, "The Interpretation of Rotation Measures in the Presence of Inhomogeneous Foreground Screens", ApJ **761**, 2, 144 (2012).

Bernet, M. L., F. Miniati, S. J. Lilly, P. P. Kronberg and M. Dessauges-Zavadsky, "Strong magnetic fields in normal galaxies at high redshift", Nature **454**, 7202, 302–304 (2008).

Birnboim, Y. and A. Dekel, "Virial shocks in galactic haloes?", MNRAS **345**, 1, 349–364 (2003).

Bordoloi, R., J. X. Prochaska, J. Tumlinson, J. K. Werk, T. M. Tripp and J. N. Burchett, "On the CGM Fundamental Plane: The Halo Mass Dependency of Circumgalactic H I", ApJ **864**, 2, 132 (2018).

Bordoloi, R., J. Tumlinson, J. K. Werk, B. D. Oppenheimer, M. S. Peeples, J. X. Prochaska, T. M. Tripp, N. Katz, R. Davé, A. J. Fox, C. Thom, A. B. Ford, D. H. Weinberg, J. N. Burchett and J. A. Kollmeier, "The COS-Dwarfs Survey: The Carbon Reservoir around Sub-L* Galaxies", ApJ **796**, 2, 136 (2014).

Borkowski, K. J., S. A. Balbus and C. C. Fristrom, "Radiative Magnetized Thermal Conduction Fronts", ApJ **355**, 501 (1990).

Borthakur, S., T. Heckman, J. Tumlinson, R. Bordoloi, G. Kauffmann, B. Catinella, D. Schiminovich, R. Davé, S. M. Moran and A. Saintonge, "The Properties of the Circumgalactic Medium in Red and Blue Galaxies: Results from the COS-GASS+COS-Halos Surveys", ApJ **833**, 2, 259 (2016).

Bowen, D. V., D. Chelouche, E. B. Jenkins, T. M. Tripp, M. Pettini, D. G. York and B. L. Frye, "The structure of the circumgalactic medium of galaxies: cool accretion inflow around ngc 1097", The Astrophysical Journal **826**, 1, 50 (2016).

Boylan-Kolchin, M., C.-P. Ma and E. Quataert, "Dynamical friction and galaxy merging time-scales", Monthly Notices of the Royal Astronomical Society **383**, 1, 93–101 (2008).

Brandenburg, A., D. Sokoloff and K. Subramanian, "Current status of turbulent dynamo theory", Space Science Reviews **169**, 1-4, 123–157, URL http://dx.doi.org/10.1007/s11214-012-9909-x (2012).

Brooks, A., F. Governato, T. Quinn, C. Brook and J. Wadsley, "The role of cold flows in the assembly of galaxy disks", ApJ **694**, 1, 396 (2009).

Bryan, S. E., S. T. Kay, A. R. Duffy, J. Schaye, C. Dalla Vecchia and C. M. Booth, "The impact of baryons on the spins and shapes of dark matter haloes", MNRAS **429**, 4, 3316–3329 (2013).

Buie, E., II, W. J. Gray and E. Scannapieco, "Modeling photoionized turbulent material in the circumgalactic medium", The Astrophysical Journal **864**, 2, 114 (2018).

Buie, I., Edward, M. Fumagalli and E. Scannapieco, "Interpreting observations of absorption lines in the circumgalactic medium with a turbulent medium", The Astrophysical Journal **890**, 1, 33 (2020a).

Buie, I., Edward, W. J. Gray, E. Scannapieco and M. Safarzadeh, "Modeling Photoionized Turbulent Material in the Circumgalactic Medium. II. Effect of Turbulence within a Stratified Medium", ApJ **896**, 2, 136 (2020b).

Buie II, E., W. J. Gray and E. Scannapieco, "Modeling photoionized turbulent material in the circumgalactic medium", The Astrophysical Journal **864**, 2, 114, URL `http://dx.doi.org/10.3847/1538-4357/aad8bd` (2018).

Bullock, J. S., A. Dekel, T. S. Kolatt, A. V. Kravtsov, A. A. Klypin, C. Porciani and J. R. Primack, "A Universal Angular Momentum Profile for Galactic Halos", ApJ **555**, 1, 240–257 (2001).

Burbidge, E. M., "Absorption Redshifts in the Quasi-Stellar Objects PHL 5200 and B 194", ApJ **155**, L43 (1969).

Burbidge, E. M., C. R. Lynds and A. N. Stockton, "Erratum: Further Observations of Quasi-Stellar Objects with Absorption-Line Spectra: Ton 1530, PKS 0237-23, and PHL 938", ApJ **153**, 703 (1968).

Cantalupo, S., F. Arrigoni-Battaia, J. X. Prochaska, J. F. Hennawi and P. Madau, "A cosmic web filament revealed in lyman-α emission around a luminous high-redshift quasar", Nature **506**, 7486, 63–66 (2014).

Cen, R., K. Nagamine and J. P. Ostriker, "Quantitative Signatures of Galactic Superwinds on Lyα Clouds and Metal-Line Systems", ApJ **635**, 1, 86–99 (2005).

Chandrasekhar, S., "Dynamical Friction. I. General Considerations: the Coefficient of Dynamical Friction.", ApJ **97**, 255 (1943).

Chen, H.-W., K. M. Lanzetta and J. K. Webb, "The Origin of C IV Absorption Systems at Redshifts z < 1: Discovery of Extended C IV Envelopes around Galaxies", ApJ **556**, 1, 158–163 (2001a).

Chen, H.-W., K. M. Lanzetta, J. K. Webb and X. Barcons, "The Gaseous Extent of Galaxies and the Origin of Lyα Absorption Systems. III. Hubble Space Telescope Imaging of Lyα-absorbing Galaxies at z < 1", ApJ **498**, 1, 77–94 (1998).

Chen, H.-W., K. M. Lanzetta, J. K. Webb and X. Barcons, "The Gaseous Extent of Galaxies and the Origin of Lyα Absorption Systems. V. Optical and Near-Infrared Photometry of Lyα-absorbing Galaxies at z¡1", ApJ **559**, 2, 654–674 (2001b).

Chen, H.-W., K. M. Lanzetta, J. K. Webb and X. Barcons, "The Gaseous Extent of Galaxies and the Origin of Lyα Absorption Systems. V. Optical and Near-Infrared Photometry of Lyα-absorbing Galaxies at z<1", ApJ **559**, 2, 654–674 (2001c).

Chen, H.-W., F. S. Zahedy, S. D. Johnson, R. M. Pierce, Y.-H. Huang, B. J. Weiner and J.-R. Gauthier, "Characterizing circumgalactic gas around massive ellipticals at z $\sim$ 0.4 - I. Initial results", MNRAS **479**, 2, 2547–2563 (2018).

Choudhury, P. P., P. Sharma and E. Quataert, "Multiphase gas in the circumgalactic medium: relative role of t_{cool}/t_{ff} and density fluctuations", MNRAS **488**, 3, 3195–3210 (2019).

Churazov, E., W. Forman, C. Jones, R. Sunyaev and H. Böhringer, "XMM-Newton observations of the Perseus cluster - II. Evidence for gas motions in the core", MNRAS **347**, 1, 29–35 (2004).

Churchill, C. W., J. R. Vander Vliet, S. Trujillo-Gomez, G. G. Kacprzak and A. Klypin, "Direct insights into observational absorption line analysis methods of the circumgalactic medium using cosmological simulations", The Astrophysical Journal **802**, 1, 10 (2015).

Correa, C. A., J. Schaye, J. S. B. Wyithe, A. R. Duffy, T. Theuns, R. A. Crain and R. G. Bower, "The formation of hot gaseous haloes around galaxies", MNRAS **473**, 1, 538–559 (2018).

Cottle, J., E. Scannapieco, M. Brüggen, W. Banda-Barragán and C. Federrath, "The Launching of Cold Clouds by Galaxy Outflows. III. The Influence of Magnetic Fields", ApJ **892**, 1, 59 (2020).

Crighton, N. H. M., J. F. Hennawi, R. A. Simcoe, K. L. Cooksey, M. T. Murphy, M. Fumagalli, J. X. Prochaska and T. Shanks, "Metal-enriched, subkiloparsec gas clumps in the circumgalactic medium of a faint z = 2.5 galaxy", MNRAS **446**, 18–37 (2015).

Dekel, A. and Y. Birnboim, "Galaxy bimodality due to cold flows and shock heating", MNRAS **368**, 1, 2–20 (2006).

Dolag, K., S. Borgani, G. Murante and V. Springel, "Substructures in hydrodynamical cluster simulations", MNRAS **399**, 2, 497–514 (2009).

Dopita, M. A. and R. S. Sutherland, "Spectral Signatures of Fast Shocks. I. Low-Density Model Grid", ApJS **102**, 161 (1996).

Dursi, L. J. and C. Pfrommer, "Draping of Cluster Magnetic Fields over Bullets and Bubbles—Morphology and Dynamic Effects", ApJ **677**, 2, 993–1018 (2008).

Eckert, D., V. Ghirardini, S. Ettori, E. Rasia, V. Biffi, E. Pointecouteau, M. Rossetti, S. Molendi, F. Vazza, F. Gastaldello, M. Gaspari, S. De Grandi, S. Ghizzardi, H. Bourdin, C. Tchernin and M. Roncarelli, "Non-thermal pressure support in X-COP galaxy clusters", A&A **621**, A40 (2019).

Edgar, R. J. and R. A. Chevalier, "Highly Ionized Atoms in Cooling Gas", ApJ **310**, L27 (1986).

Einfeldt, B., C.-D. Munz, P. L. Roe and B. Sjögreen, "On godunov-type methods near low densities", Journal of computational physics **92**, 2, 273–295 (1991).

Esmerian, C. J., A. V. Kravtsov, Z. Hafen, C.-A. Faucher-Giguère, E. Quataert, J. Stern, D. Kereš and A. Wetzel, "Thermal instability in the CGM of L$_\star$ galaxies: testing 'precipitation' models with the FIRE simulations", MNRAS **505**, 2, 1841–1862 (2021).

Faerman, Y., A. Sternberg and C. F. McKee, "Massive Warm/Hot Galaxy Coronae as Probed by UV/X-Ray Oxygen Absorption and Emission. I. Basic Model", ApJ **835**, 1, 52 (2017).

Farnes, J. S., S. P. O'Sullivan, M. E. Corrigan and B. M. Gaensler, "Faraday Rotation from Magnesium II Absorbers toward Polarized Background Radio Sources", ApJ **795**, 1, 63 (2014).

Faucher-Giguère, C.-A. and D. Kereš, "The small covering factor of cold accretion streams", MNRAS **412**, 1, L118–L122 (2011).

Ferland, G. J., M. Chatzikos, F. Guzmán, M. L. Lykins, P. A. M. van Hoof, R. J. R. Williams, N. P. Abel, N. R. Badnell, F. P. Keenan, R. L. Porter and P. C. Stancil, "The 2017 Release Cloudy", RMxAA**53**, 385–438 (2017).

Ferland, G. J., R. L. Porter, P. A. M. van Hoof, R. J. R. Williams, N. P. Abel, M. L. Lykins, G. Shaw, W. J. Henney and P. C. Stancil, "The 2013 Release of Cloudy", RMxAA**49**, 137–163 (2013).

Field, G. B., "Thermal Instability.", ApJ **142**, 531 (1965).

Fielding, D., E. Quataert, M. McCourt and T. A. Thompson, "The impact of star formation feedback on the circumgalactic medium", Monthly Notices of the Royal Astronomical Society **466**, 4, 3810–3826 (2017).

Ford, A. B., R. Davé, B. D. Oppenheimer, N. Katz, J. A. Kollmeier, R. Thompson and D. H. Weinberg, "Tracing inflows and outflows with absorption lines in circumgalactic gas", MNRAS **444**, 2, 1260–1281 (2014).

Ford, A. B., J. K. Werk, R. Davé, J. Tumlinson, R. Bordoloi, N. Katz, J. A. Kollmeier, B. D. Oppenheimer, M. S. Peeples, J. X. Prochaska and D. H. Weinberg, "Baryon cycling in the low-redshift circumgalactic medium: a comparison of simulations to the COS-Halos survey", MNRAS **459**, 1745–1763 (2016).

Fox, A. and R. Davé, *Gas Accretion Onto Galaxies*, vol. 430 (Berlin: Springer, 2017).

Fox, A. J., R. Bordoloi, B. D. Savage, F. J. Lockman, E. B. Jenkins, B. P. Wakker, J. Bland-Hawthorn, S. Hernandez, T.-S. Kim, R. A. Benjamin *et al.*, "Probing the fermi bubbles in ultraviolet absorption: A spectroscopic signature of the milky way's biconical nuclear outflow", The Astrophysical Journal Letters **799**, 1, L7 (2015).

Fryxell, B., K. Olson, P. Ricker, F. Timmes, M. Zingale, D. Lamb, P. MacNeice, R. Rosner, J. Truran and H. Tufo, "Flash: An adaptive mesh hydrodynamics code for modeling astrophysical thermonuclear flashes", ApJ **131**, 1, 273 (2000).

Gaspari, M., F. Brighenti and P. Temi, "Mechanical agn feedback: controlling the thermodynamical evolution of elliptical galaxies", Monthly Notices of the Royal Astronomical Society **424**, 1, 190–209 (2012).

Gaspari, M. and E. Churazov, "Constraining turbulence and conduction in the hot ICM through density perturbations", A&A **559**, A78 (2013).

Gaspari, M., P. Temi and F. Brighenti, "Raining on black holes and massive galaxies: the top-down multiphase condensation model", MNRAS **466**, 1, 677–704 (2017).

Gilfanov, M. R., R. A. Syunyaev and E. M. Churazov, "Radial Brightness Profiles of Resonance X-Ray Lines in Galaxy Clusters", Soviet Astronomy Letters **13**, 3 (1987).

Gnat, O. and A. Sternberg, "Time-dependent Ionization in Radiatively Cooling Gas", ApJS **168**, 2, 213–230 (2007).

Gnat, O. and A. Sternberg, "Metal-Absorption Column Densities in Fast Radiative Shocks", ApJ **693**, 2, 1514–1542 (2009).

Gnat, O., A. Sternberg and C. F. McKee, "Metal-ion Absorption in Conductively Evaporating Clouds", ApJ **718**, 2, 1315–1331 (2010).

Gray, W. J. and E. Scannapieco, "Atomic chemistry in turbulent astrophysical media. ii. effect of the redshift zero metagalactic background", ApJ **818**, 2, 198 (2016).

Gray, W. J. and E. Scannapieco, "The Effect of Turbulence on Nebular Emission Line Ratios", ApJ **849**, 2, 132 (2017).

Gray, W. J., E. Scannapieco and D. Kasen, "Atomic chemistry in turbulent astrophysical media. i. effect of atomic cooling", ApJ **801**, 2, 107 (2015).

Gutcke, T. A., G. S. Stinson, A. V. Macciò, L. Wang and A. A. Dutton, "NIHAO - VIII. Circum-galactic medium and outflows - The puzzles of H I and O VI gas distributions", MNRAS **464**, 2796–2815 (2017).

Haardt, F. and P. Madau, "Radiative Transfer in a Clumpy Universe. IV. New Synthesis Models of the Cosmic UV/X-Ray Background", ApJ **746**, 2, 125 (2012).

Hani, M. H., M. Sparre, S. L. Ellison, P. Torrey and M. Vogelsberger, "Galaxy mergers moulding the circum-galactic medium - I. The impact of a major merger", MNRAS **475**, 1160–1176 (2018).

Heckman, T., S. Borthakur, V. Wild, D. Schiminovich and R. Bordoloi, "COS-burst: Observations of the Impact of Starburst-driven Winds on the Properties of the Circum-galactic Medium", ApJ **846**, 2, 151 (2017).

Heckman, T., S. Borthakur, V. Wild, D. Schiminovich and R. Bordoloi, "Cos-burst: Observations of the impact of starburst-driven winds on the properties of the circum-galactic medium", The Astrophysical Journal **846**, 2, 151 (2017).

Hitomi Collaboration, F. Aharonian, H. Akamatsu, F. Akimoto, S. W. Allen, N. Anabuki, L. Angelini, K. Arnaud, M. Audard, H. Awaki, M. Axelsson, A. Bamba, M. Bautz, R. Blandford, L. Brenneman, G. V. Brown, E. Bulbul, E. Cackett, M. Chernyakova, M. Chiao, P. Coppi, E. Costantini, J. de Plaa, J.-W. den Herder, C. Done, T. Dotani, K. Ebisawa, M. Eckart, T. Enoto, Y. Ezoe, A. C. Fabian, C. Ferrigno, A. Foster, R. Fujimoto, Y. Fukazawa, A. Furuzawa, M. Galeazzi, L. Gallo, P. Gandhi, M. Giustini, A. Goldwurm, L. Gu, M. Guainazzi, Y. Haba, K. Hagino, K. Hamaguchi, I. Harrus, I. Hatsukade, K. Hayashi, T. Hayashi, K. Hayashida, J. Hiraga, A. Hornschemeier, A. Hoshino, J. Hughes, R. Iizuka, H. Inoue, Y. Inoue, K. Ishibashi, M. Ishida, K. Ishikawa, Y. Ishisaki, M. Itoh, N. Iyomoto, J. Kaastra, T. Kallman, T. Kamae, E. Kara, J. Kataoka, S. Katsuda, J. Katsuta, M. Kawaharada, N. Kawai, R. Kelley, D. Khangulyan, C. Kilbourne, A. King, T. Kitaguchi, S. Kitamoto, T. Kitayama, T. Kohmura, M. Kokubun, S. Koyama, K. Koyama, P. Kretschmar, H. Krimm, A. Kubota, H. Kunieda, P. Laurent, F. Lebrun, S.-H. Lee, M. Leutenegger, O. Limousin, M. Loewenstein, K. S. Long, D. Lumb, G. Madejski, Y. Maeda, D. Maier, K. Makishima, M. Markevitch, H. Matsumoto, K. Matsushita, D. McCammon, B. McNamara, M. Mehdipour, E. Miller, J. Miller, S. Mineshige, K. Mitsuda, I. Mitsuishi, T. Miyazawa, T. Mizuno, H. Mori, K. Mori, H. Moseley, K. Mukai, H. Murakami, T. Murakami, R. Mushotzky, R. Nagino, T. Nakagawa, H. Nakajima, T. Nakamori, T. Nakano, S. Nakashima, K. Nakazawa, M. Nobukawa, H. Noda, M. Nomachi, S. O'Dell, H. Odaka, T. Ohashi, M. Ohno, T. Okajima, N. Ota, M. Ozaki, F. Paerels, S. Paltani, A. Parmar, R. Petre, C. Pinto, M. Pohl, F. S. Porter, K. Pottschmidt, B. Ramsey, C. Reynolds, H. Russell, S. Safi-Harb, S. Saito, K. Sakai, H. Sameshima, G. Sato, K. Sato, R. Sato, M. Sawada, N. Schartel, P. Serlemitsos, H. Seta, M. Shidatsu, A. Simionescu, R. Smith, Y. Soong, L. Stawarz, Y. Sugawara, S. Sugita, A. Szymkowiak, H. Tajima, H. Takahashi, T. Takahashi, S. Takeda, Y. Takei, T. Tamagawa, K. Tamura, T. Tamura, T. Tanaka, Y. Tanaka, Y. Tanaka, M. Tashiro, Y. Tawara, Y. Terada, Y. Terashima, F. Tombesi, H. Tomida, Y. Tsuboi, M. Tsujimoto, H. Tsunemi, T. Tsuru, H. Uchida, H. Uchiyama, Y. Uchiyama, S. Ueda, Y. Ueda, S. Ueno, S. Uno, M. Urry, E. Ursino, C. de Vries, S. Watanabe, N. Werner, D. Wik, D. Wilkins, B. Williams, S. Yamada, H. Yamaguchi, K. Yamaoka, N. Y. Yamasaki, M. Yamauchi, S. Yamauchi, T. Yaqoob, Y. Yatsu, D. Yonetoku, A. Yoshida, T. Yuasa, I. Zhuravleva and A. Zoghbi, "The quiescent intracluster medium in the core of the Perseus cluster", Nature **535**, 7610, 117–121 (2016).

Hitomi Collaboration, F. Aharonian, H. Akamatsu, F. Akimoto, S. W. Allen, L. Angelini, M. Audard, H. Awaki, M. Axelsson, A. Bamba, M. W. Bautz, R. Blandford, L. W. Brenneman, G. V. Brown, E. Bulbul, E. M. Cackett, R. E. A. Canning, M. Chernyakova, M. P. Chiao, P. S. Coppi, E. Costantini, J. de Plaa, C. P. de Vries, J.-W. den Herder, C. Done, T. Dotani, K. Ebisawa, M. E. Eckart, T. Enoto, Y. Ezoe, A. C. Fabian, C. Ferrigno, A. R. Foster, R. Fujimoto, Y. Fukazawa, A. Furuzawa, M. Galeazzi, L. C. Gallo, P. Gandhi, M. Giustini, A. Goldwurm, L. Gu,

M. Guainazzi, Y. Haba, K. Hagino, K. Hamaguchi, I. M. Harrus, I. Hatsukade, K. Hayashi, T. Hayashi, T. Hayashi, K. Hayashida, J. S. Hiraga, A. Hornschemeier, A. Hoshino, J. P. Hughes, Y. Ichinohe, R. Iizuka, H. Inoue, S. Inoue, Y. Inoue, M. Ishida, K. Ishikawa, Y. Ishisaki, M. Iwai, J. Kaastra, T. Kallman, T. Kamae, J. Kataoka, S. Katsuda, N. Kawai, R. L. Kelley, C. A. Kilbourne, T. Kitaguchi, S. Kitamoto, T. Kitayama, T. Kohmura, M. Kokubun, K. Koyama, S. Koyama, P. Kretschmar, H. A. Krimm, A. Kubota, H. Kunieda, P. Laurent, S.-H. Lee, M. A. Leutenegger, O. Limousin, M. Loewenstein, K. S. Long, D. Lumb, G. Madejski, Y. Maeda, D. Maier, K. Makishima, M. Markevitch, H. Matsumoto, K. Matsushita, D. McCammon, B. R. McNamara, M. Mehdipour, E. D. Miller, J. M. Miller, S. Mineshige, K. Mitsuda, I. Mitsuishi, T. Miyazawa, T. Mizuno, H. Mori, K. Mori, K. Mukai, H. Murakami, R. F. Mushotzky, T. Nakagawa, H. Nakajima, T. Nakamori, S. Nakashima, K. Nakazawa, K. K. Nobukawa, M. Nobukawa, H. Noda, H. Odaka, T. Ohashi, M. Ohno, T. Okajima, N. Ota, M. Ozaki, F. Paerels, S. Paltani, R. Petre, C. Pinto, F. S. Porter, K. Pottschmidt, C. S. Reynolds, S. Safi-Harb, S. Saito, K. Sakai, T. Sasaki, G. Sato, K. Sato, R. Sato, M. Sawada, N. Schartel, P. J. Serlemtsos, H. Seta, M. Shidatsu, A. Simionescu, R. K. Smith, Y. Soong, Ł. Stawarz, Y. Sugawara, S. Sugita, A. Szymkowiak, H. Tajima, H. Takahashi, T. Takahashi, S. Takeda, Y. Takei, T. Tamagawa, T. Tamura, K. Tanaka, T. Tanaka, Y. Tanaka, Y. T. Tanaka, M. S. Tashiro, Y. Tawara, Y. Terada, Y. Terashima, F. Tombesi, H. Tomida, Y. Tsuboi, M. Tsujimoto, H. Tsunemi, T. G. Tsuru, H. Uchida, H. Uchiyama, Y. Uchiyama, S. Ueda, Y. Ueda, S. Uno, C. M. Urry, E. Ursino, Q. H. S. Wang, S. Watanabe, N. Werner, D. R. Wilkins, B. J. Williams, S. Yamada, H. Yamaguchi, K. Yamaoka, N. Y. Yamasaki, M. Yamauchi, S. Yamauchi, T. Yaqoob, Y. Yatsu, D. Yonetoku, I. Zhuravleva and A. Zoghbi, "Atmospheric gas dynamics in the Perseus cluster observed with Hitomi", PASJ**70**, 2, 9 (2018).

Ho, S. H., C. L. Martin, G. G. Kacprzak and C. W. Churchill, "Quasars Probing Galaxies. I. Signatures of Gas Accretion at Redshift Approximately 0.2", ApJ **835**, 2, 267 (2017).

Hodges-Kluck, E. J., M. J. Miller and J. N. Bregman, "The Rotation of the Hot Gas around the Milky Way", ApJ **822**, 1, 21 (2016).

Hofmann, F., J. S. Sanders, K. Nandra, N. Clerc and M. Gaspari, "Thermodynamic perturbations in the X-ray halo of 33 clusters of galaxies observed with Chandra ACIS", A&A **585**, A130 (2016).

Hoyle, F., "On the Fragmentation of Gas Clouds Into Galaxies and Stars.", ApJ **118**, 513 (1953).

Hummels, C. B., G. L. Bryan, B. D. Smith and M. J. Turk, "Constraints on hydrodynamical subgrid models from quasar absorption line studies of the simulated circumgalactic medium", MNRAS **430**, 1548–1565 (2013).

Ji, S., T. Chan, C. B. Hummels, P. F. Hopkins, J. Stern, D. Kereš, E. Quataert, C.-A. Faucher-Giguère and N. Murray, "Properties of the circumgalactic medium in cosmic ray-dominated galaxy halos", arXiv preprint arXiv:1909.00003 (2019).

Johnson, S. D., H.-W. Chen and J. S. Mulchaey, "On the possible environmental effect in distributing heavy elements beyond individual gaseous haloes", MNRAS **449**, 3263–3273 (2015).

Kaastra, J. S., R. Lieu, J. P. D. Mittaz, J. A. M. Bleeker, R. Mewe, S. Colafrancesco and F. J. Lockman, "High- and Low-Energy Nonthermal X-Ray Emission from the Abell 2199 Cluster of Galaxies", ApJ **519**, 2, L119–L122 (1999).

Kafatos, M., "Time-Dependent Radiative Cooling of a Hot Low-Density Cosmic Gas", ApJ **182**, 433–448 (1973).

Kauffmann, G., D. Nelson, S. Borthakur, T. Heckman, L. Hernquist, F. Marinacci, R. Pakmor and A. Pillepich, "The morphology and kinematics of the gaseous circumgalactic medium of Milky Way mass galaxies - II. Comparison of IllustrisTNG and Illustris simulation results", MNRAS **486**, 4, 4686–4700 (2019).

Kauffmann, G., S. D. White and B. Guiderdoni, "The formation and evolution of galaxies within merging dark matter haloes", Monthly Notices of the Royal Astronomical Society **264**, 1, 201–218 (1993).

Kazantsev, A. P., "Enhancement of a Magnetic Field by a Conducting Fluid", Soviet Journal of Experimental and Theoretical Physics **26**, 1031 (1968).

Kereš, D. and L. Hernquist, "Seeding the Formation of Cold Gaseous Clouds in Milky Way-Size Halos", ApJ **700**, 1, L1–L5 (2009).

Kereš, D., N. Katz, D. H. Weinberg and R. Davé, "How do galaxies get their gas?", MNRAS **363**, 1, 2–28 (2005).

Kolmogorov, A. N., "A refinement of previous hypotheses concerning the local structure of turbulence in a viscous incompressible fluid at high Reynolds number", Journal of Fluid Mechanics **13**, 82–85 (1962).

Krause, F. and K. H. Raedler, *Mean-field magnetohydrodynamics and dynamo theory* (1980).

Kravtsov, A. V., D. Nagai and A. A. Vikhlinin, "Effects of Cooling and Star Formation on the Baryon Fractions in Clusters", ApJ **625**, 2, 588–598 (2005).

Kritsuk, A. G., M. L. Norman, P. Padoan and R. Wagner, "The Statistics of Supersonic Isothermal Turbulence", ApJ **665**, 1, 416–431 (2007).

Kronberg, P. P., M. L. Bernet, F. Miniati, S. J. Lilly, M. B. Short and D. M. Higdon, "A Global Probe of Cosmic Magnetic Fields to High Redshifts", ApJ **676**, 1, 70–79 (2008).

Kronberg, P. P. and J. J. Perry, "Absorption lines, Faraday rotation, and magnetic field estimates for QSO absorption-line clouds", ApJ **263**, 518–532 (1982).

Kuntz, K. D. and S. L. Snowden, "Deconstructing the Spectrum of the Soft X-Ray Background", ApJ **543**, 1, 195–215 (2000).

Kwak, K. and R. L. Shelton, "Numerical Study of Turbulent Mixing Layers with Non-equilibrium Ionization Calculations", ApJ **719**, 1, 523–539 (2010).

Laha, S., M. Guainazzi, E. Piconcelli, P. Gandhi, C. Ricci, R. Ghosh, A. G. Markowitz and J. Bagchi, "A study of x-ray emission of galaxies hosting molecular outflows (mox sample)", The Astrophysical Journal **868**, 1, 10 (2018).

Lan, T.-W. and J. X. Prochaska, "Constraining magnetic fields in the circumgalactic medium", MNRAS **496**, 3, 3142–3151 (2020).

Lanzetta, K. M. and D. Bowen, "Intermediate-Redshift Galaxy Halos: Results from QSO Absorption Lines", ApJ **357**, 321 (1990).

Lanzetta, K. M., D. A. Turnshek and A. M. Wolfe, "An Absorption-Line Survey of 32 QSOs at Red Wavelengths: Properties of the MG II Absorbers", ApJ **322**, 739 (1987).

Lee, D., "A solution accurate, efficient and stable unsplit staggered mesh scheme for three dimensional magnetohydrodynamics", Journal of Computational Physics **243**, 269–292 (2013).

Lehner, N., J. C. Howk and B. P. Wakker, "Evidence for a massive, extended circumgalactic medium around the andromeda galaxy", The Astrophysical Journal **804**, 2, 79 (2015).

Lehner, N., C. Kopenhafer, J. O'Meara, J. C. Howk, M. Fumagalli, J. Prochaska, A. Acharyya, B. O'Shea, M. Peeples, J. Tumlinson and C. Hummels, "KODIAQ-Z: Metals and Baryons in the Cool Intergalactic and Circumgalactic Gas at 2.2¡z¡3.6", arXiv e-prints p. arXiv:2112.03304 (2021).

Lehner, N., C. B. Wotta, J. C. Howk, J. M. O'Meara, B. D. Oppenheimer and K. L. Cooksey, "The cos cgm compendium. i. survey design and initial results", The Astrophysical Journal **866**, 1, 33 (2018).

Li, M. and S. Tonnesen, "How do supernovae impact the circumgalactic medium? i. large-scale fountains in a milky way-like galaxy", arXiv preprint arXiv:1910.14235 (2019).

Liang, C. J. and H.-W. Chen, "Mining circumgalactic baryons in the low-redshift universe", MNRAS **445**, 2061–2081 (2014).

Liang, C. J., A. V. Kravtsov and O. Agertz, "Observing the circumgalactic medium of simulated galaxies through synthetic absorption spectra", MNRAS **479**, 1822–1835 (2018).

Liang, C. J. and I. Remming, "On the model of the circumgalactic mist: the implications of cloud sizes in galactic winds and haloes", Monthly Notices of the Royal Astronomical Society **491**, 4, 5056–5072 (2020).

Licquia, T. C. and J. A. Newman, "Improved Estimates of the Milky Way's Stellar Mass and Star Formation Rate from Hierarchical Bayesian Meta-Analysis", ApJ **806**, 1, 96 (2015).

Lilly, S. J., C. M. Carollo, A. Pipino, A. Renzini and Y. Peng, "Gas Regulation of Galaxies: The Evolution of the Cosmic Specific Star Formation Rate, the Metallicity-Mass-Star-formation Rate Relation, and the Stellar Content of Halos", ApJ **772**, 2, 119 (2013).

Lochhaas, C., S. Mathur, S. Frank, D. Som, Y. Krongold, V. Kulkarni, D. H. Weinberg, F. Nicastro and A. Gupta, "A high signal-to-noise hst spectrum towards j1009+ 0713: precise absorption measurements in the cgm of two galaxies", Monthly Notices of the Royal Astronomical Society **489**, 1, 78–98 (2019).

Lodders, K., "Solar System Abundances of the Elements", Astrophysics and Space Science Proceedings **16**, 379 (2010).

Macciò, A. V., A. A. Dutton and F. C. van den Bosch, "Concentration, spin and shape of dark matter haloes as a function of the cosmological model: WMAP1, WMAP3 and WMAP5 results", MNRAS **391**, 4, 1940–1954 (2008).

Malik, S., H. Chand and T. R. Seshadri, "Role of Intervening Mg II Absorbers on the Rotation Measure and Fractional Polarization of the Background Quasars", ApJ **890**, 2, 132 (2020).

Marinacci, F., M. Vogelsberger, R. Pakmor, P. Torrey, V. Springel, L. Hernquist, D. Nelson, R. Weinberger, A. Pillepich, J. Naiman and S. Genel, "First results from the IllustrisTNG simulations: radio haloes and magnetic fields", MNRAS **480**, 4, 5113–5139 (2018).

Mathews, W. G., D. A. Buote and F. Brighenti, "Spatial Diffusion of X-Ray Emission Lines in the M87 Cooling Flow; Evidence for Absorption", ApJ **550**, 1, L31–L34 (2001).

McCourt, M., P. Sharma, E. Quataert and I. J. Parrish, "Thermal instability in gravitationally stratified plasmas: implications for multiphase structure in clusters and galaxy haloes", Monthly Notices of the Royal Astronomical Society **419**, 4, 3319–3337 (2012).

McEwen, J. E. and D. H. Weinberg, "The effects of assembly bias on the inference of matter clustering from galaxy-galaxy lensing and galaxy clustering", MNRAS **477**, 4, 4348–4361 (2018).

Morris, S. L., R. J. Weymann, B. D. Savage and R. L. Gilliland, "First Results from the Goddard High-Resolution Spectrograph: The Galactic Halo and the LY alpha Forest at Low Redshift in 3C 273", ApJ **377**, L21 (1991).

Münch, G. and H. Zirin, "Interstellar Matter at Large Distances from the Galactic Plane.", ApJ **133**, 11 (1961).

Muratov, A. L., D. Kereš, C.-A. Faucher-Giguère, P. F. Hopkins, X. Ma, D. Anglés-Alcázar, T. K. Chan, P. Torrey, Z. H. Hafen, E. Quataert and N. Murray, "Metal flows of the circumgalactic medium, and the metal budget in galactic haloes", MNRAS **468**, 4170–4188 (2017).

Navarro, J. F., C. S. Frenk and S. D. M. White, "The Structure of Cold Dark Matter Halos", ApJ **462**, 563 (1996).

Nelson, D., G. Kauffmann, A. Pillepich, S. Genel, V. Springel, R. Pakmor, L. Hernquist, R. Weinberger, P. Torrey, M. Vogelsberger and F. Marinacci, "The abundance, distribution, and physical nature of highly ionized oxygen O VI, O VII, and O VIII in IllustrisTNG", MNRAS **477**, 450–479 (2018a).

Nelson, D., A. Pillepich, V. Springel, R. Weinberger, L. Hernquist, R. Pakmor, S. Genel, P. Torrey, M. Vogelsberger, G. Kauffmann, F. Marinacci and J. Naiman, "First results from the IllustrisTNG simulations: the galaxy colour bimodality", MNRAS **475**, 1, 624–647 (2018b).

Nelson, D., P. Sharma, A. Pillepich, V. Springel, R. Pakmor, R. Weinberger, M. Vogelsberger, F. Marinacci and L. Hernquist, "Resolving small-scale cold circumgalactic gas in TNG50", MNRAS **498**, 2, 2391–2414 (2020).

Ocvirk, P., C. Pichon and R. Teyssier, "Bimodal gas accretion in the horizon–marenostrum galaxy formation simulation", MNRAS **390**, 4, 1326–1338 (2008).

Ogorzalek, A., I. Zhuravleva, S. W. Allen, C. Pinto, N. Werner, A. B. Mantz, R. E. A. Canning, A. C. Fabian, J. S. Kaastra and J. de Plaa, "Improved measurements of turbulence in the hot gaseous atmospheres of nearby giant elliptical galaxies", MNRAS **472**, 2, 1659–1676 (2017).

Oh, S. P. and A. J. Benson, "Entropy injection as a global feedback mechanism", MNRAS **342**, 2, 664–672 (2003).

Oppenheimer, B. D., R. A. Crain, J. Schaye, A. Rahmati, A. J. Richings, J. W. Trayford, J. Tumlinson, R. G. Bower, M. Schaller and T. Theuns, "Bimodality of low-redshift circumgalactic O VI in non-equilibrium EAGLE zoom simulations", MNRAS **460**, 2, 2157–2179 (2016).

Oppenheimer, B. D. and R. Davé, "Mass, metal, and energy feedback in cosmological simulations", MNRAS **387**, 2, 577–600 (2008).

Oppenheimer, B. D. and J. Schaye, "Non-equilibrium ionization and cooling of metal-enriched gas in the presence of a photoionization background", MNRAS **434**, 2, 1043–1062 (2013).

Oppenheimer, B. D., J. Schaye, R. A. Crain, J. K. Werk and A. J. Richings, "The multiphase circumgalactic medium traced by low metal ions in EAGLE zoom simulations", ArXiv e-prints (2017).

Oppenheimer, B. D., J. Schaye, R. A. Crain, J. K. Werk and A. J. Richings, "The multiphase circumgalactic medium traced by low metal ions in eagle zoom simulations", Monthly Notices of the Royal Astronomical Society **481**, 1, 835–859 (2018).

Pakmor, R., F. A. Gómez, R. J. J. Grand, F. Marinacci, C. M. Simpson, V. Springel, D. J. R. Campbell, C. S. Frenk, T. Guillet, C. Pfrommer and S. D. M. White, "Magnetic field formation in the Milky Way like disc galaxies of the Auriga project", MNRAS **469**, 3, 3185–3199 (2017).

Pakmor, R., F. Marinacci and V. Springel, "Magnetic Fields in Cosmological Simulations of Disk Galaxies", ApJ **783**, 1, L20 (2014).

Pakmor, R., F. van de Voort, R. Bieri, F. A. Gómez, R. J. J. Grand, T. Guillet, F. Marinacci, C. Pfrommer, C. M. Simpson and V. Springel, "Magnetizing the circumgalactic medium of disc galaxies", Monthly Notices of the Royal Astronomical Society **498**, 3, 3125–3137, URL `http://dx.doi.org/10.1093/mnras/staa2530` (2020).

Pan, L. and E. Scannapieco, "Mixing in Supersonic Turbulence", ApJ **721**, 2, 1765–1782 (2010).

Pickelner, S., "Publ. crimean astrophys. obs. 10, 74 (1953)", in "Doklady Acad. Sci. USSR", vol. 88, p. 229 (1953).

Pieri, M. M., M. J. Mortonson, S. Frank, N. Crighton, D. H. Weinberg, K.-G. Lee, P. Noterdaeme, S. Bailey, N. Busca, J. Ge, D. Kirkby, B. Lundgren, S. Mathur, I. Pâris, N. Palanque-Delabrouille, P. Petitjean, J. Rich, N. P. Ross, D. P. Schneider and D. G. York, "Probing the circumgalactic medium at high-redshift using composite BOSS spectra of strong Lyman α forest absorbers", MNRAS **441**, 1718–1740 (2014).

Pillepich, A., V. Springel, D. Nelson, S. Genel, J. Naiman, R. Pakmor, L. Hernquist, P. Torrey, M. Vogelsberger, R. Weinberger and F. Marinacci, "Simulating galaxy formation with the IllustrisTNG model", MNRAS **473**, 3, 4077–4106 (2018).

Planelles, S., S. Borgani, K. Dolag, S. Ettori, D. Fabjan, G. Murante and L. Tornatore, "Baryon census in hydrodynamical simulations of galaxy clusters", MNRAS **431**, 2, 1487–1502 (2013).

Prescott, M. K., C. L. Martin and A. Dey, "Spatially resolved gas kinematics within a lyα nebula: evidence for large-scale rotation", The Astrophysical Journal **799**, 1, 62 (2015).

Prochaska, J. X., B. Weiner, H. W. Chen, J. Mulchaey and K. Cooksey, "Probing the Intergalactic Medium/Galaxy Connection. V. On the Origin of Lyα and O VI Absorption at z ¡ 0.2", ApJ **740**, 2, 91 (2011).

Prochaska, J. X., J. K. Werk, G. Worseck, T. M. Tripp, J. Tumlinson, J. N. Burchett, A. J. Fox, M. Fumagalli, N. Lehner, M. S. Peeples *et al.*, "The cos-halos survey: Metallicities in the low-redshift circumgalactic medium", ApJ **837**, 2, 169 (2017).

Rees, M. J. and J. P. Ostriker, "Cooling, dynamics and fragmentation of massive gas clouds: clues to the masses and radii of galaxies and clusters.", MNRAS **179**, 541–559 (1977).

Rephaeli, Y. and E. Salpeter, "Flow past a massive object and the gravitational drag", The Astrophysical Journal **240**, 20–24 (1980).

Rieder, M. and R. Teyssier, "A small-scale dynamo in feedback-dominated galaxies as the origin of cosmic magnetic fields - I. The kinematic phase", MNRAS **457**, 2, 1722–1738 (2016).

Rieder, M. and R. Teyssier, "A small-scale dynamo in feedback-dominated galaxies - II. The saturation phase and the final magnetic configuration", MNRAS **471**, 3, 2674–2686 (2017a).

Rieder, M. and R. Teyssier, "A small-scale dynamo in feedback-dominated galaxies - III. Cosmological simulations", MNRAS **472**, 4, 4368–4373 (2017b).

Roca-Fàbrega, S., J.-H. Kim, L. Hausammann, K. Nagamine, A. Lupi, J. W. Powell, I. Shimizu, D. Ceverino, J. R. Primack, T. R. Quinn, Y. Revaz, H. Velázquez, T. Abel, M. Buehlmann, A. Dekel, B. Dong, O. Hahn, C. Hummels, K.-W. Kim, B. D. Smith, C. Strawn, R. Teyssier, M. J. Turk and AGORA Collaboration, "The AGORA High-resolution Galaxy Simulations Comparison Project. III. Cosmological Zoom-in Simulation of a Milky Way-mass Halo", ApJ **917**, 2, 64 (2021).

Rubin, K. H., J. X. Prochaska, D. C. Koo, A. C. Phillips, C. L. Martin and L. O. Winstrom, "Evidence for ubiquitous collimated galactic-scale outflows along the star-forming sequence at z 0.5", The Astrophysical Journal **794**, 2, 156 (2014).

Rubin, K. H. R., J. X. Prochaska, D. C. Koo and A. C. Phillips, "The Direct Detection of Cool, Metal-enriched Gas Accretion onto Galaxies at z ~0.5", ApJ **747**, 2, L26 (2012).

Rudie, G. C., C. C. Steidel, M. Pettini, R. F. Trainor, A. L. Strom, C. B. Hummels, N. A. Reddy and A. E. Shapley, "Column Density, Kinematics, and Thermal State of Metal-bearing Gas within the Virial Radius of z 2 Star-forming Galaxies in the Keck Baryonic Structure Survey", ApJ **885**, 1, 61 (2019).

Rudie, G. C., C. C. Steidel, R. F. Trainor, O. Rakic, M. Bogosavljević, M. Pettini, N. Reddy, A. E. Shapley, D. K. Erb and D. R. Law, "The gaseous environment of high-z galaxies: Precision measurements of neutral hydrogen in the circumgalactic medium of z 2-3 galaxies in the keck baryonic structure survey", ApJ **750**, 1, 67 (2012).

Salpeter, E. E., "The luminosity function and stellar evolution.", The Astrophysical Journal **121**, 161 (1955).

Sanders, J. S. and A. C. Fabian, "Resonance scattering, absorption and off-centre abundance peaks in clusters of galaxies", MNRAS **370**, 1, 63–73 (2006).

Sargent, W. L. W., P. J. Young, A. Boksenberg and D. Tytler, "The distribution of Lyman-alpha absorption lines in the spectra of six QSOs: evidence for an intergalactic origin.", ApJS **42**, 41–81 (1980).

Scannapieco, E., W. J. Gray and L. Pan, "Identification of a Fundamental Transition in a Turbulently Supported Interstellar Medium", ApJ **746**, 1, 57 (2012).

Schaye, J., R. A. Crain, R. G. Bower, M. Furlong, M. Schaller, T. Theuns, C. Dalla Vecchia, C. S. Frenk, I. G. McCarthy, J. C. Helly, A. Jenkins, Y. M. Rosas-Guevara, S. D. M. White, M. Baes, C. M. Booth, P. Camps, J. F. Navarro, Y. Qu, A. Rahmati, T. Sawala, P. A. Thomas and J. Trayford, "The EAGLE project: simulating the evolution and assembly of galaxies and their environments", MNRAS **446**, 1, 521–554 (2015).

Schroetter, I., N. F. Bouché, J. Zabl, T. Contini, M. Wendt, J. Schaye, P. Mitchell, S. Muzahid, R. A. Marino, R. Bacon *et al.*, "Muse gas flow and wind (megaflow)–iii. galactic wind properties using background quasars", Monthly Notices of the Royal Astronomical Society **490**, 3, 4368–4381 (2019).

Sembach, K., B. Wakker, B. Savage, P. Richter, M. Meade, J. Shull, E. Jenkins, G. Sonneborn and H. Moos, "Highly ionized high-velocity gas in the vicinity of the galaxy", The Astrophysical Journal Supplement Series **146**, 1, 165 (2003).

Sembolini, F., P. J. Elahi, F. R. Pearce, C. Power, A. Knebe, S. T. Kay, W. Cui, G. Yepes, A. M. Beck, S. Borgani, D. Cunnama, R. Davé, S. February, S. Huang, N. Katz, I. G. McCarthy, G. Murante, R. D. A. Newton, V. Perret, E. Puchwein, A. Saro, J. Schaye and R. Teyssier, "nIFTy galaxy cluster simulations - II. Radiative models", MNRAS **459**, 3, 2973–2991 (2016a).

Sembolini, F., G. Yepes, F. R. Pearce, A. Knebe, S. T. Kay, C. Power, W. Cui, A. M. Beck, S. Borgani, C. Dalla Vecchia, R. Davé, P. J. Elahi, S. February, S. Huang, A. Hobbs, N. Katz, E. Lau, I. G. McCarthy, G. Murante, D. Nagai, K. Nelson, R. D. A. Newton, V. Perret, E. Puchwein, J. I. Read, A. Saro, J. Schaye, R. Teyssier and R. J. Thacker, "nIFTy galaxy cluster simulations - I. Dark matter and non-radiative models", MNRAS **457**, 4, 4063–4080 (2016b).

Semenov, V. and L. Bernikov, "Structure of the magnetic field and currents in an ideally conducting plasma.", Geomagnitnye Issledovaniia **26**, 40–48 (1980).

Shapiro, P. R. and G. B. Field, "Consequences of a New Hot Component of the Interstellar Medium", ApJ **205**, 762–765 (1976).

Sharma, P., M. McCourt, E. Quataert and I. J. Parrish, "Thermal instability and the feedback regulation of hot haloes in clusters, groups and galaxies", MNRAS **420**, 4, 3174–3194 (2012).

Shen, S., P. Madau, J. Guedes, L. Mayer, J. X. Prochaska and J. Wadsley, "The Circumgalactic Medium of Massive Galaxies at z ~ 3: A Test for Stellar Feedback, Galactic Outflows, and Cold Streams", ApJ **765**, 89 (2013).

Shklovsky, I., "On the nature of radio emission from the galaxy", Astr. Zhur. SSSR **29**, 418 (1952).

Shull, J. M., "The Cosmic Origins Spectrograph and the Future of Ultraviolet Astronomy", in "Future Directions in Ultraviolet Spectroscopy", edited by M. E. e. a. van Steenberg, vol. 1135 of *AIP Conf. Ser.*, p. 301 (2009).

Shull, J. M. and M. Van Steenberg, "The ionization equilibrium of astrophysically abundant elements", ApJS **48**, 95–107 (1982).

Silk, J., "On the fragmentation of cosmic gas clouds. I. The formation of galaxies and the first generation of stars.", ApJ **211**, 638–648 (1977).

Simionescu, A., J. ZuHone, I. Zhuravleva, E. Churazov, M. Gaspari, D. Nagai, N. Werner, E. Roediger, R. Canning, D. Eckert, L. Gu and F. Paerels, "Constraining Gas Motions in the Intra-Cluster Medium", SSR**215**, 2, 24 (2019).

Slavin, J. D., J. M. Shull and M. C. Begelman, "Turbulent Mixing Layers in the Interstellar Medium of Galaxies", ApJ **407**, 83 (1993).

Smith, S., "The Mass of the Virgo Cluster", ApJ **83**, 23 (1936).

Somerville, R. S. and J. R. Primack, "Semi-analytic modelling of galaxy formation: the local universe", Monthly Notices of the Royal Astronomical Society **310**, 4, 1087–1110 (1999).

Spitzer, J., Lyman, "On a Possible Interstellar Galactic Corona.", ApJ **124**, 20 (1956).

Springel, V., "The cosmological simulation code GADGET-2", MNRAS **364**, 4, 1105–1134 (2005).

Springel, V., J. Wang, M. Vogelsberger, A. Ludlow, A. Jenkins, A. Helmi, J. F. Navarro, C. S. Frenk and S. D. White, "The aquarius project: the subhaloes of galactic haloes", Monthly Notices of the Royal Astronomical Society **391**, 4, 1685–1711 (2008).

Steidel, C., "Gaseous "Halos" and High Redshift Galaxies", in "Galactic Halos", edited by D. Zaritsky, vol. 136 of *ASP Conf. Ser.*, p. 167 (1998).

Steidel, C. C., M. Dickinson and S. E. Persson, "Field Galaxy Evolution Since Z approximately 1 from a Sample of QSO Absorption–selected Galaxies", ApJ **437**, L75 (1994).

Steidel, C. C. and W. L. W. Sargent, "The Effect of the Lyman-Alpha Forest on the Ultraviolet Continua of Very High Redshift Quasars", ApJ **313**, 171 (1987).

Stern, J., D. Fielding, C.-A. Faucher-Giguère and E. Quataert, "Cooling flow solutions for the circumgalactic medium", Monthly Notices of the Royal Astronomical Society **488**, 2, 2549–2572 (2019).

Stewart, K. R., T. Kaufmann, J. S. Bullock, E. J. Barton, A. H. Maller, J. Diemand and J. Wadsley, "Orbiting Circumgalactic Gas as a Signature of Cosmological Accretion", ApJ **738**, 1, 39 (2011).

Strickland, D. K. and T. M. Heckman, "Iron line and diffuse hard x-ray emission from the starburst galaxy m82", The Astrophysical Journal **658**, 1, 258 (2007).

Strickland, D. K. and T. M. Heckman, "Supernova feedback efficiency and mass loading in the starburst and galactic superwind exemplar m82", The Astrophysical Journal **697**, 2, 2030 (2009).

Su, K.-Y., P. F. Hopkins, C. C. Hayward, C.-A. Faucher-Giguère, D. Kereš, X. Ma, M. E. Orr, T. Chan and V. H. Robles, "Cosmic rays or turbulence can suppress cooling flows (where thermal heating or momentum injection fail)", Monthly Notices of the Royal Astronomical Society **491**, 1, 1190–1212 (2020).

Sur, S., E. Scannapieco and E. C. Ostriker, "Galaxy Outflows Without Supernovae", ApJ **818**, 1, 28 (2016).

Ter Haar, D., "Book Reviews: Gas Dynamics of Cosmic Clouds. A Symposium of the International Union of Theoretical and Applied Mechanics and International Astronomical Union", Science **122**, 3176, 928–929 (1955).

Toro, E. F., *Riemann solvers and numerical methods for fluid dynamics: a practical introduction* (Springer, 1999).

Toro, E. F., M. Spruce and W. Speares, "Restoration of the contact surface in the hll-riemann solver", Shock waves **4**, 1, 25–34 (1994).

Tumlinson, J., M. S. Peeples and J. K. Werk, "The Circumgalactic Medium", ARA&A **55**, 1, 389–432 (2017).

Tumlinson, J., C. Thom, J. K. Werk, J. X. Prochaska, T. M. Tripp, N. Katz, R. Davé, B. D. Oppenheimer, J. D. Meiring, A. B. Ford, J. M. O'Meara, M. S. Peeples, K. R. Sembach and D. H. Weinberg, "The COS-Halos Survey: Rationale, Design, and a Census of Circumgalactic Neutral Hydrogen", ApJ **777**, 1, 59 (2013).

Turner, J., S. Beck, D. Benford, S. Consiglio, P. T. Ho, A. Kovács, D. Meier and J.-H. Zhao, "Highly efficient star formation in ngc 5253 possibly from stream-fed accretion", Nature **519**, 7543, 331–333 (2015).

Turner, M. L., J. Schaye, C. C. Steidel, G. C. Rudie and A. L. Strom, "Metal-line absorption around z $\approx$ 2.4 star-forming galaxies in the Keck Baryonic Structure Survey", MNRAS **445**, 1, 794–822 (2014).

Uhlenbeck, G. E. and L. S. Ornstein, "On the theory of the brownian motion", Physical review **36**, 5, 823 (1930).

van de Voort, F., J. Schaye, C. M. Booth, M. R. Haas and C. Dalla Vecchia, "The rates and modes of gas accretion on to galaxies and their gaseous haloes", MNRAS **414**, 3, 2458–2478 (2011).

Vazza, F., M. Brüggen, C. Gheller and P. Wang, "On the amplification of magnetic fields in cosmic filaments and galaxy clusters", MNRAS **445**, 4, 3706–3722 (2014).

Veilleux, S., G. Cecil and J. Bland-Hawthorn, "Galactic winds", Annu. Rev. Astron. Astrophys. **43**, 769–826 (2005).

Verner, D. A., G. J. Ferland, K. T. Korista and D. G. Yakovlev, "Atomic Data for Astrophysics. II. New Analytic FITS for Photoionization Cross Sections of Atoms and Ions", ApJ **465**, 487 (1996).

Verner, D. A. and D. G. Yakovlev, "Analytic FITS for partial photoionization cross sections.", A&A SS**109**, 125–133 (1995).

Voit, G. M., G. L. Bryan, M. L. Balogh and R. G. Bower, "Modified Entropy Models for the Intracluster Medium", ApJ **576**, 2, 601–624 (2002).

Voit, G. M., G. L. Bryan, B. W. O'Shea and M. Donahue, "Precipitation-regulated Star Formation in Galaxies", ApJ **808**, 1, L30 (2015).

Voit, G. M., G. Meece, Y. Li, B. W. O'Shea, G. L. Bryan and M. Donahue, "A global model for circumgalactic and cluster-core precipitation", The Astrophysical Journal **845**, 1, 80 (2017).

Wakker, B. P. and B. D. Savage, "The Relationship Between Intergalactic H I/O VI and Nearby (z ¡ 0.017) Galaxies", ApJS **182**, 1, 378–467 (2009).

Wakker, B. P., B. D. Savage, A. J. Fox, R. A. Benjamin and P. R. Shapiro, "Characterizing Transition Temperature Gas in the Galactic Corona", ApJ **749**, 2, 157 (2012).

Welter, G. L., J. J. Perry and P. P. Kronberg, "The rotation measure distribution of QSOs and of intervening clouds :magnetic fields and column densities.", ApJ **279**, 19–39 (1984).

Werk, J. K., J. X. Prochaska, S. Cantalupo, A. J. Fox, B. Oppenheimer, J. Tumlinson, T. M. Tripp, N. Lehner and M. McQuinn, "The COS-Halos Survey: Origins of the Highly Ionized Circumgalactic Medium of Star-Forming Galaxies", ApJ **833**, 1, 54 (2016).

Werk, J. K., J. X. Prochaska, C. Thom, J. Tumlinson, T. M. Tripp, J. M. O'Meara and M. S. Peeples, "The COS-Halos Survey: An Empirical Description of Metal-line Absorption in the Low-redshift Circumgalactic Medium", ApJS **204**, 2, 17 (2013).

Werk, J. K., J. X. Prochaska, J. Tumlinson, M. S. Peeples, T. M. Tripp, A. J. Fox, N. Lehner, C. Thom, J. M. O'Meara, A. B. Ford *et al.*, "The cos-halos survey: physical conditions and baryonic mass in the low-redshift circumgalactic medium", ApJ **792**, 1, 8 (2014).

Werner, N., I. Zhuravleva, E. Churazov, A. Simionescu, S. W. Allen, W. Forman, C. Jones and J. S. Kaastra, "Constraints on turbulent pressure in the X-ray haloes of giant elliptical galaxies from resonant scattering", MNRAS **398**, 1, 23–32 (2009).

White, S. D. M., J. F. Navarro, A. E. Evrard and C. S. Frenk, "The baryon content of galaxy clusters: a challenge to cosmological orthodoxy", Nature **366**, 6454, 429–433 (1993).

Wiersma, R. P., J. Schaye and B. D. Smith, "The effect of photoionization on the cooling rates of enriched, astrophysical plasmas", Monthly Notices of the Royal Astronomical Society **393**, 1, 99–107 (2009).

Xu, H., S. M. Kahn, J. R. Peterson, E. Behar, F. B. S. Paerels, R. F. Mushotzky, J. G. Jernigan, A. C. Brinkman and K. Makishima, "High-Resolution Observations of the Elliptical Galaxy NGC 4636 with the Reflection Grating Spectrometer on Board XMM-Newton", ApJ **579**, 2, 600–606 (2002).

Young, P., W. L. W. Sargent and A. Boksenberg, "C IV absorption in an unbiased sample of 33 QSOs: evidence for the intervening galaxy hypothesis.", ApJS **48**, 455–506 (1982).

Zahedy, F. S., H.-W. Chen, S. D. Johnson, R. M. Pierce, M. Rauch, Y.-H. Huang, B. J. Weiner and J.-R. Gauthier, "Characterizing circumgalactic gas around massive ellipticals at z~0.4 - II. Physical properties and elemental abundances", MNRAS **484**, 2, 2257–2280 (2019).

Zehavi, I., S. Contreras, N. Padilla, N. J. Smith, C. M. Baugh and P. Norberg, "The Impact of Assembly Bias on the Galaxy Content of Dark Matter Halos", ApJ **853**, 1, 84 (2018).

Zeldovich, Y. B., A. A. Ruzmaikin and D. D. Sokoloff, *The almighty chance* (1990).

Zhuravleva, I., S. W. Allen, A. Mantz and N. Werner, "Gas Perturbations in the Cool Cores of Galaxy Clusters: Effective Equation of State, Velocity Power Spectra, and Turbulent Heating", ApJ **865**, 1, 53 (2018).

Zhuravleva, I., E. Churazov, R. Sunyaev, S. Sazonov, S. W. Allen, N. Werner, A. Simionescu, S. Konami and T. Ohashi, "Resonant scattering in the Perseus Cluster: spectral model for constraining gas motions with Astro-H", MNRAS **435**, 4, 3111–3121 (2013).